Experimental Assessment of Heat Treatments on Large Forgings for Nuclear Applications by Microstructure and Mechanical Property Assessment at the Correct Length Scale

A thesis submitted for the partial fulfilment of the degree of Doctor of Philosophy

Jared James Kitchen

The University of Sheffield

Department of Materials Science and Engineering

January 2018

DECLARATION

This dissertation is submitted in the partial fulfilment of the degree of Doctor of Philosophy at the University of Sheffield. The research was completed between September 2014 and September 2017, under the supervision of Professor Bradley Wynne within the Department of Materials Science and Engineering, The University of Sheffield, UK, and in collaboration with Sheffield Forgemasters International Limited, Sheffield, UK.

I hereby declare that the contents of this dissertation are my own work, and are not collaborations with others, except where otherwise stated. In respect, the works contained are not part of any other submission, for any other degree or diploma, at any other university or institute of higher education. Neither do the contents exceed the stipulated limit of 80,000 words.

Some of the contents have been publicised:

J. J. Kitchen, B. P. Wynne, S. Al-Bermani, J. Talamentes Silva, A New Experimental Methodology of Predicting Through Thickness Property Variation in Large Forgings, *Proceedings of the 20th International Forgemasters Meeting, 2017,* 486-496, 2017.

Signed

Jared J Kitchen

January 2018

ACKNOWLEDGEMENTS

Studying for my PhD has often felt like a long and independent journey with a large number of obstacles to overcome, many of which were not anticipated. It has often felt like an unsupported journey, but now that I am at the end it is possible for me to reflect clearly, and I am humbled in the knowledge that it would not have been possible without the support and guidance of many in the last 3 years.

I would firstly like to thank my supervisor Professor Bradley Wynne at The University of Sheffield, who in his way guided me towards the end. I realise that much of his input, while not clear to me at the time, has been to help me to complete my PhD, and I am truly thankful for it. I would also like to acknowledge the input of my industrial supervisors, Dr Sinan Al-Bermani and Professor Jesus Talamentes-Silva, at Sheffield Forgemasters International Limited. Sinan especially has been a source of practical insight and inspiration over the last 3 years, and his contribution will not be forgotten.

I have been blessed with the support of two institutions and industry backing during my PhD, and there are many who have contributed that should be acknowledged. At the University of Sheffield, I would like to thank Mr Andrew Mould, Mr Kyle Arnold, and Mr Michael Bell whose technical support has helped me complete the many practical

ABSTRACT

The content of this thesis details the experimental verification and validation of new heat treatment simulation technology. The heat treatment simulator (HTS) takes the form of a large dilatometer, and generates volumes of material that accurately represent any simulated thermal program. What is novel and unique about the technology is that the volumes of material produced are large enough to allow both microstructure investigation and mechanical testing from individual specimens, and this functionality yields a method of experimentally assessing the effect of heat treatments on large forgings at the correct length scale.

The experimental part of the thesis begins in Chapter 3 where initial investigations lead to an optimisation study. The study shows that large volumes of representative material are produced when simulating heat treatments using the HTS, but identifies the existence of systematic errors in the recorded results. This is investigated in Chapter 4, where a calibration procedure is developed that significantly reduces systematic error in the recorded data during testing. This work shows that the HTS can both simulate heat treatments accurately and can produce accurate data for analysis, and therefore its function is verified.

Following verification, the HTS function is validated by two experimental studies. In Chapter 5, a new methodology of predicting property variation in large forgings is tested. A thermal profile of a large tubesheet forging undergoing heat treatment is simulated, and the results are compared to identical small-scale experiments. The results show that the HTS can be used to simulate complex thermal profiles accurately, but highlights the need for detailed material characterisations. In Chapter 6, the HTS is used to characterise the pressure vessel alloy SA508 Grade 3 Class 1 under continuous cooling conditions. The results are compared with small-scale experiments, giving validation, and allowing a continuous cooling transformation diagram to be plotted with mechanical properties, a functionality only possible using the HTS.

CONTENTS

NOMENCLATURE

The following denotations are specified in SI units unless where otherwise stated:

α	Radiation, cross sectional area (m^2), CTE (1/°C)
β	Radiation
γ	Radiation
E	Energy (J)
M	Mass (kg)
C	Velocity of light (m/s)
T	Thickness (mm), Temperature (°C)
Lo	Original Length (mm)
L	Length (mm)
α_T	True CTE (1/°C)
P	Power (W)
I	Current (amperes)
R	Resistance (ohms)
ρ	Resistivity (1/ohms)
Io	Applied current (amperes)

Y	Depth from surface (mm)
δ	Reference depth (m)
μ	Relative permeability
f	Frequency (Hz)

ABBREVIATIONS

CTE	Coefficient of thermal expansion
HTS	Heat treatment simulator
CCT	Continuous cooling transformations
LWR	Light water reactor
PWR	Pressurised water reactor
BWR	Boiling water reactor
AGR	Advanced gas-cooled reactor
GIF	Generation 4 international forum
RPV	Reactor pressure vessel
EPR	European pressurised water reactor
FOS	Factor of safety
ASME	American society of mechanical engineers
BPVC	Boiler and pressure vessel code
ASTM	American society of testing and materials
VCD	Vacuum carbon de-oxidation
SHT	Solution heat treatment
QHT	Quality heat treatment

PAGS	Prior austenite grain size
TE	Thermal equilibrium
TTT	Time-temperature transformation
SFIL	Sheffield Forgemasters International Limited
PLC	Programmable logic controller
PID	Proportional, integral, differential
FE	Finite element
TM	Temperature measurement
OES	Optical emission spectrometry
SRM	Standard reference material
FCC	Face centred cubic
BCC	Body centred cubic
LVDT	Linear variable differential transformer
XRF	X-ray fluorescence
EDS	Energy dispersive x-ray spectroscopy
RT	Room temperature
AQ	As-quenched
QT	Quench and tempered
ICP	Inductively coupled plasma
AES	Atomic emission spectroscopy
LMP	Larson-miller parameter
DSC	Differential scanning calorimetry
SEM	Scanning electron microscope

1   INTRODUCTION

Dilatometry is an effective and common technique for characterising dimensional changes of materials under the application of heat. In this technique, the change in length of a standard material test piece is measured as a function of temperature to identify thermally driven events like phase transformations and derive material constants such as the coefficient of thermal expansion (CTE). For industrial processes, dilatometry is a useful tool for evaluating the effect of heat treatments on materials and components before full-scale production. However, modern dilatometers, while sophisticated in function, remain small in scale, and do not permit experimental characterisation of mechanical properties as defined by industrial standards and codes. The logical progression is thus to develop and validate a large dilatometer that can provide sufficient material volumes to produce standard size mechanical test specimens. This thesis presents the experimental validation studies of such a dilatometer, the first of its kind, known in Sheffield Forgemasters, where the machine is housed, as the heat treatment simulator (HTS).

The HTS is to be used in the development of a new methodology, which aims to improve upon the efficiency of empirical methods used to develop industrial heat treatments for large forgings. The objective is to substitute destructive testing of component test coupons by simulating location specific thermal evolution of components under

heat treatment, and produce large specimens for complete characterisations at the correct length scale. The strength in the methodology is that the thermal evolution of specific points within a forging can be fully characterised from a single HTS specimen, significantly improving the speed and efficiency of heat treatment development.

For manufactures of large-scale safety critical forgings, a method of assessing through thickness microstructure evolution of components as a function of heat treatment is a valuable asset. However, for the new methodology to become meaningful to industry, certainty in the HTS function must be shown.

2   LITERATURE REVIEW

2.1   CIVIL NUCLEAR ENERGY

2.1.1   Radioactive decay

Atoms are formed from protons, electrons and neutrons. Protons and neutrons are large and heavy compared to electrons and are grouped together in the centre of an atom to form a nucleus. Electrons are much smaller and lighter than protons and neutrons and orbit the nucleus as shown in Figure 1. Protons and electrons have positive and negative electro-static charges respectively, which are equal, and sum to balance the total charge of the atom; hence, there are the same number of protons and electrons in an atom. This number is the atomic number that determines the atom's position on the periodic table of elements. Neutrons do not have a charge and subsequently, the number of neutrons in a given atom can vary, however, because the neutrons do not have a charge, they do not contribute to the forces that bind the atoms nucleus together and in certain numbers, can cause atoms to become unbalanced. Neutrons have a similar mass to protons and therefore the addition or subtraction of neutrons to an atom also changes the mass of that atom; each different atomic mass for the same element is named an isotope. It follows that some isotopes are more balanced than others, and that the larger the nucleus of the atom, the more likely it is to be unbalanced.
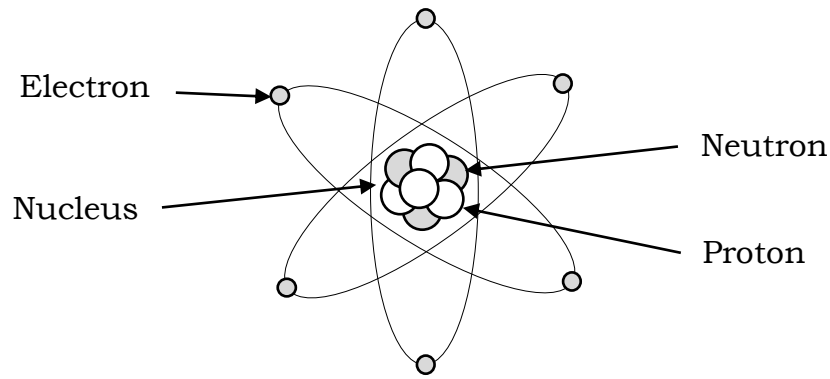
Figure 1: Atom Structure

When an isotope becomes unbalanced by the presence of neutrons, it must balance its energy state. The way in which atoms do this is known as radioactive decay. Radioactivity of a material may be thought of as a process of releasing energy to stabilise the nuclei of atoms. Energy is released by three mechanisms. These are known as Alpha (α), Beta (β) and Gamma (γ).

Heavy atoms have nuclei that contain a large number of protons and neutrons. The nuclei can become unbalanced due to the existence of neutrons and therefore need to reduce their energy state. The simplest way in which the nuclei can become balanced is by acquiring more electro-static charge. This is accomplished by discharging a neutron to form a proton, and then taking in an additional electron from the surroundings to balance the positive charge of the new proton. This atomic discharge is known as beta radiation. When this occurs, the atomic number of the atom increases, meaning that a new heavier element has been formed. However, for heavy elements, an increase of atomic number is often not sufficient to balance the nucleus of the new isotopes, and therefore further energy reduction may be needed. Sometimes this occurs by more beta radiation but in other cases, it may occur by one of two further radioactive decay processes. The first is gamma radiation that releases energy as an electro-magnetic pulse

in the form of light or x-ray; this commonly follows beta decay. The second is alpha radiation in which an alpha particle consisting of two protons and two neutrons is forcibly ejected from the nucleus; this is always followed by beta decay.

The radioactive decay processes are naturally occurring in all elements as all elements can have unstable isotopes, however, it is the elements of high atomic number that decay most quickly. The rate at which an element will decay is a measure of its stability that can be expressed statistically. Elements that are undergoing radioactive decay often go through many stages of radiation before stability is achieved. In a bulk material undergoing decay, the decay of one atom initiates the decay of another atom, creating a complex decay chain. Initially the decay of the material may be fast, but as more atoms in the bulk material achieve stability, the decay chain begins to slow. This is shown in Figure 2.
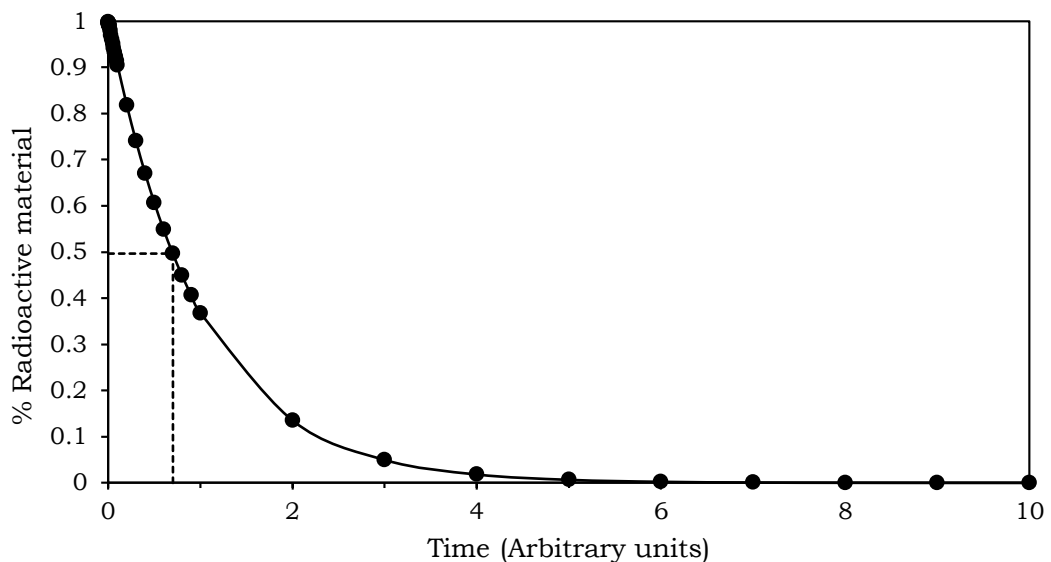
Figure 2: The idealised characteristics of bulk material undergoing radioactive decay

The exponential decay characteristics imply that to calculate the total time required to complete the decay chain would contain a very large degree of uncertainty. However, the near linearity of the initial, fast decay chain makes it possible to calculate the time required for half the material to become stable with high accuracy. This measure is named the radioactive 'half-life' of the bulk material, and may have magnitudes of fractional seconds to millions of years depending on the material; the shorter the half-life the quicker and more intense the radioactive decay.

The radioactivity of elements had been discovered during the late 19th century in work by Henri Basquil, and following the discovery, continued work through the 19th century, first by himself then by Marie and Pierre Curie and others, knowledge was attained on the phenomenon of radioactivity. It became apparent that radioactivity was a property of materials and that radioactive decay processes possessed the potential to release huge amounts of energy. It was thought that this energy could be used to benefit humanity, however, during this time, the half-lives of naturally occurring elements were not short enough to yield usable quantities of energy, and usable quantities of more volatile radioactive materials could not be attained. During this period in the history of nuclear developments, a process from which the energy released in radioactive decay could be harvested was not known, but by the beginning of the 20th century, advances in knowledge and technology delivered a solution.

2.1.2   Nuclear fission

In 1905, Albert Einstein published the paper "Does the inertia of a body depend upon its energy-content?"[1]. In this paper Einstein proposed a theory in which the energy and mass of matter were related

and equivalent. The modern version of energy/mass equivalence in the well-known and simplified form is written:

$$E = MC^2 \tag{1}$$

Where E is the energy, M is mass, and C is the velocity of light in a vacuum. At the time of writing, Einstein's theory did not spark immediate interest, however, the magnitude that the theory of energy/mass equivalence would have on the future would be great. It was not long after this paper was published that a method of harvesting significant quantities of energy from radioactive decay processes was discovered. The theory of energy/mass equivalence was the theoretical understanding of this process [2], and today is known throughout the world.

During the decades that followed the discovery that radioactivity was a property of elements, research into the structure of materials and atoms provided knowledge into radioactive processes, and in the 1930's, radioactivity of materials was identified as the radioactive decay of atoms [3]. It was found that the decay process produced a number of particles which were emitted from decaying atoms, and that these particles possessed a large amount of energy. In 1938, two German scientists, Otto Hahn and Fritz Straussman, discovered a way in which this energy could be harvested. The two scientists were experimenting with the metallic element uranium, which is the heaviest naturally occurring element on earth. Uranium has the atomic number 92, and is an element known to be radioactive. Their experiment aimed to characterise the effect of bombarding the uranium with free neutrons by studying changes of radiation. During the experiment they detected beta radiation and assumed that a new heavier element had been formed, however, when analysing the

specimen following neutron bombardment, they identified the element barium. Barium did not exist in the specimen before the experiment but what was more notable was that barium had an atomic number of 56, much less than the original uranium. Following further analysis and consultation, this result was published as evidence that uranium atoms could be split by neutron bombardment into two smaller atoms, and that when this occurred, the atomic masses of these lighter elements did not equal the mass of the original uranium atom.

What was discovered is that neutrons can be captured by the nucleus of the uranium isotope 235 (^{235}U). This additional neutron put the nucleus into such instability that it began to split into two parts via a necking phenomenon. As the two new nuclei developed, the distance between the two evolving nuclei increases and they are pushed apart by their positive charges [2]. At the point of splitting, the two new nuclei are driven apart violently, hitting surrounding atoms and causing the bulk material temperature to increase. In the split 2-3 neutrons are also released, while the new nuclei further stabilise by emitting radiation. The specific reaction identified by Hahn and Straussman can be written as [4]:

$$^{235}_{92}U + n \rightarrow {}^{236}_{92}U \rightarrow {}^{143}_{56}Ba + {}^{90}_{36}Kr + 3n \tag{2}$$
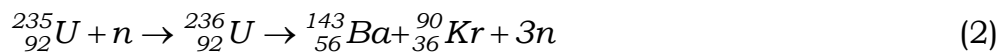
The neutrons released during the split can then go on to split further uranium atoms, and so a fast chain reaction delivering large quantities of energy was possible. It is known today that the splitting of ^{235}U results in a number of different product atoms, however, regardless of the product, Einstein's theory of energy/mass equivalence showed that the change of mass between the parent and product atoms resulted in an energy release of approximately 1MeV per atomic split. The discovery sparked immediate attention throughout the world as

splitting uranium in this way could be used to harvest the large quantities of energy already known to exist within decay processes. This process became known as nuclear fission.

In the few years that followed the discovery of nuclear fission, much research was completed. What was discovered was that neutrons were not only captured by ^{235}U but also by the heavier uranium isotope ^{238}U. In this case, the capture of neutrons did not cause a split of the atom, but instead caused decay of ^{238}U by beta radiation. The element that was produced was number 93 and was named neptunium. Neptunium had an atomic mass of 239 and was also unstable and decayed by beta radiation almost instantly into the well-known element number 94, the specific isotope being plutonium-239 (^{239}Pu). This plutonium isotope was found to be highly radioactive and could be split by fission; however, producing plutonium on a large scale would require significant technological developments. Natural uranium however was mostly ^{238}U with concentrations of the fissionable isotope ^{235}U being only a fraction of a percent of mass at best. Natural uranium therefore required enrichment in ^{235}U before significant energy could be harvested from it using the fission process, which also required technological development. It was not long before the developments arrived.

2.1.3   Nuclear technology

In 1942, the Second World War began a race for the development of nuclear technologies. This race manifested as an endeavour to produce weapons from the energy released in fission, and resulted in the production of the atom bomb. The energy that could be harvested from fission was known and it was postulated that an accelerated chain reaction of a larger and pure quantity of a fissionable material would produce an energy release of immense magnitude. During the

development of the atom bomb, two paths from which fuel for the bomb could be produced were identified. One of these paths was to enrich the metallic element uranium to produce a near instantaneous release of energy from large quantities of ^{235}U; the other was to produce the fissionable plutonium isotope ^{239}Pu from ^{238}U. The development of the atom bomb was a collaboration between the allied forces and progress was swift. Both paths to the atom bomb were followed; the production of ^{235}U lead to a diffusion based enrichment process while the production of ^{239}Pu led to the development of nuclear reactors. In 1945 two atom bombs, one developed from each type of fuel were ready. These were dropped on Japan, ending the war in the east.

After the war the collaboration of the allied forces ceased and development of nuclear technologies continued independently by individual nations. Initially this development was towards nuclear weapons technology, but it was quickly realised by all nations that the production of plutonium using a nuclear reactor developed a large amount of heat, and that this heat could be used to do work [5]. Initially it was thought that this heat could be used to subsidise the power demands of running a nuclear reactor, however, the needs and requirements of power production, and those of plutonium production proved to be uniquely different, and it was not long until civil nuclear power became an independent direction in the development of nuclear technologies. This resulted in the world's first civil nuclear power programme that was announced by the UK in February 1955.

2.1.3.1 Nuclear reactors

The controlled energy released by fission of ^{235}U within a nuclear reactor is a continuous heat source. The heat released in fission is transferred to a primary coolant in the reactor pressure vessel that is circulated through a heat exchanger. Within the heat exchanger, the

heat is transferred from the primary coolant to a secondary cooling circuit containing water, which boils and generates steam. The primary coolant is circulated back through the reactor core, and the steam generated in the secondary circuit is used to drive a gas turbine. The secondary coolant then is condensed and recirculated. The turbine is used to drive an alternator-generator that produces electrical power. This is shown schematically in Figure 3.
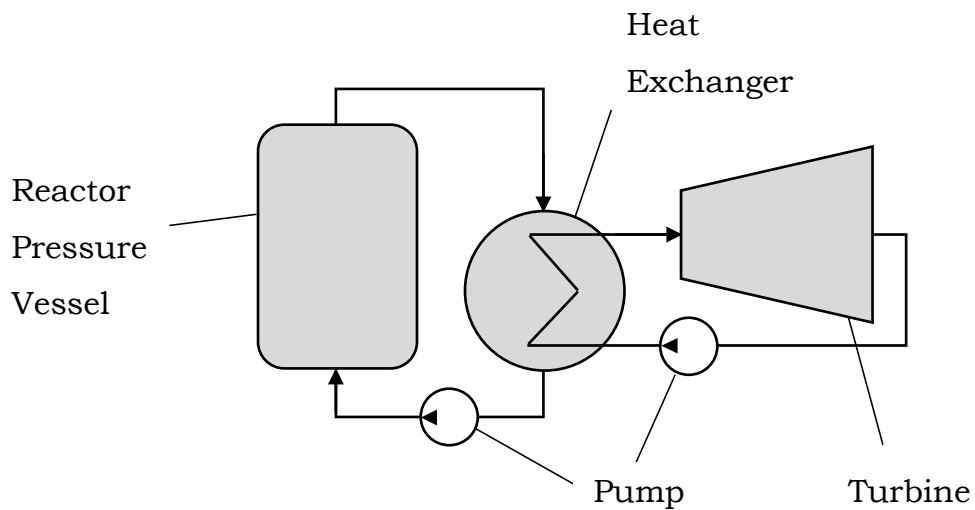
Figure 3: Schematic of a nuclear power plant

The technology is almost identical to power generation by fossil fuels, only differing in heat source; however, the independent developments of civil nuclear reactors have led to a variety of different technologies. These technologies are categorised as either thermal reactors or fast reactors, and within each category exists a number of unique variations.

2.1.3.2   Thermal reactors

It was identified very early that for efficient capture of neutrons by ^{235}U, the free neutrons should have a near equal energy state to ^{235}U atoms. Since the quantity of ^{235}U in natural uranium was so low, and that

large fraction of ^{238}U isotopes captured neutrons, it became necessary to slow the velocity of the fast neutrons released in fission to match the energy state of ^{235}U atoms. This increases the probability of released neutrons being captured by further ^{235}U atoms, sustaining the chain reaction. The slowing of fast neutrons in the reactor core was achieved by a moderator. In a nuclear reactor, the moderator is a material that does not readily capture neutrons but instead, slows the velocity of fast neutrons by atomic collisions. Nuclear reactors that moderate fast neutrons are known as thermal reactors and these reactors burn ^{235}U to generate heat.

The independent efforts of nations after the war resulted in a number of different forms of thermal reactor. In the USA, developments resulted in the use of water as both the primary coolant and moderator; while in the UK, carbon dioxide was used as the primary coolant and graphite as the moderator. The reactors that use water as the moderator are collectively known as light water reactors (LWR's). These can take the form of pressurised water reactors (PWR's) or boiling water reactors (BWR's). PWR's operate as shown schematically as shown in Figure 3; however, BWR's eliminate the need for two coolant circuits by allowing boiling to occur within the reactor core. Reactors that use CO_2 as the primary coolant are collectively known as gas-cooled reactors. These take the form of MAGNOX and advanced gas-cooled reactors (AGR's).

Thermal reactors require fuel that is enriched in ^{235}U to operate. The moderation of fast neutrons increases the probability of neutrons becoming captured by ^{235}U atoms; however, the capture of neutrons by ^{238}U does still occur. This produces ^{239}Pu that is undesirable due its high radioactivity. Fuel is shuffled around the reactor core to limit the build-up of ^{239}Pu, and to ensure the ^{235}U fuel is burned evenly throughout the core. Despite these efforts, the fuel must still be

removed from the core before the ^{235}U fuel is fully burned, and therefore efficiency is of concern, as is the high radioactivity of the spent fuel upon removal from the core. In the UK and France, spent fuel is reprocessed to separate the usable uranium from plutonium and fission products. However, no other nations reprocess spent fuel due to concerns with safety, and security regarding the production of plutonium that can be used for weapons manufacture. Due to these reasons many are in agreement that current thermal reactor technology is not sustainable for the future of nuclear energy [6].

In order to make thermal reactor technology sustainable, significant improvements must be made to their operational limits. Higher operating temperatures, higher fuel burn up and higher operating pressure will all increase the performance of thermal reactor technology [7,8]. However, these improvements put additional pressures on the components of the nuclear reactor, which must be addressed for nuclear technology to progress.

2.1.3.3   Fast reactors

Nuclear reactors were initially developed to produce ^{239}Pu from neutron capture and beta decay of ^{238}U. It was known from early developments that ^{239}Pu was fissionable and therefore a reactor that could produce and fission ^{239}Pu could produce large amounts of heat. Furthermore, the capture of neutrons by ^{238}U would be desirable, and moderators would not be required. This form of reactor became known as the fast reactor as fast neutrons realised in fission were not slowed by a moderator within the process.

This technology was realised early for civil power generation and was tested at a small scale with success; however, the technology has remained undeveloped due to complications with scaling. The fission

process within a fast reactor is more volatile than that of a thermal reactor due to the increased quantity of neutron capture. The process produces much larger quantities of heat, which requires coolants that possess increased conductivities over the water and gas used by thermal reactors. In addition, the fuel must remain in the reactor core for much longer periods to allow sufficient production and fission of plutonium, and this puts increased pressures on component properties within the reactor core.

Fast reactor technology has many benefits over the thermal reactor design. Firstly, it can burn more of the fuel in the reactor core and is therefore more efficient. The fuel also is less radioactive upon removal from the core due to the increased burnup, and the process produces more heat and therefore more power can be generated, increasing efficiency further [9]. An observant reader will also realise that the fuel for fast reactor technology does not require enrichment processing, and with this is mind, it follows that it is also possible to use spent fuel from thermal reactors to fuel fast reactors. There already exists a large quantity of depleted uranium fuel in storage throughout the world. This can be reused, eliminating the need for controversial fuel reprocessing.

Fast reactor technology is seen by many to be the future of nuclear energy as the benefits over current thermal reactor technology suggest sustainability [10]. However, fast reactor technology and advanced thermal reactor technology increase the demands placed upon the components of the reactor, and this is the limiting factor to the progress of fast reactor technology.

2.1.4 Nuclear advancement

Since the development of civil nuclear fission reactors following the war, the acquisition of knowledge in the field of nuclear energy has been continuous. The technological process is described as a series of generations within time: The 1st generation reactors were the post war experimental reactors. Generation 2 reactors were the first generation of civil power reactors that were developed in the 1960's and were put into service during the 1970's-1980's. Generation 3 reactors were designed in the 1980's and put into service during the 1990's and 2000's [11,12]. All generations were designed to have lifecycles of 30-40 years, but many have had their lifecycle extended to 60 years, especially in the USA. Despite controversial lifecycle extensions, most Generation 2 reactors are now in their period of decommissioning, and so preparations for the next generation of nuclear systems are underway.

Generation 4 reactors are reactors technologically advanced over current systems, and as may be remembered, have improvements in terms of increased operating temperatures and pressures, and increased burnup of fuel. The scope of Generation 4 reactors is under the guidance of the Generation 4 International Forum (GIF) who have identified several possible systems which meet the criteria of technological advancement [13] (Table 1).

Table 1: Proposed Generation 4 systems [14]

Reactor system	Coolant	Reactor type	Operating temperature (°C)
Gas-cooled fast reactor (GFR)	Gas (He)	Fast	~850
Lead-cooled reactor (LFR)	Liquid metal (Pb, Pb-Bi)	Fast	550-850
Moten salt reactor (MSR)	Molten salt	Thermal	700-800
Sodium-cooled fast reactor (SFR)	Liquid metal (Na)	Fast	~550
Very high temperature reactor (VHTR)	Gas (He)	Thermal	>900
Super critical water cooled reactor (SCWR)	Water	Fast/Thermal	350-620

These systems fulfil the criteria of generation 4, however the physical application of these systems raise some important issues. For example, it is noted that the operating temperatures of these systems are much higher than generation 3 systems, and that for the fast reactor systems, the coolants are more reactive than the inert gas and water systems used in generation 3. On paper, these systems are improvements on existing technology, producing more energy and being more efficient, however, this improvement puts increased stresses on the components of each of the Generation 4 reactor systems, and this presents a significant barrier for physical development. There have been many reviews into the materials challenges faced in developing advanced reactor systems [8,11,14,15], and progress is being made, however, the scale of reactor components and the longevity of their service creates uncertainties of suitability, and therefore there is resistance to the application of new materials, which is slowing developments of advanced nuclear systems.

Every year the International Atomic Energy Authority (IAEA) publish statistics about the global fleet of nuclear reactors [16]. In Figure 4 is displayed the 2017 data which shows how the number of reactors and the summed net power output of the global fleet have varied since 1985.
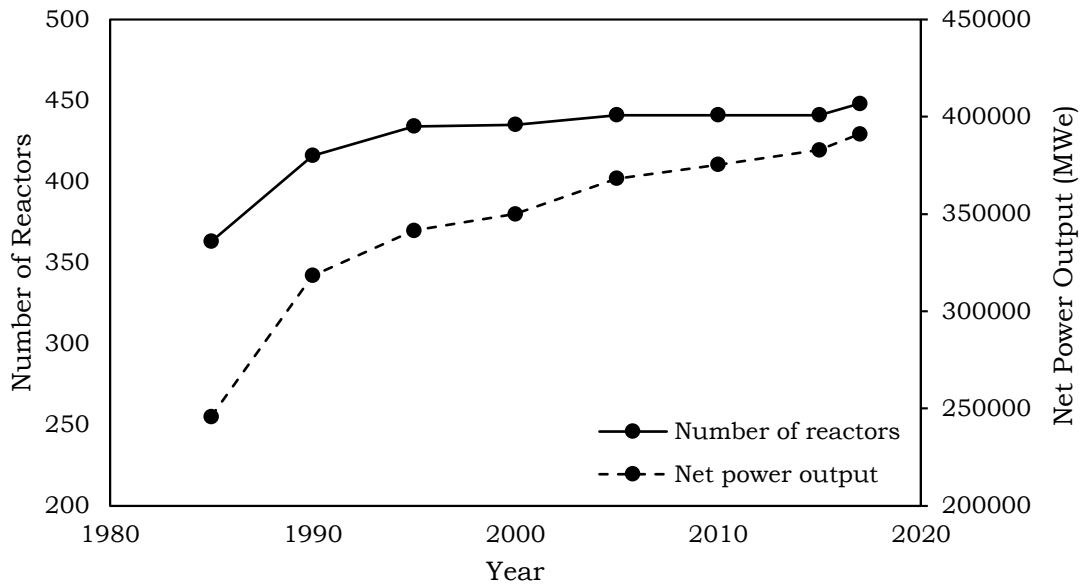
Figure 4: The variation of the net global nuclear power output and the number of nuclear power reactors worldwide from 1985-2017.

Figure 4 shows that the net power output has increased more quickly with time when compared to the number of operational reactors; the growth of power between 1985 and 2017 is ~59.13% while the number of reactors has only grown by ~23.42%. This is due to technological advancements in civil nuclear power systems, however, this trend also implies that technological advancements are necessary for continued growth, and so the next generation of nuclear power reactors must be realised for growth to be achieved. For generation 4 systems to be applied commercially, the materials required for their construction must be developed. This means that new and innovative analysis methods are needed, that can be used to rapidly investigate the applicability of new materials in nuclear applications, reducing the

uncertainty of new materials in service, and contributing to the growth of the civil nuclear energy.

2.2   REACTOR PRESSURE VESSELS

2.2.1   Introduction

In the previous section, the general layout of a nuclear fission reactor system was discussed. A key safety critical component within this system is the reactor pressure vessel (RPV), which serves as the primary containment of the reactor core. The environment within the RPV is very hostile combining high levels of radiation, neutrons with energies up to 3MeV, and high temperatures. Furthermore, it cannot be replaced during service and thus is a life-limiting component of all nuclear fission reactors.

RPVs are very large and have increased in size through the generations of nuclear design, and as power capacity has increased. A good example of this is seen when reviewing nuclear reactors in the USA, who have employed a substantial civil nuclear power program and been involved in nuclear technology from the Second World War. Figure 5 presents selected data [17,18] that shows how the scale of USA's PWR RPVs have changed as a function of both time and power capacity. Figures 5a) and 5b) show how typical RPV dimensions have grown with respect to time and power capacity. The different generations are indicated, however, when plotting power capacity against time along with the RPV growth, Figure 5c), the trends have disproportionate growth rates and show that the power capacity of plants in the USA has increased more quickly than the thickness of the RPV, over the same time period.

a)

b)
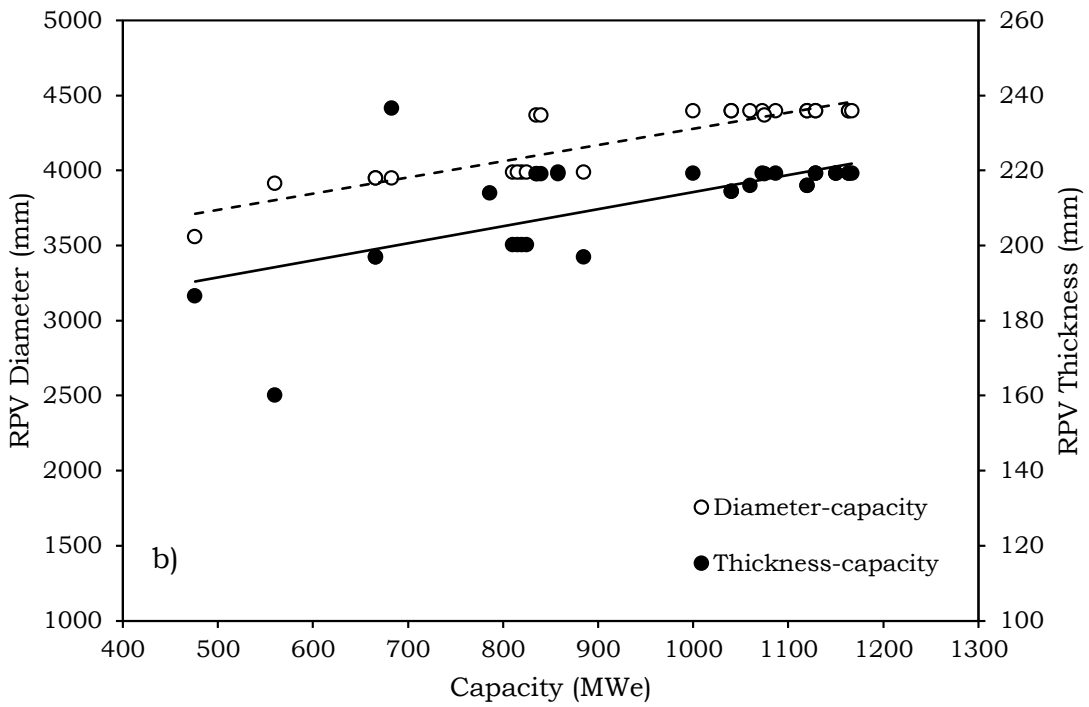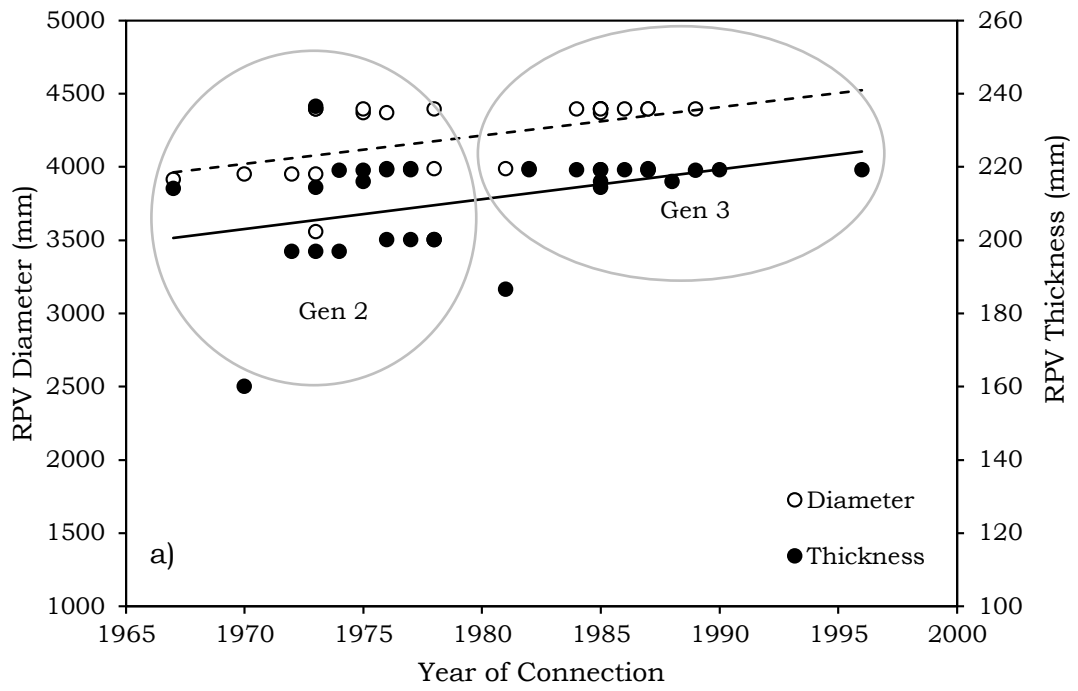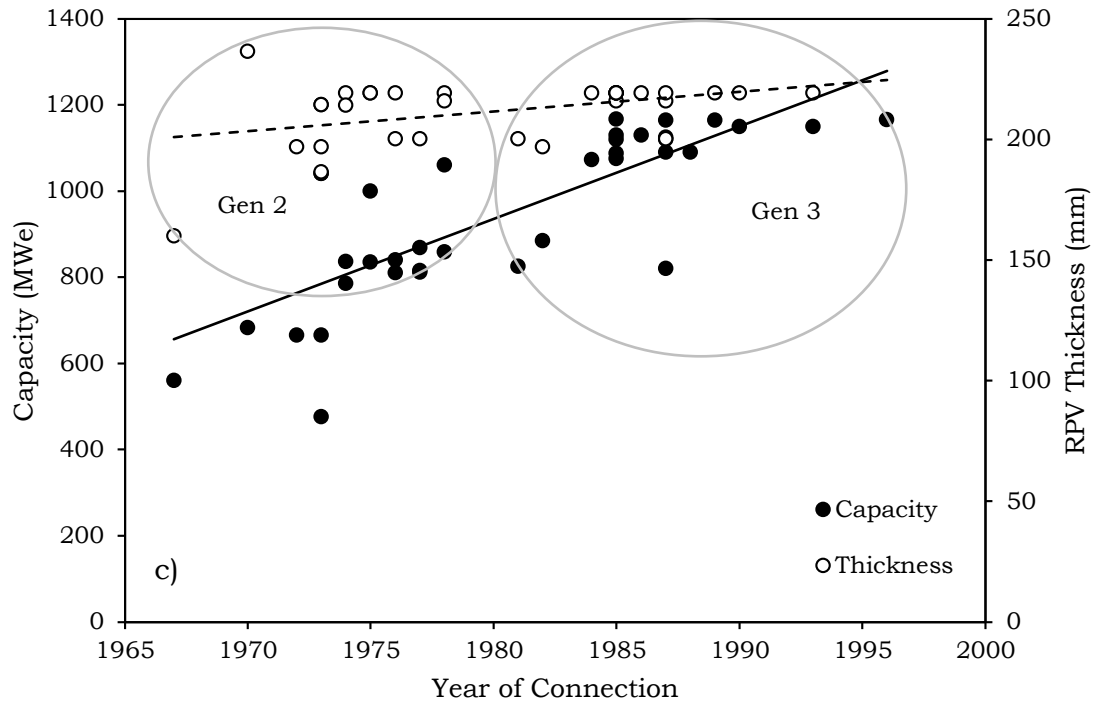
Figure 5: Selected metrics for PWR power plants in the US [18]

This observation implies there is a limitation to the growth of civil nuclear energy, however, the data does not reflect the many technological advancements achieved through the same period. As previously mentioned, there have been many researches focussed on advancing RPV technology, and since the birth of civil nuclear power generation, many significant advancements have been applied. The RPV design, steel and ingot making and manufacturing processes have all seen the attention of research. The result of this work is that the properties and in-service performance of the RPV have improved, and the dimensional growth of the RPV component has slowed. In present times, the growth of generation 3 PWR power capacity has increased to 1600MWe with the new European Pressurized Water Reactor (EPR) [18,19]; more than 1000MWe greater than the early Generation 2 plants. The majority of the Generation 2 plants are now being decommissioned and technologically advanced replacements are in development; however, while research has allowed technological advancement to be made in this period, the data in Figure 5 show that

there is a limiting factor for continued growth, and therefore continued research is needed if growth is to be sustained.

2.2.2   RPV development

In much of the world where nuclear fission power is exploited, the standard which governs the manufacture, building and testing of RPVs is the American Society of Mechanical Engineers (ASME) Boiler and Pressure Vessel Code (BPVC) [20]. Early RPVs followed generic standards for pressure vessels, however, in 1963 the specific section III that governs nuclear power plant components was added to the code [20,21]. Developments to the code have occurred often through biannual reviews. These are included as addenda initially, but become part of the code after 6 months [21]. These include many discrete changes that have improved the function and performance of RPVs. For example, since the development of fracture mechanics, many design criteria for RPVs have changed from a design by rule criteria to a design by analysis criteria, which identifies different stress categories. RPV components are designed to satisfy stress limits [22] set by these categories, and has led to a reduction in the overall Factor of Safety (FOS) from 5 to 3 in modern times. The effect is a substantial material saving, which in turn has improved the overall capacity of nuclear reactors. Another important change is the fabrication of RPVs. Many of the Generation 2 RPVs were fabricated from formed A533 steel plates that were welded together. However, this meant that longitudinal seam welds were present along the belt line of the RPV, an area of high stress. Modern RPVs are now fabricated from a number of mono-block ring and shell forgings, which are welded circumferentially, as shown in Figure 6:
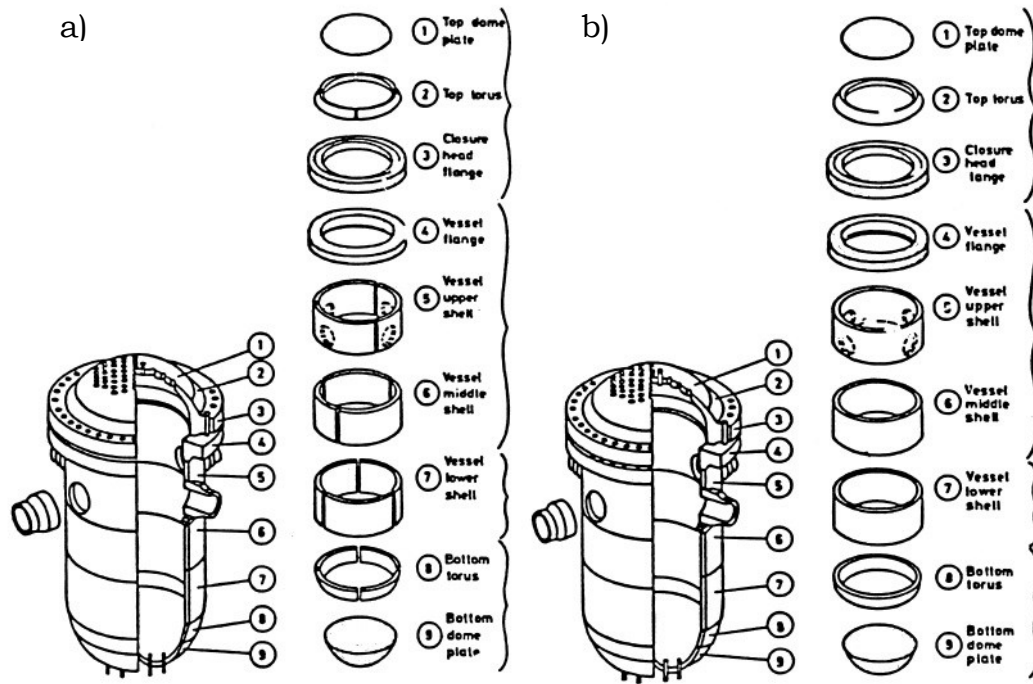
Figure 6: Typical PWR RPV fabrication. a) From formed plate. b) From mono-block ring forgings [17,23].

This improvement has led to an upgrade in the materials used in RPV manufacture and currently, the ASME standard is A533 for plate components and A508 Grade 3 Class 1 for forged components. The factors that determine the final properties of RPV components are the chemistry of the specific alloy and thermo-mechanical history. A flow chart depicting the manufacture of a modern RPV ring forgings is shown in Figure 7 [24].

A large number of processes contribute to microstructure evolution in RPV components, and it follows that large numbers of variables require understanding to ensure that high quality RPV components result from manufacture. These variables may be summarised under the headings of: 1. Steel and ingot making, which determines composition. 2. The forging route, which develops the form of the component and contributes to microstructure evolution. 3. Quality heat treatment, which develops the final microstructure in the component.

38

1. Ingot making.

2. Solution HT.

3. Discard ends.

6. Trepanning.

5. Upsetting.

4. Cogging.

7. Becking

8. Drawing

9. Expanding.

12. Final Machining.

11. QHT

10. Rough Machining.

Figure 7: The production route of a typical RPV ring forging

2.2.2.1 Steel and ingot making

The shift of RPV manufacturing from formed plate components to mono-block ring forgings has facilitated the growth of civil nuclear energy because of the reduced FOS, and because of the increase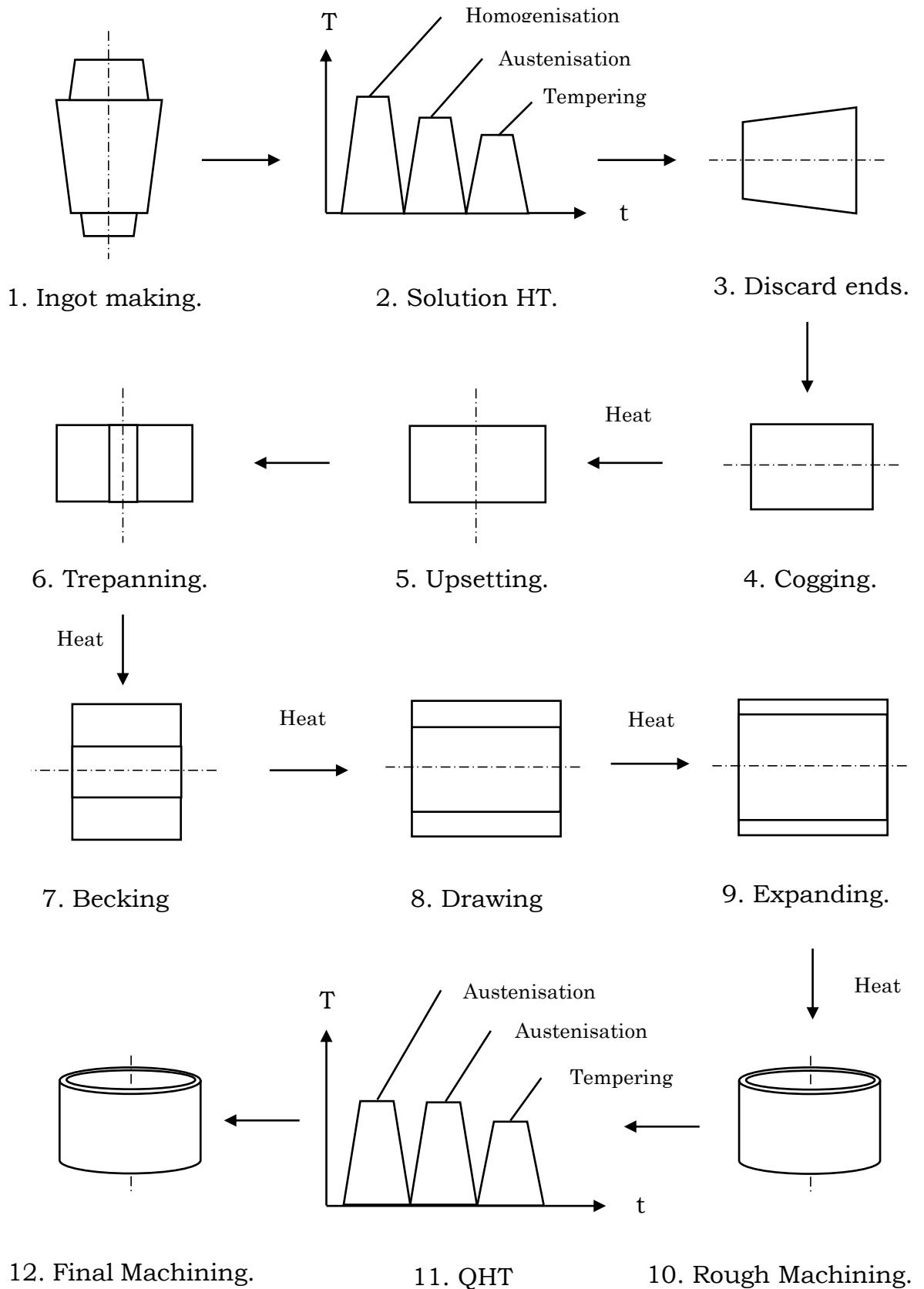d quantity of forged components. However, as capacity increases it is necessary to produce larger forgings, and all of these are made from cast ingots. An good example is the nozzle shell forging made for the EPR at Japan Steel Works, which was made from a single ingot weighing a world first of 600 tonnes [19]. The properties of the final component are a function of the composition of the steel, but are affected by macroscopic segregations that occur during ingot making, most notably longitudinal solute enrichments and A-type segregates. However, there has been continuous improvements in steel and ingot making that in modern times have summed to produce very high quality components. For RPVs, some specific advancements are standardised, however, within the standardised ranges of composition and procedure, discrete variation has effects on the final properties.

2.2.2.1.1 Steelmaking

When in a liquid form, iron and the alloying solutes that form steel are in solution, however, when solidification occurs the solubility of these additions within iron reduces, resulting in precipitation. An element of specific importance in steelmaking is the interstitial element, oxygen. This element when leaving the iron matrix either coalesces to form voids or precipitates to form a brittle FeO phase, both of which are undesirable in ingots destined for high quality forgings. The methods to eliminate the deleterious effects of oxygen are standardised for RPV's forgings in ASTM A508 [25], and more generally for forgings in ASTM A788 [26]. These methods are known as Vacuum Carbon De-oxidation (VCD) and killing, both of which affect microstructure evolution.

Traditionally, de-oxidation of steel is achieved by the process of killing. In this process, an element with affinity to oxygen is added to the liquid steel to be precipitated with it. Commonly used elements are silicon (Si), aluminium (Al) and manganese (Mn), however the additions and their products have an effect on microstructure evolution and hence, mechanical properties. VCD was introduced to remove the oxygen without oxygen killing additions, by vacuum treating the liquid steel. In this reaction, oxygen combines preferentially with carbon to form CO. This process had the benefit of greatly improving segregation of all forms, however, in the absence of large quantities of precipitates, it was found that VCD led to increased austenite grain growth affecting transformation kinetics upon cooling, hence material properties.

There has been much research conducted in terms of the effect of killing additions and VCD, and combinations of both in many forms. A good example was the work by Houchstein et al. [27] who used a new procedure of injecting Al to molten steel alloy 20MnMoNi55 (a German specification for the A508 alloy) after VCD. The results suggested that the VCD with Al addition formed a steel that possessed all the benefits of VCD, with the refined grain structure of a killed material. They compared the results through microscopy and impact testing to an Si killed steel and showed this well, however they did not speculate as to the mechanisms of this success.

A similar investigation was under taken by Kim et al. [28,29] studying three A508 Grade 3 RPV shell forgings manufactured using VCD, VCD+Al and Si-killing. Properties were improved in VCD+Al and Si-killed steels over VCD alone due to grain refinement, but they noted little difference between these in terms of mechanical properties. They postulated that in the absence of oxygen, Al combined with nitrogen to form AlN precipitates that pinned grain boundaries. However, while cited, evidence to support this was not presented.

Pous-Romero et al. studied austenite grain growth in A508 grade 3 [30]. They found that grain growth was retarded below ~940°C due to the presence of AlN precipitates pinning grain boundaries. Above this temperature, increased growth implied the dissolution of these particles, allowing austenite boundaries to move freely and grains to grow. The processing steps applied to the material were not discussed, however, the measured chemistry possessed low quantities of sulphur and phosphorus implying a modern clean steel, which for conformation to ASTM specifications, would have been both killed, and cast using VCD.

2.2.2.1.2 Ingot making

When ingots solidify and cool, they do so from the surfaces of the mould. This creates temperature gradients and convective fluid flows during solidification and are often aided by density gradients caused by newly formed solute depleted grains sinking, and causing less dense, solute enriched fluid to rise. It was previously mentioned that macro-segregation in the form of positive and negative solute segregation, V-segregates and A-segregates do occur in ingots, and while the specific chemistry and the processes used are shown to affect the presence of these segregations, the ingot mould geometry remains an important variable. The typical segregations that commonly occur in cast ingots along with their locations are shown in Figure 8:
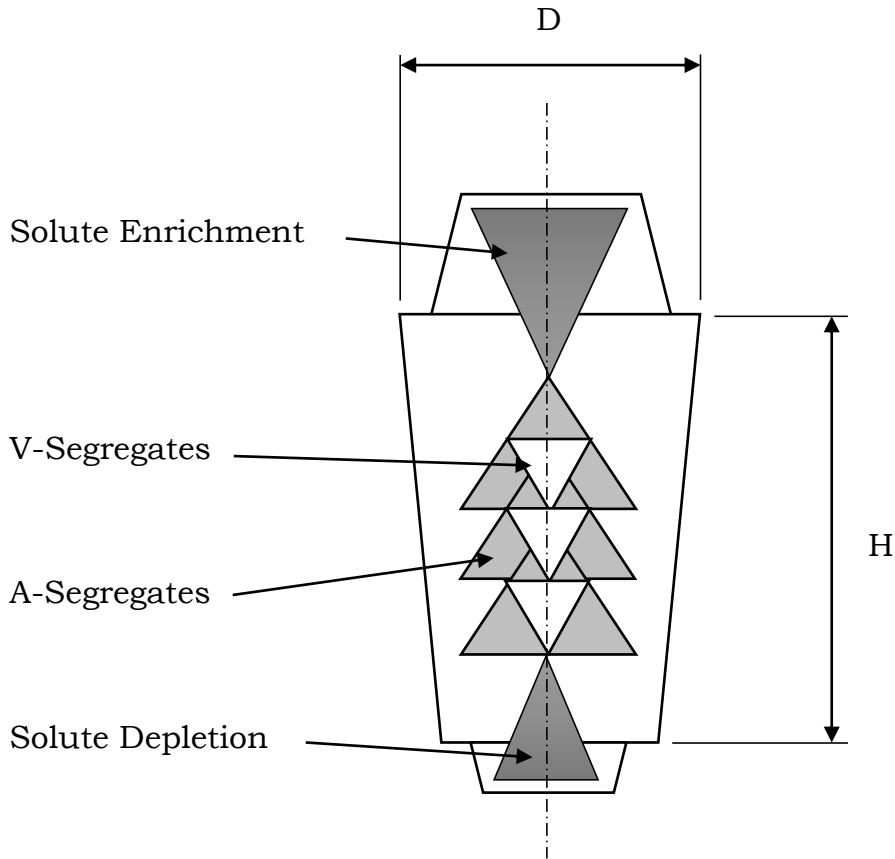
Figure 8: Typical segregations found in large cast ingots [31]

The ingot mould geometry has an important role in controlling the formation of these segregations and thus, on the properties of a high quality forgings. Ingot moulds are designed to have large surface areas to shorten solidification times; however, the dimensions of the mould in terms of height, diameter and conicity are critical variables in terms of segregation. For each component to be forged, the ingot mould must be uniquely optimized with respect to segregation and porosity. For example, ingots for hollow products such as RPV ring forgings require a high level of chemical homogeneity. The conicity of the mould should then be low to the limit convective flows that generate A-segregates, and the height/diameter (H/D) ratio should be large to avoid positive and negative enrichment, ensuring chemical homogeneity in the centre portion of the ingot. This can be seen in Figure 7, where both the top

and bottom of the ingot are removed to reduce positive and negative segregation in the forging. Similarly, the trepanning operation removes much of the A and V-segregates from the ingot. Further forging breaks up the remaining segregation, however, over large length scales solute concentrations cannot be distributed homogenously by any known process and some positive and negative solute enrichment, and some A-segregates, remain in the finished component [24].

In 1979 Suzuki et al. studied the formation of A-segregates at a laboratory scale [32]. Their experiments sucked the liquid metal from a number of partially solidified low alloy steels, and measured the composition of the solidified and sucked material respectively. Results indicated that a reduction of Si, or an increase of Mo, caused solute enrichment of the inter-dendritic fluid ahead of the solidification front to become reduced. It was postulated that the density difference between the inter-dendritic fluid and the bulk fluid remained small as a result, which lowered the driving force for the solute enriched liquid becoming segregated from the bulk. It was concluded that the formation of A-segregates was affected by composition and could therefore be controlled, however, the work was completed in a laboratory and did not consider the effects of temperature gradients and scale, of RPV ingots.

A simple way to avoid macro-segregation is to avoid the enrichment of the inter-dendritic fluid altogether. However, the only way to achieve this is by cooling at rates fast enough to retard diffusion of solute away from the solid/liquid interface during solidification. For RPV forgings, the ingot sizes are too large to achieve these rates through the entire thickness, and large temperature gradients occur as a result. In 1985, Maidhorn and Blind [33] published work which considered specifically the segregations which occurred in three large ingots cast in 20MnMoNi55 low alloy steel, which all underwent different procedures

during ingot making. They measured how carbon content varied across complete sections and connected identical values to plot iso-carbon contours for each ingot. Figure 9.
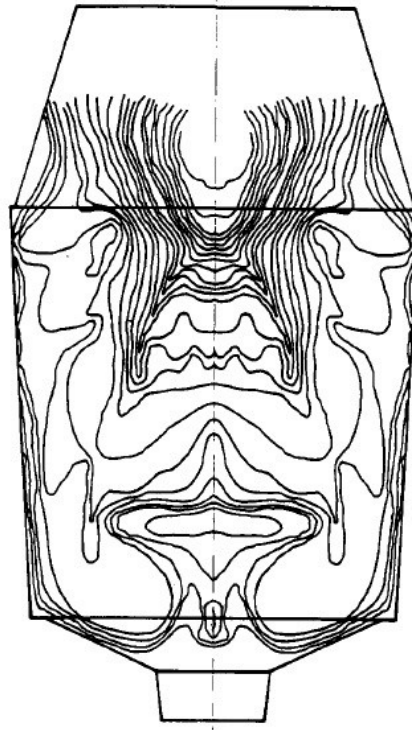
Figure 9: Iso-carbon contours inside a 180 tonne ingot [33]

Since the partitioning of carbon occurs during solidification of steels, each iso-carbon contour was plotted in sequence according to increased carbon content, and this was used to ascertain the solidification path of each ingot. Segregation was found to be unavoidable in large ingots, but it could be controlled using the process of hot topping. In this process, an exothermic powder is applied to the top of the ingot after casting. The powder provided heat, controlling the solidification path from bottom to top, and thus carbon segregation. The heavily enriched top and depleted bottom of each ingot are then removed, but this process cannot mitigate against segregation when the H/D ratio is incorrect. This was evidenced when high carbon regions in the mid-section of the third ingot were found,

causing the whole ingot to be discarded. The reason the third ingot was discarded is that macro-segregations have a strong effect on microstructure and mechanical properties, and for safety critical RPV forgings, property specifications must be met.

Many works have investigated the effect of segregation on RPV properties. In 1997 Ostberg published a review of many papers and discussed them in terms of the impact strength, resistance to crack growth and fatigue of RPV components [34]. The review was largely qualitative but highlighted that specific segregations, their locations and orientations, are specifically important to properties and hence RPV integrity. However, he did not discuss the metallurgical implications of these works in terms of the relationships between segregation, microstructure evolution and mechanical properties.

The metallurgical implications of segregation in A508 Grade 3 Class 1 were studied by Pickering [35] which included an investigation on the effect of A-segregates on microstructure evolution in a large A508 grade 3 cast ingot [36]. The results showed that bands of allotriomorphic ferrite were produced within the A-segregated regions, in comparison to the upper Bainite structure that was formed elsewhere in the microstructure. It was postulated that the allotriomorphic ferrite decreased fracture toughness by producing a continuous path for crack propagation.

2.2.2.2 Forging

Following steel and ingot making, the microstructure of the cast ingot contains composition variation and segregations as discussed in section 2.2.2.1, and has a coarse grain structure with low morphological homogeneity. This consists of internal equiaxed grains, columnar grains and small surface chill grains that are typical of as-

cast microstructures. Composition and microstructure are factors that affect mechanical properties, and poor homogeneity is deleterious and highly undesirable in high quality forgings. The primary purpose of forging is to form the ingot into the desired geometry; however, the forging process also breaks up inclusions and segregations, and facilitates recrystallization. The aim of the forging process is to form a quality component with excellent homogeneity of both composition and microstructure, with high dimensional accuracy.

Figure 7 shows a simplified flow chart detailing the production route of a RPV ring forging. Before forging can begin, an ingot must be made. Ingot making was discussed in section 2.2.2.1.2, and is always followed by a solution heat treatment. The next operation performed is to discard the ends of the ingot by an oxy-flame parting process. This removes a significant portion of the solute enrichments formed during casting, and removes a large proportion of the ingot weight. The ingot is turned by 90° to its axis and cogged to form either a cylinder, or hexagonal or octagonal cross-section bar. This operation works the material perpendicular to the ingot axis and breaks up the columnar grain structure created during casting by facilitating dynamic recrystallization.

The forging is then turned again, and upset in the axial direction to produce a thick disc. This operation prepares the forging for forming into the component geometry, and breaks up any remnants of the as cast microstructure, replacing it with recrystallized grains. In this orientation, the forging is then trepanned. This operation removes the axial centre of the disc to allow forging into a ring. Importantly, this operation also removes much of the A and V segregations from the component, further improving chemical homogeneity.

The forging is then placed on a mandrel and worked perpendicularly to the axis in a number of operations. The first operation is becking, which is completed to increase the bore of the component. During this operation, a forging tool is actuated parallel to the axis, increasing both bore and length, and reducing wall thickness. The component is rotated on the mandrel with each pressing of the tool to work the entire circumference of the forging.

Following the becking operation, the component is passed to a larger mandrel to be drawn to length. In this operation, the pressing tool is actuated perpendicularly to the mandrel, working its way along the component length. This increases the length of the forging at the cost of wall thickness; however, the bore of the ring remains constant.

When the forging has been drawn to the correct length, the component undergoes a final becking operation. This operation increases the bore and reduces the wall thickness to near net dimensions, while keeping the length constant.

The forging processes for large RPV forgings are designed to work the material equally in the axial and radial directions to produce anisotropy of microstructure throughout the forging. Following, the forged component is then machined into its final geometry, before being heat treated to generate the final microstructure.

2.2.2.3   Heat treatment

During manufacture, an RPV forged component undergoes two major heat treatment processes. These are shown in Figure 7 and are the solution heat treatment (SHT), completed after ingot making and quality heat treatment (QHT), completed after forging and rough

48

machining. The SHT is given to cast ingots to homogenise microsegregation of the microstructure following solidification, and to allow ultrasonic inspection. The QHT is applied to evolve the final microstructure and hence properties of the forging. Of these two the QHT is the most important, and there have been many researches investigating the effects of QHT elements on microstructure and mechanical property evolution [37–41].

A complete QHT consists of a number of unique austenisation and quench stages, followed by tempering and quenching. These processes are specified in the ASME BPVC SA-508 [42], the identical ASTM A508 standard [25], and the ASTM A788 [26]. The standards state that for the austenisation element of the QHT, the upper soaking temperature must be sufficient to develop a fully austenitic microstructure in the material, followed by quenching in a suitable liquid medium by immersion or spraying. No specific parameters are given for austenisation, however, for tempering specific soaking temperatures for different materials are detailed, with soaking times specified using a design rule criterion that relates to component scale.

The factors that affect microstructure evolution during the QHT are the soaking temperature, the soaking time, and the cooling rate achieved during quenching from soaking. The soaking temperature must be above AC_3 to produce a fully austenitic microstructure prior to quenching; however, a high soaking temperature promotes austenite grain growth that affects transformation kinetics. A negative contributor to austenite grain growth is the soaking time. For large forgings, faster rates of heating and cooling produce temperature gradients through thickness, because heat transfer through the component is controlled by conduction. Time is required to homogenise the component temperature, and so the component is soaked above AC_3 prior to quenching, however, increasing soaking

times at high temperature promotes austenite grain growth as was discussed earlier in work by Pous-Romero et al. [30]. If the soaking parameters are not chosen correctly, transformation kinetics can be significantly affected. AC$_3$ temperatures can be estimated for alloy chemistry using empirical formulae, or by modern modelling software such as JMatPro, however, temperature control is limited in large industrial furnaces. Austenisation temperatures are often given large tolerance limits which are in excess of these control errors, and are often well above AC$_3$. Grain growth during the austenisation stages of the QHT is normally mitigated by reducing the soaking temperatures for each austenising stage; temperatures can range between 860-910°C.

The cooling rate of the component during quenching is a very important parameter as the cooling rate determines transformation kinetics. QHT is always performed with the component in near net shape and in agitated water to maximise cooling rates, however, because thick components suffer thermal lag, cooling rates vary though thickness and with time, leading to variation of microstructure, and hence variation of mechanical properties through thickness. At the surface, rapid cooling produces martensite, while slower rates within internal regions allow more time for diffusion and therefore more ferrite is formed.

Tempering is required to relieve the residual stresses inherent of rapid cooling, increasing toughness at the cost of strength. The parameters of this treatment are strictly specified for a given material and have temperatures of between 600-650°C, with a soaking times specified for as 30 minutes for each inch (25.4mm) of section thickness. However, these parameters relate to an idealised tempering process, but in large forgings the temperature lag inherent of heating and cooling means

that the tempering parameters vary through thickness, often resulting in increased soaking times, affecting mechanical properties.

2.2.3 RPV materials

Many materials are specified for the production of RPVs. These have been chosen and/or developed because of a specific combination of strength and toughness. The most common alloy used is SA508 grade 3 class 1, which has been in service since the 1950's [23].

The mechanical properties for the SA508 Gr.3 Cl.1 are specified in standards previously discussed [25,26,42], and are achieved primarily by the addition of Mo. Mo is a substitutional solute in Fe and diffuses slowly below the A_3 solvus. This retards mass transport and slowing the nucleation and growth of reconstructive transformations such as ferrite and pearlite. During cooling, the result is an increased likelihood for displacive transformations. In SA508 Gr.3 Cl.1, this produces large quantities of the eutectoid morphology, upper bainite.

The insensitivity of a material to cooling rate is a property referred to as hardenability, and the high hardenability of SA508 Gr.3 Cl.1 permits upper bainite to be produced at relatively slow cooling rates. From an industrial perspective, this is the ability to meet material specifications across a large range of cooling rates and hence the large section thicknesses found in RPV components by an appropriate QHT. However, despite increased hardenability of RPV alloys, variations of cooling rate through thickness do produce variations of microstructure through of RPV components, and this produces variation of mechanical properties. This was shown by Byun et al. [43], who measured maximum variations of mechanical properties of 20% through the thickness of several RPV forgings measuring 250mm in thickness. Many modern components are thicker and so detailed

characterisations of the response of RPV materials as a function of specific heat treatments are necessary to ensure ASME standards are met. One common method of determining the effect of thermal gradients in RPV components during QHT is to characterise a material on a smaller scale using similar but idealised conditions, and infer the microstructure and mechanical properties at full scale, by monitoring temperature evolution during QHT. The material characterisation under these circumstances is developed into a continuous cooling transformation (CCT) diagram that graphically represents microstructure evolution as a series of transformation temperatures, identified for constant cooling rates. When a number of cooling rates have been tested, discrete transformation temperatures can be plotted as a locus of data points that separates the CCT diagram into a number of identifiable transformation fields. The microstructure of components can then be inferred by comparing cooling data recorded from full scale testing. There has been much work devoted to characterising SA508 Gr.3 Cl.1, producing a number of CCT diagrams. Three CCT diagrams obtained from literature [44–46] are compared in Figure 10.

Figure 10 shows that there is limited correlation between each CCT diagram, and while the transformation temperatures appear to converge at slower cooling rates, the differences are large at faster rates, with little correlation between the critical cooling rates at which discrete transformations occur. For example, ferrite is shown to exist in each CCT diagram but the critical cooling rates for the suppression of ferrite vary by over an order of magnitude between the three diagrams. This is an important observation as increased volume fractions of ferrite in SA508 Gr.3 are often postulated to reduce fracture toughness, e.g., as shown by Pickering et al [36].
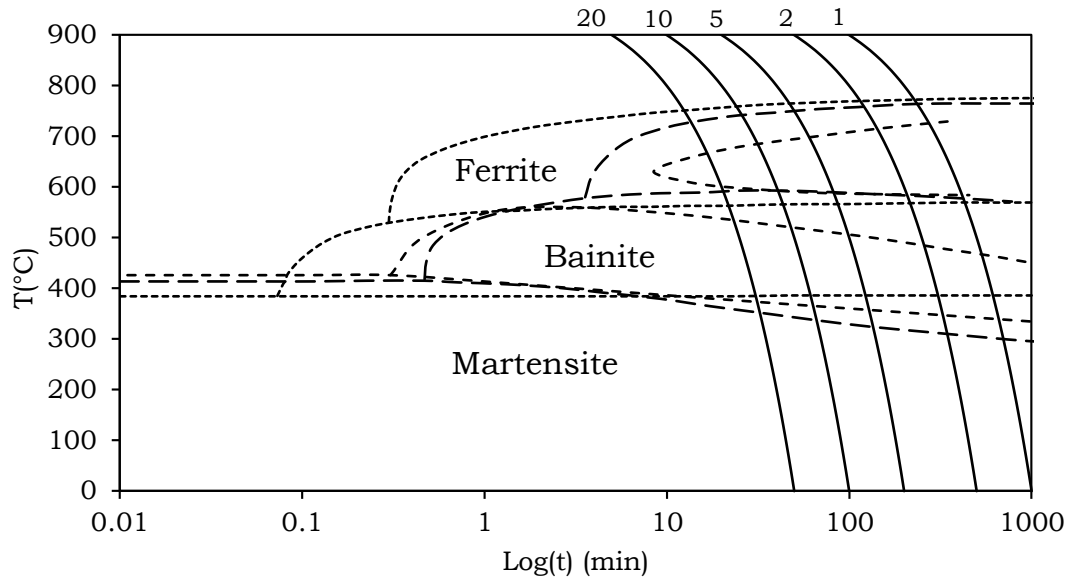
Figure 10: A comparison of published CCT diagrams for SA508 Gr.3 Cl.1. Francis et al. 2007. Suzuki et al. 2000. Haverkamp et al. 1983.

Kim et al. [28] investigated the effect of different steel making practices and heat treatments on the impact toughness of SA508 Gr.3. They tested samples that had thickness of 270mm, and recorded temperature evolution under heat treatment at a variety of depths using thermocouples. Results showed that impact energies rapidly reduced with reducing cooling rate below 30°C/min, implying that the onset of ferrite occurred at this rate, and that a proportionate increase in the volume fraction of ferrite occurred with further reductions of cooling rate. However, no ferrite was observed in the microstructures above 10.1°C/min under microscopic investigation. The work by Byun et al. [43] previously mentioned was published in the same year, and characterised the through thickness variations in mechanical properties of four 250mm thick SA508 Gr.3 RPV forgings made following different steel making processes. They did not present any temperature data or microstructure analysis for the locations, but stated that ferrite was observed in the third RPV at its mid-thickness. However, hardness testing showed that the Brinell number for that RPV at its mid thickness was greater than at the same location of the

other RPVs tested, implying that a fraction of ferrite could exist in these RPVs also. In addition, the hardness for all RPVs tested did not vary greatly from 0.2 thickness to 0.8 thickness locations, making a reasonable argument for the existence of ferrite through a large proportion of each RPV. Comparing this data to the CCTs in Figure 10 it is seen that the critical cooling rate reported by Kim et al. passes through the ferrite transformation field of all three CCTs, and since the thicknesses of Byun et al. specimens were comparable to Kim, it can be assumed that ferrite does exist in the forgings they tested.

Pickering et al. published work which looked into how segregation during casting of SA508 Gr.3 billets for RPV manufacture, affected the transformation characteristics of the material under heat treatment [36]. Specimens were sectioned across a region of segregated material taken from a cast ingot destined for RPV forging, and tested them at a constant cooling rate using a dilatometer. Ferrite was identified to form at a cooling rate of 6°C/min, regardless of the degree of segregation. In the same year, the ferrite formation in SA508 Gr.3 Cl.1 was studied by Pous-Romero et al. [47]. Using dilatometry, they tested specimens for a broad range of cooling rates and found that a critical cooling rate of 24°C/min was required to retard the formation of ferrite for a Prior Austenite Grain size (PAGS) of 13µm, and went on to say that ferrite could be retarded at 6°C/min by minimising the PAGS to 25µm. In Figure 10 we see that these rates produce ferrite according to the CCT diagrams presented, however, no PAGS's were included or discussed in those researches.

When reviewing the literature presented here, there seems to be little correlation on the transformation characteristics of SA508 Gr.3. Cl.1. However, a transparent argument requires that variables that affect the microstructure evolution of RPV materials must be discussed in

relation to the work. As discussed in previous sections, a number of variables that contribute to microstructure evolution in RPV materials, and the effect of different combinations of these variables is considerable. However, the differences between the CCT diagrams in Figure 10 cannot be rationalised by assessing these variables as they have been not been included; neither Suzuki et al, nor Haverkamp et al, referenced or discussed the acquisition of the CCT diagrams published as part of their work. The CCT diagram published by Francis et al. was modelled, and taken from work completed by Kim et al. in 2003 [48]. This work used a thermodynamic model refined by Li et al in 1998 [49], from original research by Kirkaldy et al. in 1984 [50]. The CCT is then a direct use of Li et al.'s formulation, and while that model was validated experimentally for a small number of low alloy steels, no such validation was completed by Kim et al. when modelling for SA508 Gr.3 Cl.1. A complete discussion on the topic of the thermodynamic modelling of transformation kinetics is beyond the scope of this review, but it is important to understand that it remains a developing field. It has shown notable acceleration and advance through time and much research has been completed and is ongoing [51-56], however, a constant within modern modelling of transformation kinetics are the validation stages applied for each new iteration. The CCT published by Francis et al. used a model that is old by comparison to the paper, and was un-validated for SA508 Gr.3 Cl.1.

The other works discussed here also show large variability. For example, the works of Kim et al. and Byun et al. in 1997 were completed on full-scale components, which as discussed, suffer from variable cooling rates through thickness. In Kim et al.'s work the cooling rate was specified between 800-500°C only, and for point measurements in a large object, while mechanically testing over much larger length scales. In Byun et al.'s work, cooling data was not presented at all. The work by Pickering et al. was designed to test the

effect of segregation on transformation kinetics, and it was successful in showing the significant effect of variable composition on microstructure evolution, but only on a small scale. The work by Pous-Romero et al. showed that the PAGS has a significant effect on transformation kinetics, and hence the effect of specific heat treatment parameters on microstructure evolution, but again the testing was on a small scale.

2.2.4 Summary

For large RPV forgings there are a large number of variables that contribute to microstructure evolution, and therefore mechanical properties. Predicting the final properties of individual RPV forgings is therefore also uncertain, as variability through thickness exists. The manufacturing processes and parameters used during manufacture of RPV forgings have been developed over ~70 years, giving confident empirical knowledge, which in turn produces high quality components in respect to the currently used RPV materials. This, however, leads to resistance within industry to introduce new advanced materials for the same applications, and/or for technologically advanced systems such as generation 4 reactors, as empirical knowledge with respect to these materials is not available. Advanced materials may possess properties in advance of current RPV standard materials, however, a lack of empirical knowledge learned from manufacturing large RPV forgings from these materials yields uncertainty. The resistance to introduce new materials presents a limitation for the technological advancement of civil nuclear energy, as time is required to validate new materials. This yields a complimentary need to develop new advanced assessment methods that can be used to characterise the variables of RPV manufacture on microstructure evolution both rapidly and systematically and hence accelerate validation of new materials for RPV manufacture.

2.3 DILATOMETRY

2.3.1 Introduction

Dilatometry is a method in which the change in shape of a material under the application of heat can be quantified. It allows the thermal expansions of materials to be measured and material properties such as the coefficient of thermal expansion (CTE) to be determined. For materials that undergo phase transformations during heating and cooling, dilatometry allows characterisation, and this makes dilatometry an important tool in industry for the testing and evaluation of heat treatments, and for the development of new materials.

In dilatometry, the linear expansion of standard specimens is measured as a function of temperature and is plotted to form a dilatation curve. Figure 11 shows the dilatation curve for the austenitic stainless steel AISI 304L, heated and cooled at 3°C/min, with a 30 min soak at 910°C. In the chart, the dilatation has been normalised by dividing by the gauge length (Lo) to yield a thermal strain (dL/Lo). The gradient of the plot is the CTE of the material.

The variables of dilatometry are the change in temperature and the change in length of the specimen, measured from initial conditions. Both of these variables must be measured in high resolution for accurate data to be recorded. This is especially true as temperatures become very low as can be found in cryogenic applications, and when material expansion are very low, as are measured for ceramic and composite materials. These challenges have led to technological advancements in the field of dilatometry, and have yielded a large variety of dilatometers from which to choose [57,58].
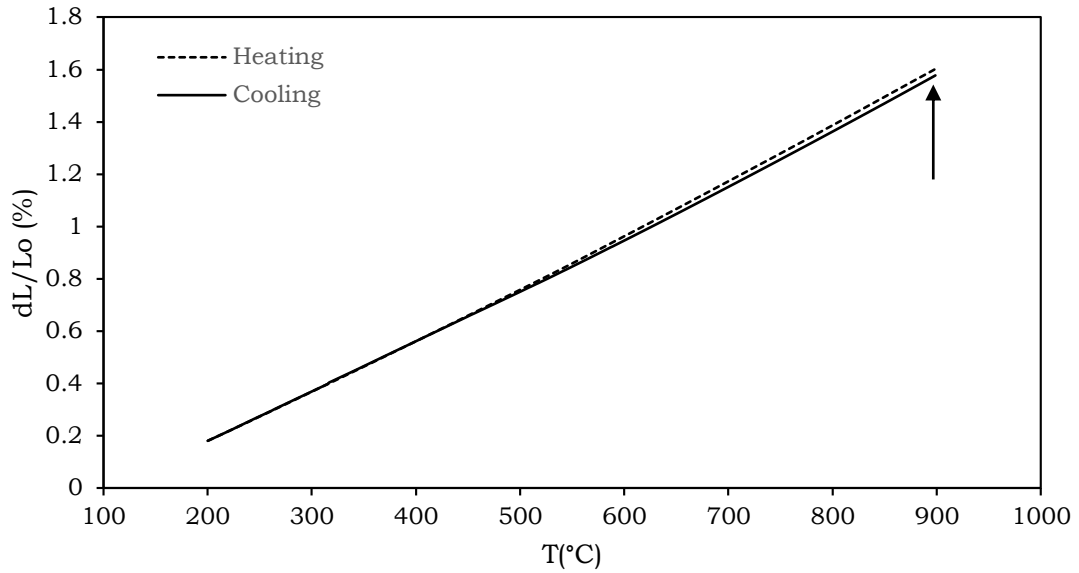
Figure 11: Dilatation of AISI 304L heated and cooled at 3°C/min

Modern dilatometers are highly sophisticated instruments, and can measure the dilatations of materials under application of heat in high resolution; dilatations can be measured in the order of nm [59] while temperature can be measured to resolutions of ±0.1°C [60]. Standardised specimens are small, with the largest ASTM specified specimens having 6mm diameters and 25mm gauge lengths. Despite the small scale of specimens, the control of temperature is often not as accurate as its measurement, and the measurement of these variables is subject to systematic error. This can be seen in Figure 11 where the maximum dilatation of the specimen is larger for heating than for cooling despite the measured temperatures being identical. This is because the bulk temperature of the specimen equalises upon soaking due to thermal lag, yielded an observed iso-thermal expansion. To increase accuracy of temperature control, smaller specimens can be tested, but this comes as a trade-off with the volume of material needed for analysis.

Depending on the function of each specific dilatometer, it is necessary to calibrate the measurements of temperature and thermal expansion

58

to yield accurate and representative data. Standards exist for the most common forms of dilatometer, but work continues to improve accuracy and in respect to technological advancement. A good example is the work of Sommer et al. [60,61] who used the Curie temperature of Fe and Fe-Ni alloys to calibrate for temperature in a differential dilatometer, and followed by developing a mathematical procedure to correct the measured longitudinal expansion for the effects of temperature gradients in their specimens [62].

2.3.2 Dilatometers

Dilatometers are classified as either absolute or relative in there function [57,60]. In absolute methods, the expansion of a specimen is measured directly while in relative methods; expansions must be calibrated using a standard reference specimen. In relative methods, calibration is required to remove systematic errors. These are often referred to as differential dilatometers. There are many forms of dilatometer which have been developed [57,58,63], many of them to analyse specific materials and the behaviours of materials in specific environments, however, over broad ranges of temperature and CTE only two types of dilatometer are used commonly. The first is the push rod dilatometer and the second is the interferometer. Standards which govern the operation and use of these types of dilatometers have been published by the ASTM E289-04 and E228-95 [64,65], and in these standards the limits by which reliable data can be recorded are given.

2.3.2.1 Push rod dilatometers

The push rod dilatometer is a mechanical device in which the thermal expansions of specimens displace a push rod. The push rod is in longitudinal contact with the specimen at one end, and is connected to a transducer at the other. The dilatation of the specimen is transmitted to the transducer via the push rod and is converted from

the transducer signal. A schematic of a push rod dilatometer is shown in Figure 12.
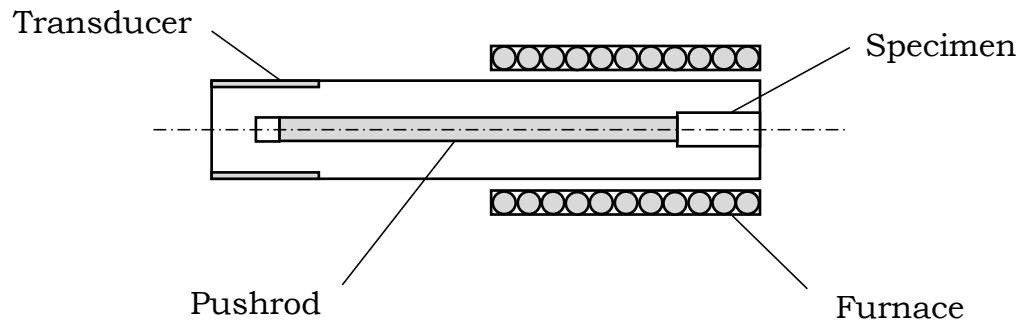

Figure 12: Schematic of a push rod dilatometer [65]

The experimental setup of push rod dilatometers requires that part of the push rod be inside the furnace that heats the specimen, and is subject to thermal expansion too. The dilatation of the push rod sums with the specimen as systematic error, and so push rod dilatometers require calibration before each experiment to remove those errors from measurements of expansion. The correct calibration procedure is outlined in ASTM E228-95 [65].

To calibrate a push rod dilatometer, a thermal program is applied to a standard reference specimen using the exact conditions and procedures intended for a test specimen. The reference specimen is made from a material for which the expansion characteristics are well known [66], and its expansion can be calculated. The calculated value is subtracted from the reference specimen to yield a quantity that represents the expansion of the push rod and other systematic errors. This quantity can be removed from the measured dilatations to give an accurate dilatation for the test specimen. The calibration however, requires that each thermal program must be completed twice, once for the reference and once for the test specimens, doubling the time

60

required to acquire accurate results. In addition, the success of the calibration is not guaranteed.

A successful calibration depends on two factors. First, the choice of reference material must be suited to the test material and the testing conditions; greatly different thermal expansion characteristics between reference and test materials will increase the level of error due to diverging dilatations with increasing temperature. Using materials with complex phase transformations for reference materials is also undesirable, as phase transformations are a function of thermal history. The initial and final microstructures and hence CTEs are unknown, and therefore the calculation of the thermal expansions of transforming materials introduces error into the calibration. The second important factor in calibrating differential dilatometers is repeatability. A calibration procedure requires the dilatometer to apply a program identically to two individual specimens. Any random errors such as external vibration, environmental factors, and operator errors during set up will lead to introduction of error in the calibration.

2.3.2.2 Interferometers

Interferometry is an optical dilatometry method in which the thermal expansion of a material is measured directly. In this method a specimen is placed between two reflecting surfaces and in the path of laser (Michelson) or monochromatic light source (Fizeau) [64]. The light beams that are reflected from the two surfaces from the specimen are summed, and the interference between them focussed through a lens to create a fringe pattern. Changes of the fringe pattern due to the dilatation of the specimen can be detected and converted to quantify the expansion. There are no mechanical components involved in interferometry, and the method is absolute in function, with the

61

resolution of measurement being fixed by the wavelength of the light source, giving resolutions in the order of nm.
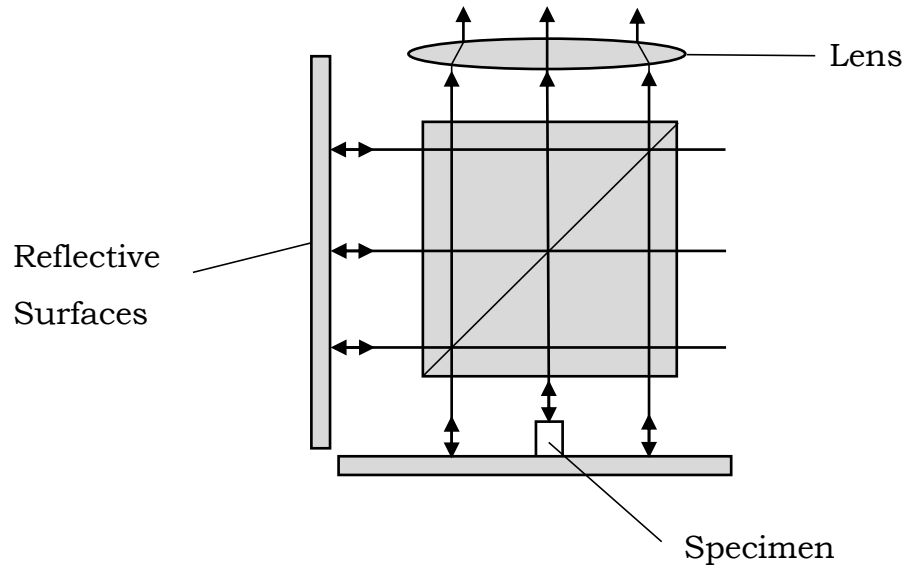

Figure 13: A schematic of an interferometer [64]

Interferometers offer improvements when compared with push rod dilatometers. For example, without mechanical transmission of expansion, no calibration is required and so both accuracy and resolution are improved [67]. This allows the analysis of materials with very low CTEs, and at extreme temperatures which would be impossible using differential dilatometers. Other benefits include a reduction in testing time and greater dexterity in both the geometry and orientation of the specimens. However, the method requires specimens to be contained within a vacuum because suspended particles in gaseous environments interfere with the transmission of light, and this means the method is limited in terms of the scale. In addition, the absence of an environment affects the heat transfer characteristics of the system, and the control of temperature is limited as a result. Therefore, there is a trade-off between the accuracy of measuring thermal expansion, and the accuracy of temperature control when using interferometers to measure thermal expansion,

especially if thermal programs are complex or contain fast heating and/or cooling rates.

2.3.3   Dilatation data

The data acquired from dilatometry is very useful for a number of practical purposes. It may be used to determine the CTE of a material, construct Thermal Equilibrium Diagrams (TEs), Time Temperature Transformation diagrams (TTTs), and CCTs. From an industrial viewpoint, CCTs are of specific importance, as they describe the non-equilibrium microstructures transformed in polymorphic materials as a function of heating and cooling rates, and relate more closely to industrial heat treatments. The CTE is a material property whose determination is essential for materials development and for design processes, as it allows the quantification of large-scale thermal expansion calculations in modern modelling software.

2.3.3.1   Analysis of dilatations

In its simplest form, dilatation of a material is approximately linear with respect to temperature, as is seen for SS304L in Figure 11. In that case, the CTE of the material is approximately constant; however, for many materials the CTE is not constant but varies with temperature. For polymorphic materials, the situation is complex with a variety of transformations and their volume fractions contributing to the recorded CTE. For example, the possible phases present in a plain carbon steel are ferrite, cementite, martensite and austenite. For mixtures of ferrite and cementite, the specific transformation may be pearlite, upper, or lower Bainite. For ferrite alone, the transformation may be diffusional or displacive with morphologies of polygonal, allotriomorphic, quasi-polygonal, granular, acicular or Widmanstätten [68,71,72].

With such a large quantity of transformations possible, it is important to understand and interpret the dilatation data accurately. Figure 14 shows the dilatation curves recorded for the low alloy steel, 20MND5, when cooling for a range of discrete iso-cooling rates. 20MND5 is a polymorphic material and Figure 14 shows that the CTE of the material changes with decreasing temperature for each cooling rate tested, evidencing that a number of transformations have occurred. The chart also shows that the transformation characteristics change as a function of cooling rate, and evidences that the material transformation kinetics also vary and are sensitive to changes of cooling rate.

Without transformation the materials dilatation has an approximate linear relationship with temperature. When a transformation occurs, this relationship becomes non-linear because the crystal structure of the transforming phase has a different specific volume to the parent phase, and often because of the latent heat released by the transformation alters heat transfer too. Once a transformation is completed, the dilatation returns to a linear relationship with temperature. With a knowledge of possible transformations in steel, the transformation sequence can be inferred from the dilatation curve; from high temperature, the first deviation is likely to be ferrite, the second bainite, and the third martensite, however, to confirm the exact transformations and their morphology, microstructure investigations and hardness testing are always required.
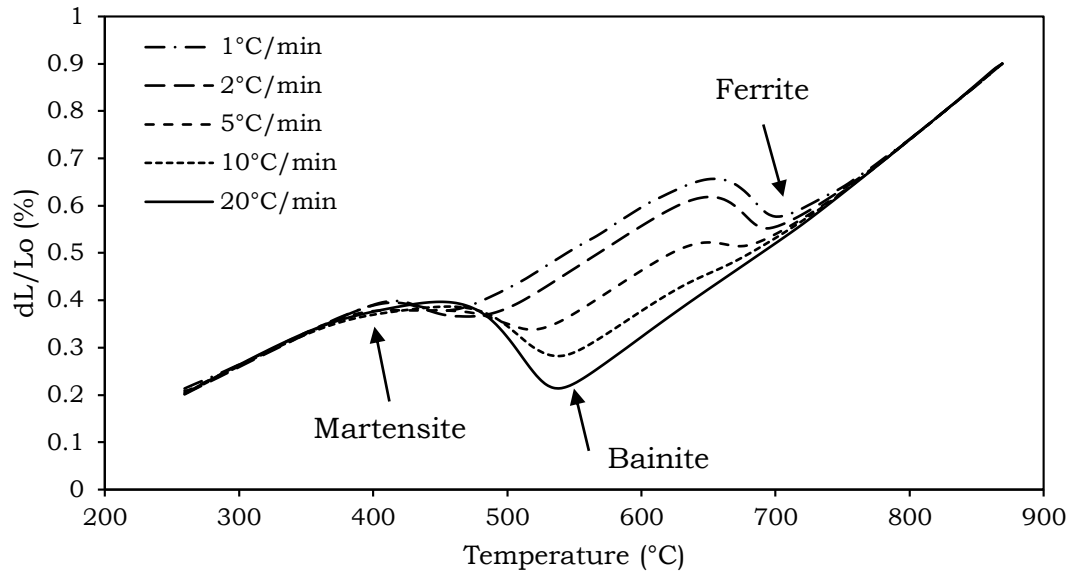
Figure 14: the dilatation curves of steel alloy 20MND5 cooling at a variety of iso-cooling rates

2.3.3.2 The coefficient of thermal expansion

The CTE is a material property that is dependent on the interatomic bonding forces of a given material. A strong atomic bond yields a low CTE while weaker bonds have larger CTEs. It follows that metals have larger CTEs than ceramics, due to the nature of their atomic bonding. It should also follow that the CTE is an anisotropic property that depends on linear density of a given crystal lattice, and highly textured materials may have different CTEs depending on crystallographic texture levels. It is therefore important to characterise the CTE of a material so that accurate component designs can be achieved. If large components such as pressure vessels are required to work at high temperature, then it can be appreciated that significant dimensional change can occur, leading to stresses that must be accounted for during the design stages.

The CTE of a material can be defined as the fractional increase in length (thermal strain) per unit rise in temperature [58,73,74]. This may be written as:

$$\alpha = \frac{\Delta L}{L_0 \cdot \Delta T} \tag{3}$$

Where α is the linear CTE, ΔL is the change in length between two points, ΔT is the change in temperature between the same two points and the L_0 is the original length of the specimen. Equation (1) plots a linear gradient between two specific measurements, which graphically, describes a mean gradient between the two points. The CTE for many materials is, however, a temperature dependent property and tends to increase with temperature [58]. To define the true CTE the gradient at a single point must be known [73]. Since the dilatometric plot is one of thermal strain against temperature the true CTE may be written:

$$\alpha_T = \frac{d}{dT}\left(\frac{\Delta L}{L_0}\right) \tag{4}$$

Hence, dimensional change can be quantified as a function of temperature directly.

2.3.3.3 *Continuous cooling transformations*

Thermal expansion exists because the vibrational amplitude of atoms becomes increased with increased energy input. Interatomic distances increase and the material expands. Some materials can reduce their energy state by rearranging their crystal structure, making the atomic structure more stable. These materials are referred to as polymorphic, and they exist in solutions of one or more phases, both in equilibrium and non-equilibrium morphologies. The phase changes that occur in polymorphic materials also result in a change of specific volume. Since dilatometers detect dimensional change in high resolution, dilatometry

is a key method of characterising material responses to heating and cooling. From an industrial standpoint, an important characterisation is microstructure evolution under continuous cooling conditions [75]. These conditions more closely relate to industrial processes when compared to isothermal conditions, and aid in the design of thermal processes.

If a transforming material is heated and cooled at a specific rate, the temperatures at which transformations occur, as a function of that rate can be determined from the dilatation data. These are known as critical temperatures. If the critical temperatures of the material are determined as a function of many different cooling rates, they can then be plotted as a locus of data points in a plot of temperature against time. An example is given in Figure 15:
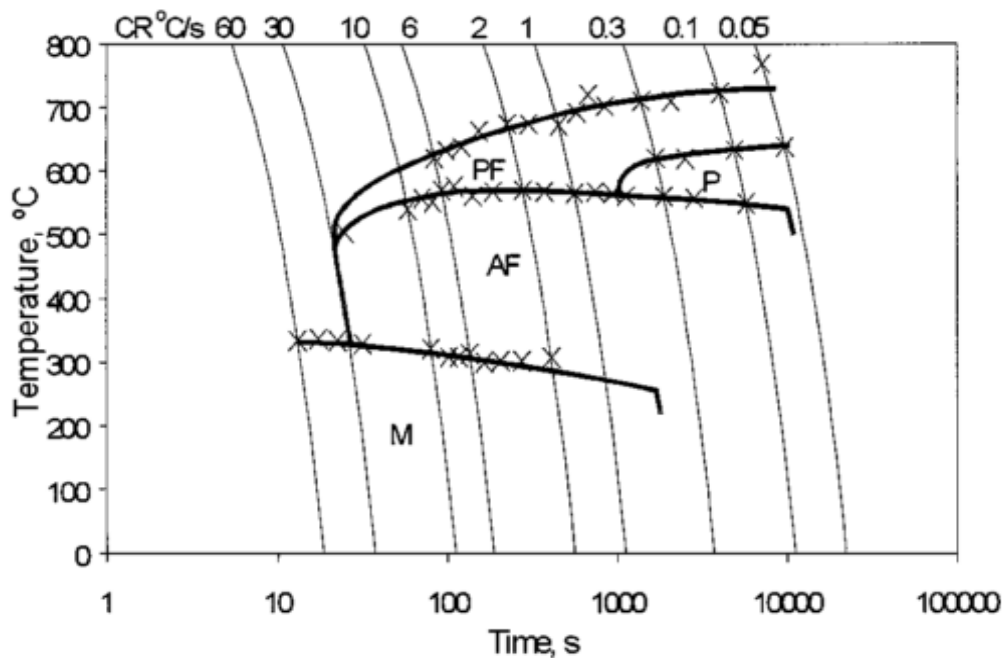

Figure 15: A Continuous Cooling Transformation Diagram for a medium carbon steel [76]

The loci of critical temperatures separates the CCT diagram into a number of equilibrium and non-equilibrium phase fields with the identity of the fields being determined from metallographic investigation and hardness testing [77]. Once the phase fields are identified, the CCT indicates the response of a material for known cooling rates. For example, in Figure 15, the CCT indicates reduced volume fractions of the diffusional transformations of Polygonal Ferrite (PF) and Pearlite (P) as cooling rate increases. The quantity of Acicular Ferrite (AF) also reduces and Martensite (M) increases until a rate of 30°C/s at which 100% martensite is transformed.

CCT diagrams are considered useful for industry and many researches have been completed toward their development. Atkins et al. [78] developed and compiled a large number of continuous cooling diagrams for British Steel ltd. Their work entitled 'An Atlas of Continuous Cooling Diagrams for Engineering Steels' showed the behaviours of many industrially meaningful materials in response to continuous cooling, and was published as an industrial tool for the design of thermal processes, however, the work was flawed in a number of ways. At that time, high-resolution dilatometry was not available and their experimental method was based upon a quenching method. Specimens where quenched in air, water and oil and their response to the quench was recorded using thermocouples. Cooling rates at intermediate locations were inferred from a calibrated table and microstructures were inferred from the CCT respectively.

This approach does not represent continuous cooling conditions due to the physical limitations of quenching processes. Temperature gradients are generated within each specimen during quenching and these will vary with time, varying the cooling rate both with thickness and time too. Therefore, the approach assumed that transformations occurred independently from cooling rate, and the rate at each critical

temperature was the only criterion for prediction of microstructure. This simplification does not represent transformation kinetics, as the thermal history is a dependent variable. Another observation is the omission of data points from each of Atkins et al.'s diagrams. The absence of data points on each CCT implies that a level of smoothing was applied to each data set. Normally an error calculation provides certainty in the smoothing procedures; however, no error calculations were presented in the atlas.

During the time of Atkins et al., others also published smaller atlases of CCT diagrams obtained by similar experimental methods. Eventually, these atlases were compiled with other independent CCT diagrams by Vander Voort [79], and were published; however, these diagrams contain the errors of the past.

The technological development of dilatometry practices has increased the accuracy by which CCT diagrams can be generated. Since the publication of Vander Voort's Atlas many CCT diagrams have been developed and published, however, no effort to update the databases created by Akins and Vander Voort has been made. Almost all work has been completed towards specific materials development, and therefore the relevance of Atkins and Vander Voort's Atlas' is limited to modern industry, as is the specificity of new scientific researches.

The experimental determination of CCT diagrams is flawed in many ways. The systematic error present in dilatometry has already been discussed in terms of measurement and control. Issues due to temperature gradients in the specimen that can also cause inaccuracies, as was highlighted in Figure 11. Random error has been discussed to affect repeatability, and all these contribute to uncertainty. It is possible to reduce the uncertainty in measurement

69

by collating large quantities of data; however, it must be appreciated that a large number of experimental repetitions for each cooling rate increases the time and cost required to form acceptable conclusions. Since a large number of cooling rates are required for a detailed CCT, the total time needed becomes significant, especially in the pursuit of reducing experimental error. To update the database developed by Atkins et al. and Vander Voort et al. would therefore be a long and laborious task, which even with the application of modern dilatometry would contain a degree of uncertainty.

It is also arguable that such an update is not relevant for industry. This is because a CCT is not a unique diagram for a given material, but highly specific, and depends on the composition and initial microstructure of the specimens tested. New phases are likely to nucleate and grow from grain boundaries, and so the scale of the initial microstructure can modify the transformation characteristics as was shown by Pous-Romero et al. [30] and it follows that the thermo-mechanical history of specific specimens adds to uncertainty. For industry, a single CCT cannot be used to characterise the behaviour of components undergoing heat treatment, which is underpinned when considering the variation of composition, microstructure and temperature that exists through the thickness of a large components such as an RPV's, as was discussed in section 2.2. To add to this limitation, current dilatometers are small in scale and only allow investigations of microstructure and hardness from tested specimens. For safety critical components, mechanical property testing is also needed to ensure that property specifications are met, and this cannot be achieved using current dilatometry technologies.

2.3.4 Summary

Dilatometry is a useful method of characterising the effect of heat treatments on materials, however, current dilatometry technology and its application is limited to industry. This is because variability of results in terms of material and experiment, and dissimilarities between industrial processes and experiment limit the use of historical data. Current technologies are small in scale and do not allow complete material characterisations, and both these factors mean that full scale industrial trials remain necessary to ensure property specifications are met. For developing new materials and new heat treatments, dilatometry is a key method of analysis, but the limitations associated with the current technology require that further development is necessary. Specifically, a dilatometer with increased scale would allow mechanical testing and hence full characterisations, and if volumes of material that represent any applied thermal history were produced, rapid systematic studies that relate specifically to industrial processes could be completed, facilitating the development of new materials and/or new heat treatments.

3   THE HEAT TREATMENT SIMULATOR

3.1   INTRODUCTION

Current dilatometers are small in scale and do not allow mechanical property evaluation from ASTM standard specimens. For industry, this means that heat treatments cannot be fully characterised, and therefore destructive testing of full-scale component test coupons is necessary to validate heat treatments. This method of validation is inefficient due to the iterative nature of development, and is empirical, leading to resistance within industry to introduce new materials, as they cannot be characterised quickly.

The Heat Treatment Simulator (HTS) can be considered as a large-scale dilatometer in which complex heating and cooling profiles are applied to large metallic specimens. The unique feature of the HTS is that its scale permits the characterisation of both microstructure and mechanical properties of individual test specimens, which addresses the limitations of current dilatometer technologies. The HTS was designed and manufactured by Inductelec Ltd, Sheffield, UK, under instruction and specification given by The University of Sheffield and Sheffield Forgemasters International Limited (SFIL). The HTS is installed at SFIL, and operates under their provision. The work

presented in this chapter details the initial investigations of the HTS function following installation, and the optimization of its performance.

3.1.1 The HTS

The HTS consists of a 30kW induction coil that heats and cools cylindrical metallic specimens of 42mm diameter and 135mm gauge length, in accordance to pre-written PLC programming. The specimens are mounted vertically within the induction coil between a non-conductive fixed pin, and free moving mono-directional push rod. During an applied thermal program, dilatations are transferred from the specimen through the push rod and are measured by an interferometer. Figure 16.
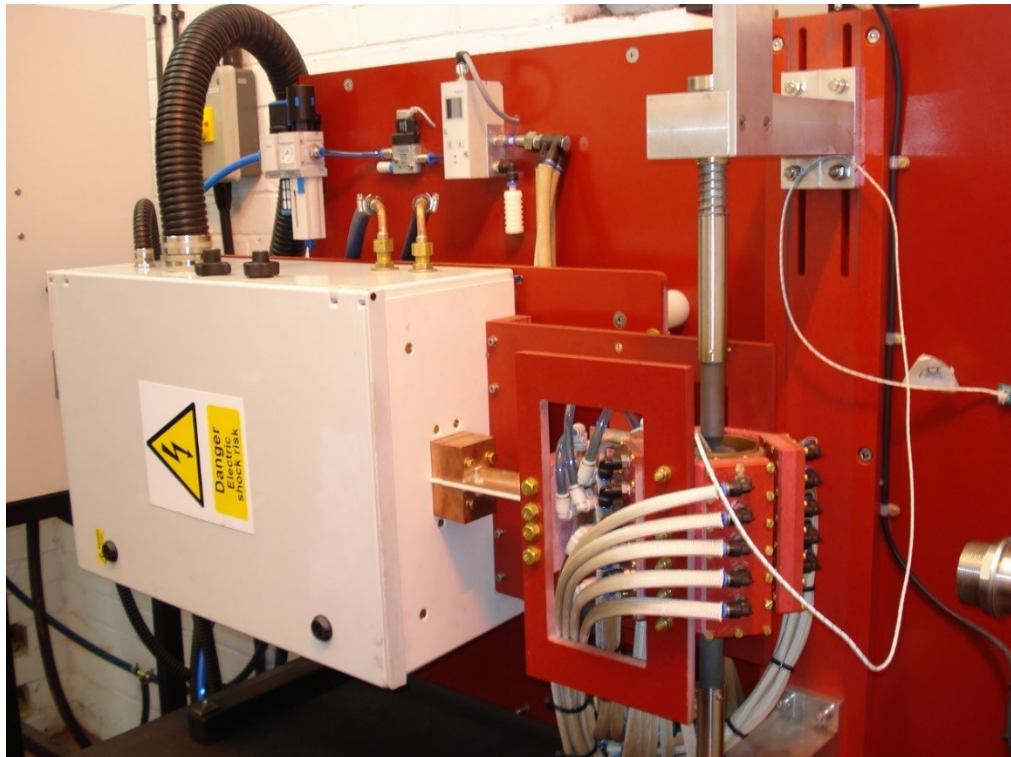

Figure 16: An image of the HTS. Labelling is omitted due to industrial sensitivity

Tracking the specimen temperature to applied thermal programs is achieved with a PID feedback control system. This is facilitated by a K-Type thermocouple spot-welded to the surface of each specimen, halfway along the gauge length. In operation, the HTS tracks complex thermal profiles between defined temperature set points, in accordance to user defined heating/cooling rates. Between each defined set point, the system generates subsidiary set points in respect to the user specified heating or cooling rate. Temperature tracking is achieved by a stepped power input, which is toggled on/off when the specimen temperature is above or below set points by a user defined temperature threshold. This fixes the accuracy of temperature tracking with respect to the control thermocouple at the surface. The system automatically de-rates the power supplied to approximate the demands of the heating/cooling rate for each temperature set point, and the frequency of the coil can be varied between 60-100 kHz to allow modification of the system parameters. The ability of the HTS to track temperature accurately is assisted by a forced convection cooling system. In operation, this system uses compressed air to achieve rapid cooling rates, which with simultaneous application of power from the induction coil, facilitates more accurate tracking of temperature.

As an induction heating assembly, the HTS can heat specimens with a greater level of homogeneity of temperature when compared with the surface heat transfer associated with furnace processing, especially at greater rates of heating and cooling. The forced air quenching system is designed to complement accuracy during cooling, and maintain homogeneity at faster cooling rates leading to a system that should meet the needs of the HTS specification. However, the transfer of heat by induction is not homogenous, and as a function of specific parameters can become more complex. In addition, the increased size of the HTS specimens may result in temperature lag due to conduction through the larger thickness, despite the forced air quenching.

3.1.2 Induction heating

For induction heating of cylindrical specimens, it is known that the idealised distribution of current induced in a specimen takes the form of an exponential with depth from the surface toward cylinder axis [80].
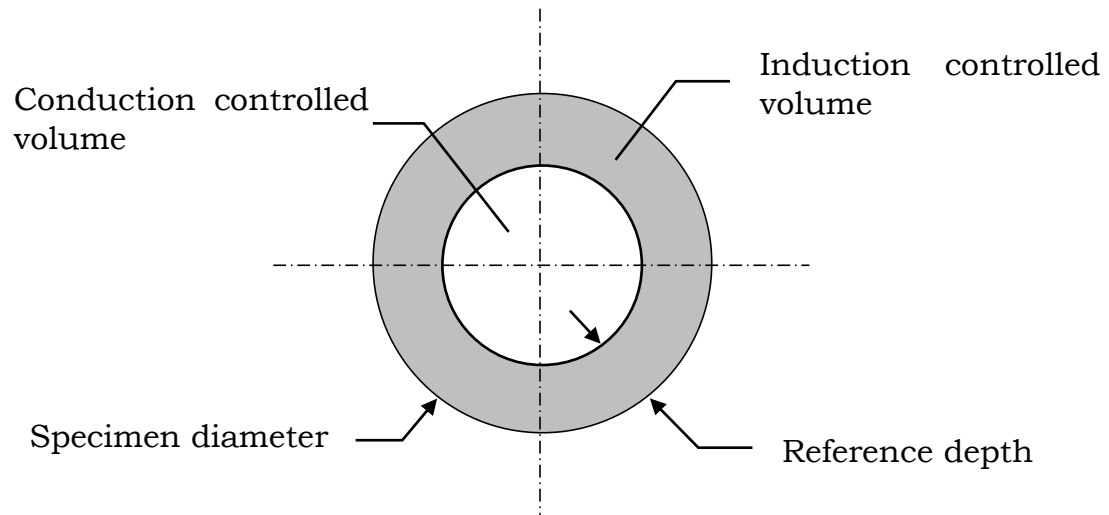

Figure 17: Power distribution for idealised induction heating of a cylindrical specimen

The depth at which the current density is 1/3 of the density of the surface is defined as the reference depth. The reference depth is often applied as a design tool for induction heating systems. The heating power of the system due to the induced current occurs by the Joule effect [81]:

$$P = I^2 R \tag{5}$$

Where R is the electrical resistance of the specimen and I is the current density. R is defined by:

$$R = \frac{\rho L}{a} \tag{6}$$

Where ρ is the electrical resistivity of the material, L is the specimen length and a is the specimen's cross sectional area. As discussed above, ideally for cylindrical specimens, I decays exponentially with radial depth and is defined by:

$$I = I_0 e^{-\frac{y}{\delta}} \tag{7}$$

Where I_0 is the applied current, y is the depth from the surface and δ is the reference depth. Substituting equation 5 with equations 6 & 7:

$$P = \left(\frac{I_0}{e^{\frac{y}{\delta}}} \right)^2 \cdot \frac{\rho L}{a}$$

$$P = \left(\frac{I_0^2 \rho L}{a} \right) \cdot e^{-\frac{2y}{\delta}} \tag{8}$$

Therefore, the heating power is scaled by the term $e^{-\frac{2y}{\delta}}$ and is distributed by the ratio of y/δ. Evaluating the ratio y/δ (table 2) it is found that at the surface of the specimen a heating power of 100% is provided. However, when the penetration depth is equal to the reference depth, the heating power is reduced to ~13.5%. This implies that a volume of material within the core of the specimen relies on the conduction of heat through the solid to homogenise temperature.

Table 2: Scaling of heating power through thickness of induction heating a cylindrical specimen

y/δ	$exp(-2y/\delta)$
0	1.0000
1	0.1353
2	0.0183
3	0.0025

The value of the reference depth is essential when designing efficient induction heating apparatus, as its value defines the scale of the conduction-controlled volume. This is approximated in meters by the equation:

$$\delta \approx 503 \sqrt{\frac{\rho}{\mu_r \cdot f}} \tag{9}$$

Where ρ is the materials electrical resistivity, μ is the relative permittivity and f is the frequency of the coil in kHz. For many steels, the relative permittivity is approximated as unity, and therefore the reference depth can be approximated for coil frequency as a function of electrical resistivity. Electrical resistivity however, is a function of temperature, and so to maintain a constant reference depth, for varying electrical resistivity, the frequency must vary. The HTS can vary the frequency applied between 60-100 kHz. The effect of this variable frequency on the reference depth, as a function of temperature is plotted for the austenitic stainless steel AISI 304L in Figure 18:
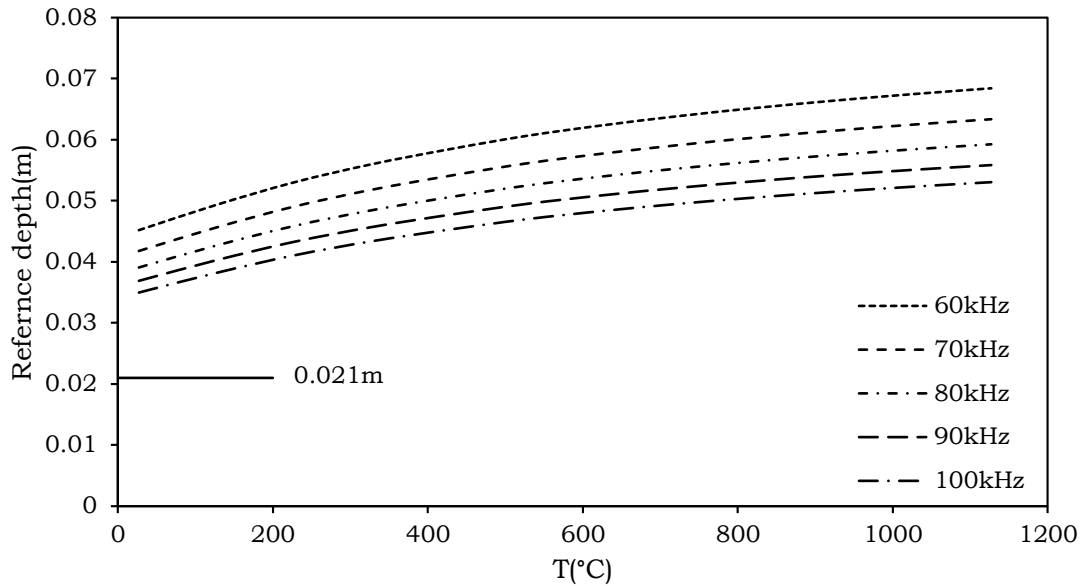
Figure 18: The variability of reference depth for AISI 304L as a function of temperature, for the applied frequency range of the HTS.

For through heating of material, a frequency close to the reference depth of the material should be chosen, however, Figure 18 shows that for 304L, the reference depth varies by more than twice the radius of a HTS specimen within the defined frequency range. The specific frequency applied by the HTS is varied during each test with respect to power demand, and this makes the through thickness temperature evolution of specimens during testing uncertain.

The specific variables that determine the characteristics of thermal evolution for induction heating are the reference depth, the rate of energy transfer, and the thermal properties of the material, specifically the conductive properties. This last point is important as the conductive properties are related to electrical properties relied upon for induction. As temperatures are increased, thermal conductivity and electrical resistivity are both increased, and while increased conductivity may be beneficial for homogenising the specimen temperature through thickness, the increased resistivity reduces heating power at higher temperatures.

78

For idealised operation of induction heating equipment, the frequencies required for known reference depths can be determined, however as the thermal resistivity of metallic materials changes with temperature, this also changes the frequency required for efficient heating. Conductive properties also vary with temperature and these must be relied upon to distribute heat through the thickness of each specimen. The function of the HTS is to simulate complex thermal programs on metallic specimens and generate volumes of material that represent the applied program. For mechanical tests to be representative, the specimen must have temperature homogeneity through its thickness. A theoretical investigation has shown that many factors affect the thermal evolution of specimens tested by induction, and so the level of temperature homogeneity within HTS specimens during testing is unknown.

3.1.3 Aims and objectives

At the time of commissioning, the temperature homogeneity of HTS specimens was investigated using finite element (FE) models, which were experimentally validated by control thermocouple readings taken at the surface, and from pyrometer imaging of specimen's surface for a range of idealised heat treatments. These results indicated good temperature tracking at the surface, but did not evidence temperature homogeneity through thickness. To verify the function of the HTS it is necessary to know how the temperature distribution in each specimen evolves so that volumes of material that are representative can be produced. The aim of the work presented in this chapter is to investigate the temperature distribution of specimens tested in the HTS, and to optimize the performance of the HTS in respect, so that a representative volume of material can be reproducibly produced in each specimen tested.

3.2   EXPERIMENTAL

To investigate the thermal evolution of HTS specimens during testing, a temperature measurement (TM) specimen was developed. The TM specimen had geometry of a standard HTS specimen: A solid cylinder with dimensions of 42mm diameter and 135mm gauge length. However, the temperature measurement specimen was also prepared with nine (9) additional K-Type thermocouples, embedded at three radial depths, and three different longitudinal locations that allowed the identification of both radial and longitudinal temperature inhomogeneity during testing. The location of these thermocouples are shown in the working drawing for the TM specimens. Figure 19. The positions of the thermocouples were given numerical denotations as detailed in Figure 19, and organised in Table 3.

Table 3: Numerical labelling for Thermocouple locations

	Depth from Surface (mm)		
Height (mm)	5.25	10.5	21
117.5	1-1	1-2	1-3
67.5	2-1	2-2	2-3
17.5	3-1	3-2	2-2

The experimental program applied consisted of: 1. heating the temperature measurement specimen to 910°C at a rate of 20°C/min, 2. holding for 30 minutes at 910°C and 3. continuous cooling to room temperature at 20°C/min. During testing the temperature profile at each thermocouple position was recorded using National Instruments LabVIEW, which sampled temperature at 1/s. This allowed the thermal evolution of the TM specimen to be analysed in high resolution with respect to the experimental parameters.

A single TM specimen was made from the austenitic stainless steel AISI 304L. This material was chosen as it does not exhibit any transformations of microstructure within the experimental temperature range, and so the discontinuous effects of transformations on the specimen's thermal expansion during testing could be avoided, ensuring clarity in the analysis of test results.

Before experimentation began, the composition of the TM specimen was measured by spark optical emission spectrometry (OES) and compared with the compositional limits specified for 304L by the ASTM. The ASTM specification of AISI 304L, and composition as tested by spark OES are shown in Table 4.

Table 4: ASTM composition for AISI 304L (wt. %)

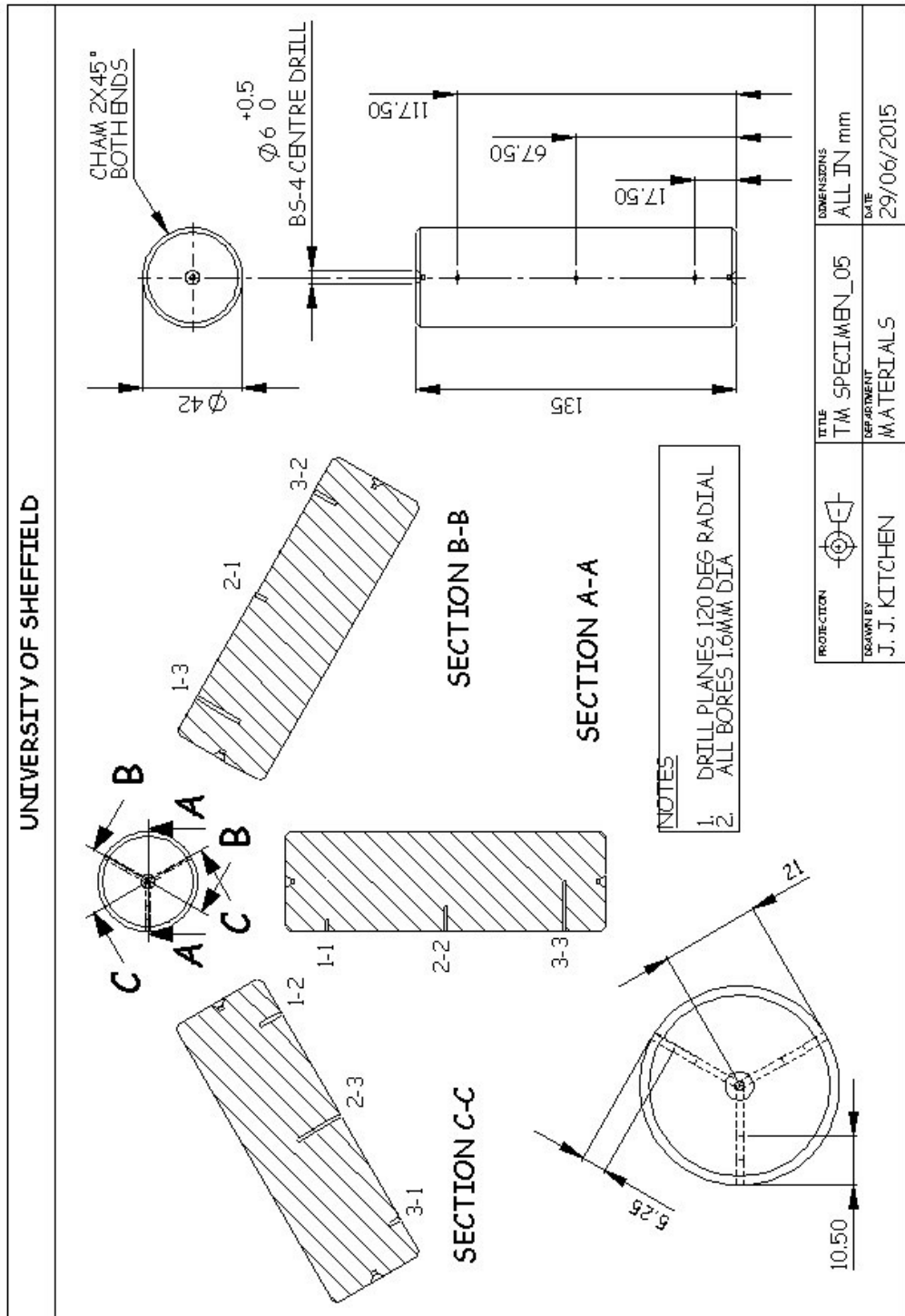|	C	Mn	P	S	Si	Cr	Ni	Fe
ASTM	<0.03	<2.00	<0.45	<0.03	<1.00	18.00-20.00	8.00-12.00	Bal.
OES	0.029	1.37	0.029	0.021	0.35	18.46	8.37	Bal.

Figure 19: The working drawing of the TM specimen. The positioning of the surface bores was chosen to reveal both radial and longitudinal temperature gradients.

With the composition of the TM specimen material within the ASTM specified limits, the thermal expansion behaviour of the material was characterised. This allowed the dilatation of the material to be calculated and compared with the thermal expansions recorded by the HTS for each test. Thermal expansion data was acquired from literature [73,74,82], and by experiment. These sources were combined to form a characteristic equation for 304L from which dilatation could be calculated. For the experimental characterisation, a single 304L specimen measuring 6mm diameter and 25mm gauge length was prepared and tested in a Netzsch 402C differential dilatometer. This experiment heated the specimen at 3°C/min to 1000°C, soaked for 30 minutes, then cooled at 3°C/min that conformed to ASTM standards for CTE determination. This procedure was completed twice for the specimen that provided four experimental data sets to be combined with literature. The combined data was fitted with a second order polynomial equation that allowed thermal expansion to be calculated. Figure 20:

$$\frac{dL}{Lo} = 2.88 \cdot 10^{-7} T^2 + 1.71 \cdot 10^{-3} T - 4.34 \cdot 10^{-2}$$
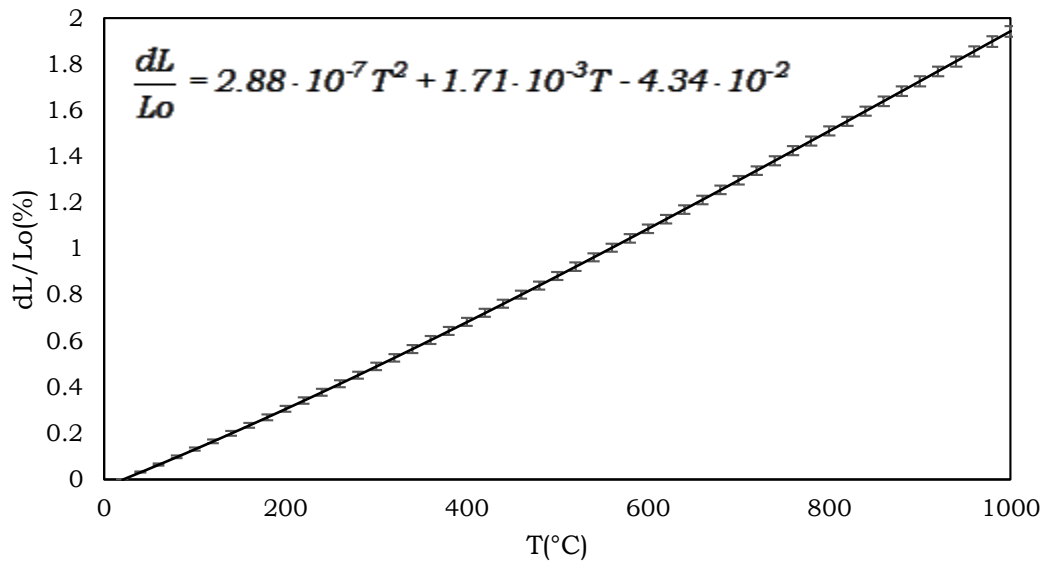
Figure 20: The thermal expansion of The TM material as characterised by literature and experiment. Error bars indicate 95% confidence limits

The TM experimental procedure was repeated 13 times. After each repetition, an analysis of the temperature evolution and thermal expansion was completed, and an attempt to improve performance of the HTS was made. The TM specimen was then tested to ascertain the effect of the improvements, and through iteration, the performance of the HTS was optimised.

3.3   RESULTS

Optimisation of the HTS was completed by iteration, and 13 experimental trials were completed in this respect. The number of iterations completed cannot be presented here; what is presented in this section are the results of the initial and final tests.

3.3.1   Initial investigation

In Figure 21 the results of the initial testing in terms of temperature evolution and thermal expansion are presented. Figure 21a) displays thermal evolution of the control thermocouple, the target temperature profile and the greatest thermal deviators to the target. The figure shows that the specimen control thermocouple tracks the target temperature well through the majority of the program but loses control during cooling from temperatures of ~450°C and lower. This is because at lower temperatures the dissipation of heat from the surface is retarded due to a reduced contribution from radiative heat losses. Conduction of heat to the surface is also retarded due to the reducing driving force, and so the specimen cannot match the target-cooling rate for the experiment when cooling though relatively low temperatures.

Also upon soaking, it is observed that the thermal deviators plotted do not track the target temperatures very closely. The locations of the

profiles recorded were location 2-3 at the longitudinal/radial centre, and location 3-1 near the surface at the bottom of the specimen. It is visible by comparing the extremes that a temperature difference in the order of 100°C exists within the specimen, and that this increases as a function of temperature to reach a maximum upon soaking.

In Figure 21b), the recorded thermal expansions of the TM specimen as a function of the control temperatures recorded for the test are plotted. The calculated expansion of 304L from the characteristic equation is also plotted for these temperatures. For this plot, all expansions are aligned to a datum at 200°C to allow clear comparison. The chart shows that the specimen's thermal expansion is notably greater than the calculated value during heating, and increases with increased temperature to reach a maximum at the beginning of the soaking period. The thermal expansion then reduces isothermally during soaking. Since thermal expansion is a function of temperature, this indicates that while the control thermocouple is recording temperatures that track the target well, the average temperature of the specimen is greater than the target upon the start of the soaking period, and this implies that the TM specimen has become internally overheated.

This can be explained by considering the operation of the HTS. During heating the distribution of heating power through the specimen can be considered idealised, taking the form of an exponential with radius as discussed in section 3.1.2. However, the power input is stepped in/out by the control thermocouple attached to the surface. The TM specimen is mounted in open air. Heat is dissipated from its surface quickly, primarily through convection, but significantly by radiation at high temperatures. Internally however, heat must be transferred to the surface for dissipation. The rate of transfer is controlled by the material's conductive properties which are a function of temperature,

85

but which are always retarded for metallic materials in comparison to convection and radiation [83]. The control thermocouple is mounted to the surface of the specimen, and power is applied when the surface temperature drops below that of the target, but internally, the heat is not dissipated, and therefore increases each time the power is stepped in. The result is that the measured dilatation becomes greater than that of the calculated data during heating when plotted against the control temperatures. During soaking, less power is required to maintain constant temperature, and this gives the time needed for conduction to the surface, reducing the need for further power. The result is that the specimen temperature begins to homogenise, and so the thermal expansion reduces.

The results in Figure 21 and discussions above show that a good temperature homogeneity can be achieved by soaking, however, the internal overheat occurring during heating is a concern: If a transforming material is overheated before cooling the prior microstructure could be altered irreversibly, affecting transformation kinetics during cooling. What is required of the HTS is that it produces large volumes of material that are representative of the programed thermal profile, and so the magnitude and distribution of overheating must be investigated.

To quantify internal overheating, the temperature distribution in the specimen was evaluated. The maximum difference between each thermocouple and the target temperature was plotted against the position of each thermocouple, both longitudinally and radially. As previously discussed, the greatest overheating occurred at the start of the soaking period and so the temperatures at this point were chosen for evaluation. In Figure 22 the temperature distribution at the onset of soaking for the initial trials is shown. These are plotted together with the allowable tolerances of temperature as specified by SFIL, which are

fixed at ±10°C on each temperature set point. In Figure 22a) the longitudinal temperature inhomogeneity for the three radial locations are plotted. The plot shows that the specimen experiences large temperature variation with a low temperature error of approximately -54°C on the target, and a high temperature error of approximately +17°C on the target. It is also evident that the central section of the specimen is greater in temperature than each ends of the specimen. This is better shown in Figure 22b) that shows that all the thermocouples at the bottom of the specimen are below the target tolerance. At the centre, the temperatures are greater than tolerance except for near the surface location, while at the top only the core thermocouples are within the tolerance limits, with the near surface temperatures being lower.

What is required of the HTS is that it produces a volume of material that is representative of the programed thermal profile. The initial investigation shows that this volume does not exist in the specimen; in the core, the material has overheated beyond the tolerances specified by SFIL, while near the surface, especially at the ends, the temperature is below the target tolerance. In this state of operation, the initial results show that the HTS cannot produce representative volumes of material; however, the results also show that the distribution of heat is predictable, with temperature reducing from the core towards the surfaces. This is systematic and therefore temperature homogeneity can be controlled.
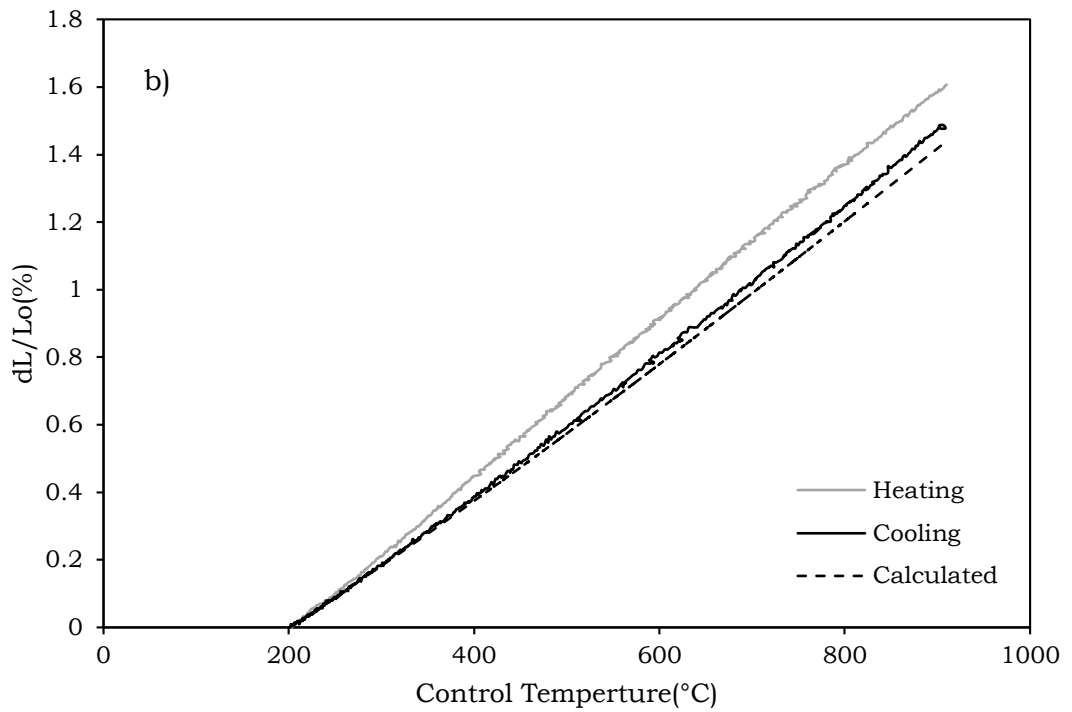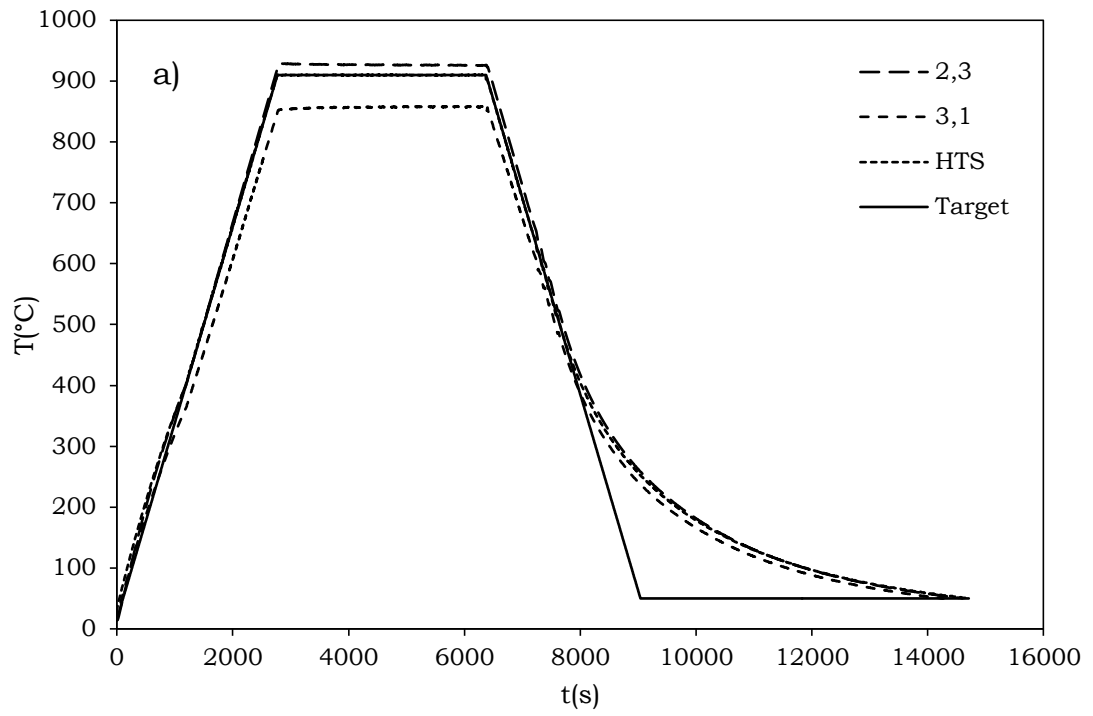
Figure 21: The results of trial experiments under continuous cooling conditions show
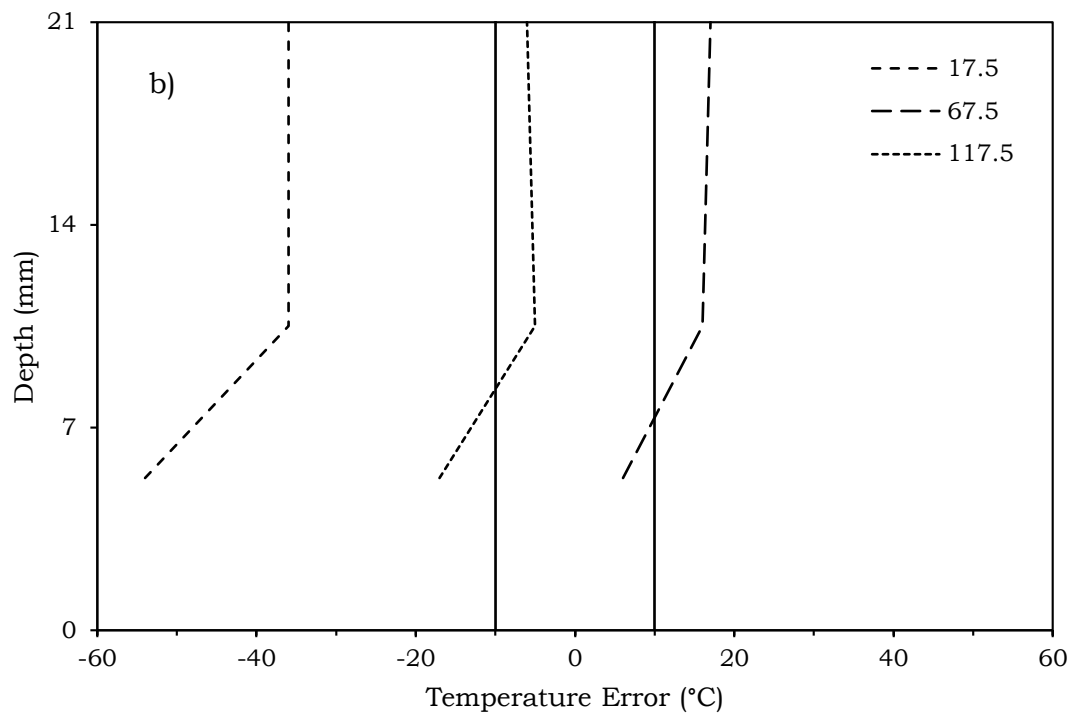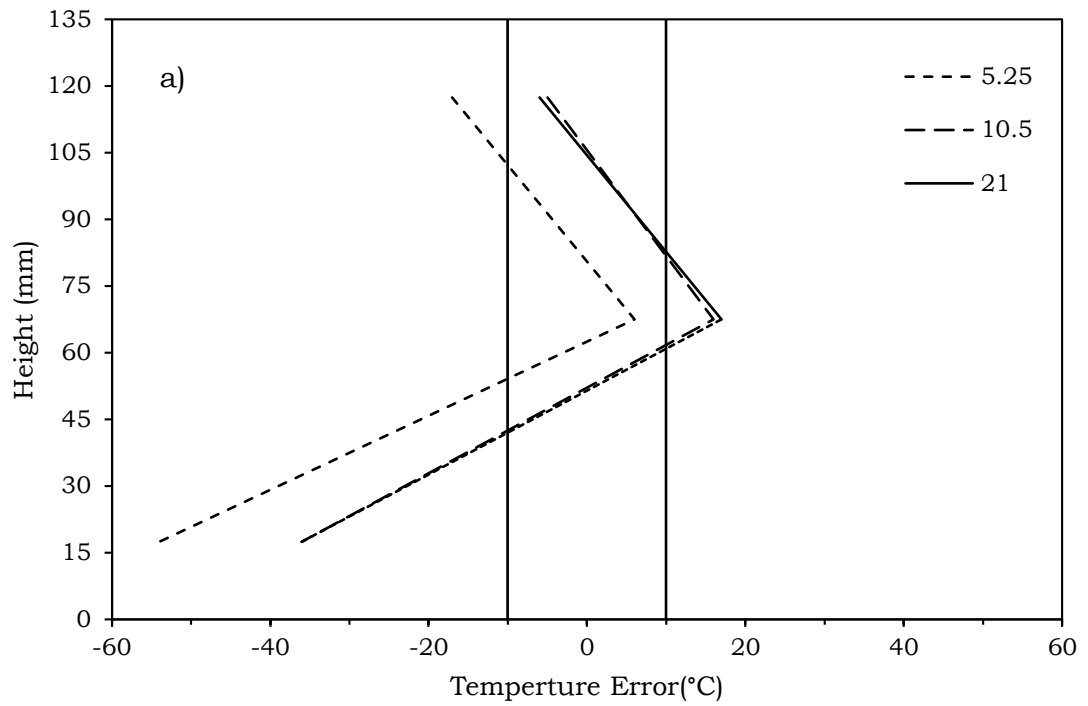large temperature inhomogeneity of the specimen

Figure 22: The maximum temperature error during the initial trial as a function of position, a) plotted longitudinally, b) plotted radially.

3.3.2 Optimization and adjustment

For a volume of each specimen to be representative of the applied thermal profile, it must exist within the core of the specimen without overheating. It is also necessary that this volume be maximised to ensure mechanical testing of the material is representative too. The results of the initial investigation showed that the ends of the specimen were a maximum of 71°C lower in temperature that the centre and this evidenced that heat loss due to end effects was a significant contributor to temperature inhomogeneity. It follows that the representative volume can be maximised by controlling this heat loss, and thus a method of control was investigated.

The method of control investigated was to insulate the ends of the specimen using an industrial refractory. The insulation was applied in different thickness and the application tested using the TM program to ascertain the effect on temperature distribution. This was quantified by the range of temperatures recorded and the symmetry of the temperature distribution both longitudinally and radially.

Following temperature optimization, the volume of material was adjusted by temperature to ensure that no overheating of the core volume occurred. This was made possible by identifying the magnitude of systematic overheat in the specimen, and manual removal of this quantity from the temperature set points within the TM program. The results of both optimization and adjustment are shown in Figure 23 and Figure 24.

In Figure 23 the temperature profile of the specimen following optimization and adjustment, and the thermal expansion (dL/Lo) as a percentage of the original length is plotted. In Figure 23a) the profile

shows that the HTS continues to lose control of the specimen temperature below ~450°C when cooling, however, the difference between the largest thermal deviators is reduced to +11°C and -24°C on the target temperature. Overheating of the specimen has been largely removed and is evidenced in the thermal expansion plot, Figure 23b). This shows that the difference in expansion at the start and end of soaking has been greatly reduced, and implies greater accuracy and homogeneity of temperature when compared to the initial investigation. The remaining isothermal expansion has become a positive expansion, also indicating that internal overheating has been greatly reduced. However, it is noted that both these thermal expansions remain notably greater than the calculated value.

In Figure 24 the longitudinal and radial temperature error plots provide further evidence of these deductions. The results show significant improvement of temperature homogeneity when compared to the initial tests, which is evidenced by both the difference between the highest and lowest temperatures and the symmetry of the temperature distribution. In Figure 24a), the longitudinal error shows that the core of the specimen is within the tolerance of temperature, and only the near surface thermocouples are below the set point temperature limit. Figure 24b) also shows a core region of representative temperature, but also gives the radial depths at which the temperature exceeds the tolerance limits, hence, the size of the volume can be quantified.
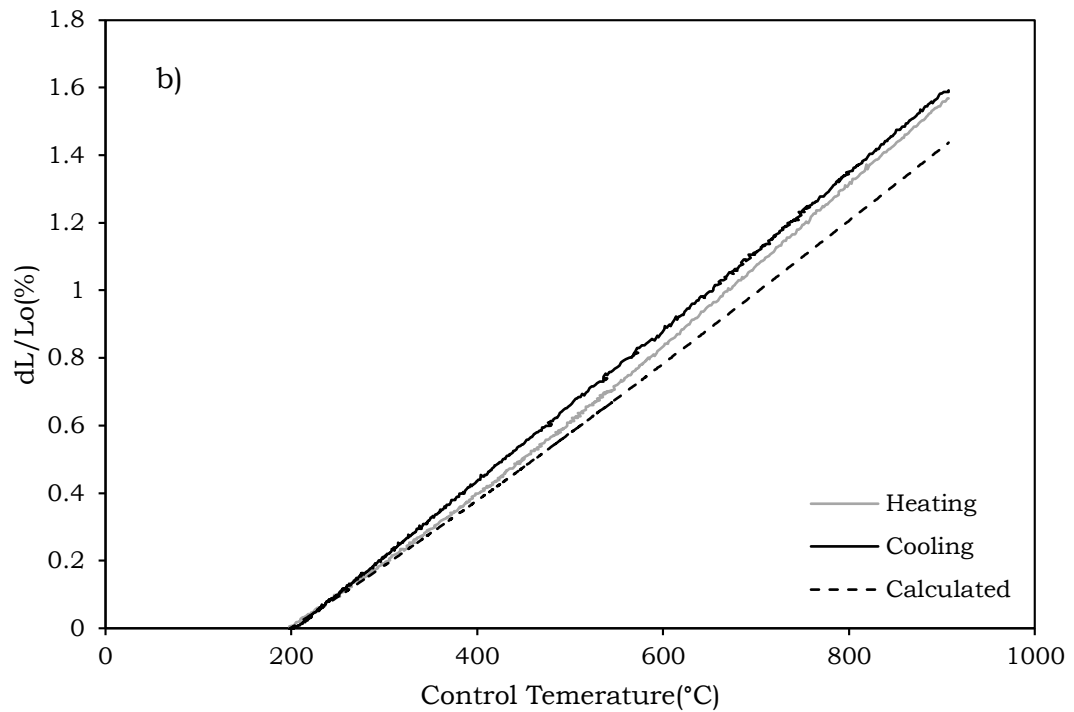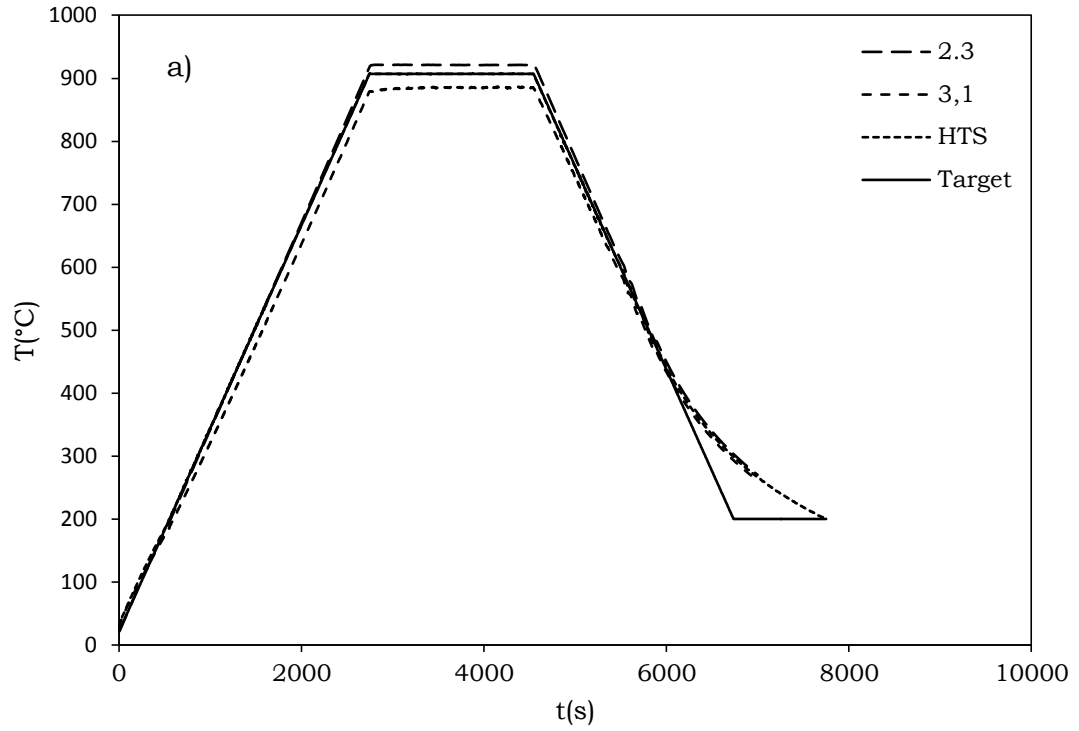
Figure 23: The results of experiments following optimization and adjustment, a) shows
the maximum temperature difference in the specimen has been reduced, b) The thermal
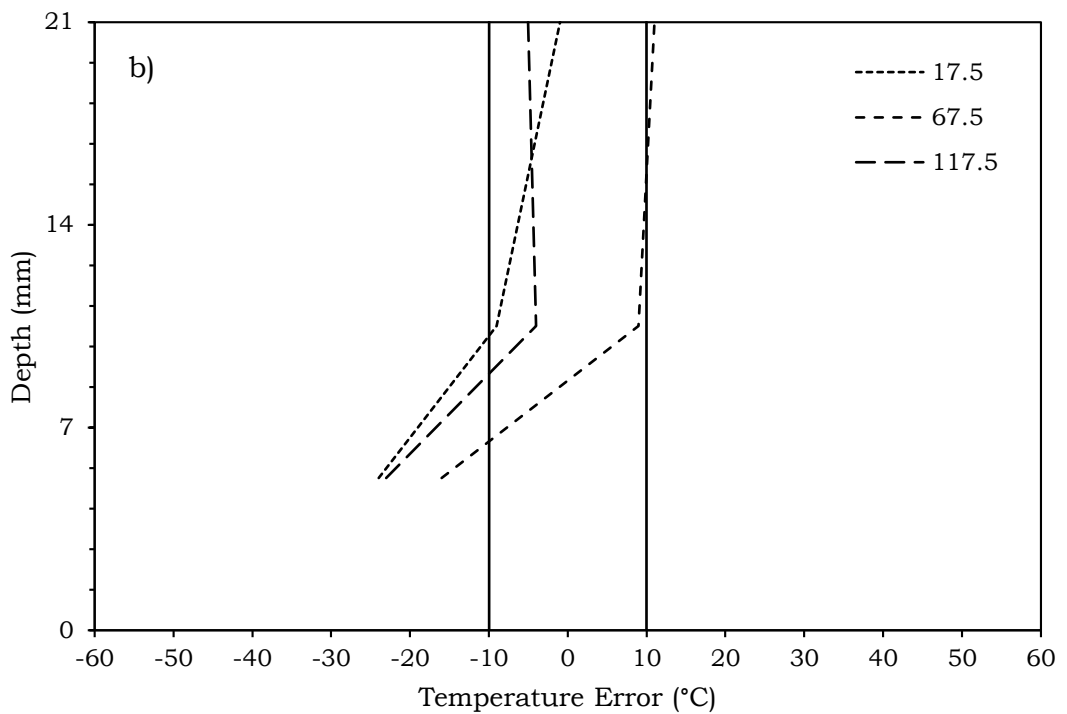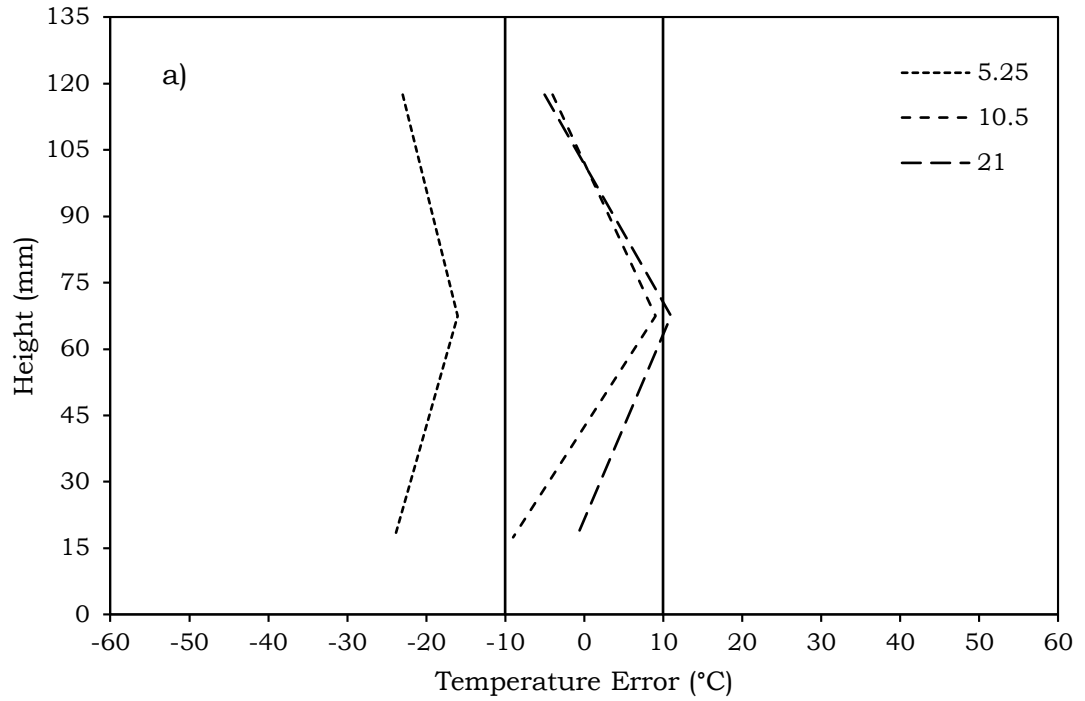expansion behaviour upon soaking has been improved

Figure 24: The results of the test following optimization and adjustment, a) The longitudinal error, b) The radial error. Both are greatly reduced and are more symmetrical about their centres, when compared to the initial results.

3.3.3 The representative volume

The optimization and adjustment procedure was successful in reducing temperature inhomogeneity and internal overheating, however, a temperature gradient still exists, as observed in the results presented in section 3.3.2. Since the internal overheating can be controlled by adjustment, a volume at the core of the specimen must be within the tolerances of the target temperature and is therefore representative of the applied thermal programs. This must be investigated to ensure the representative volume has sufficient scale to allow mechanical testing, and can be quantified using the thermocouple data recorded during testing.

As mentioned in section 3.3.2, Figure 24 shows how the temperature varies radially with depth, as recorded by the thermocouples during soaking. The temperature distribution between each thermocouple is unknown; however, if it is assumed that the temperature gradient between each thermocouple is linear, the depth at which the specimen temperature falls below the tolerance limit can be estimated. Interpolating between the radial thermocouples at each longitudinal location yields a radius at the longitudinal locations from which the representative volume can be calculated, given in Table 5.

Table 5: The representative radii of the TM specimen following optimization and adjustment

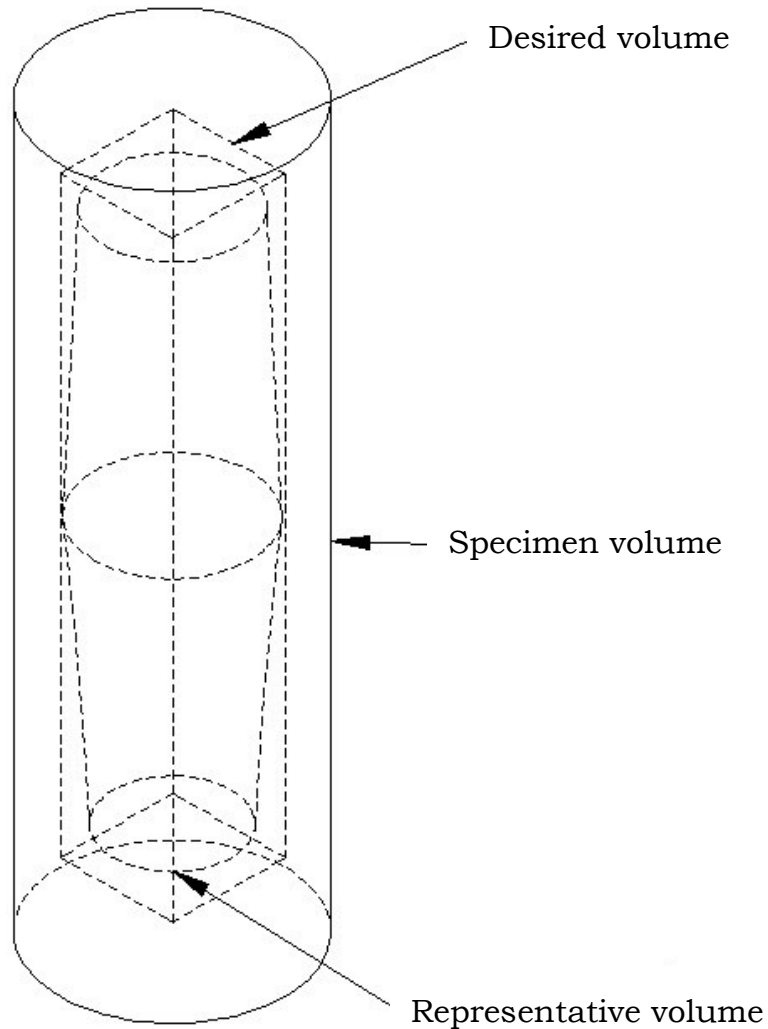| Height (mm)	Depth (mm)	Radius (mm)
117.5	8.082	12.918
67.5	5.25	15.75
17.5	9.175	11.825

Figure 25: An isometric diagram showing the representative volume of a tested HTS specimen, in comparison to the required test volume.

An isometric diagram of the representative volume calculated from the radii is presented in Figure 25. In this figure, the longitudinal temperature gradient between the calculated radii has been assumed linear and plotted to approximate the representative volume. Also plotted is the volume desired by SFIL for mechanical testing of each HTS specimen. The calculations show that at a large core volume of ~67% is representative of the applied thermal program, and that the representative volume largely fills the desired test volume. The representative volume does not equal the desired volume, but the

result evidences that the HTS does possess the ability to produce representative volumes of test material that are large enough to test for both microstructure and mechanical properties from each HTS specimen.

3.4 DISCUSSION

The results in this chapter of work show that following optimization and adjustment, the HTS produces volumes of material that are representative of applied thermal programs, and are large enough to test for both microstructure and mechanical properties. However, some additional observations were noted which deviate from the successes evidenced, and these must be discussed to verify the HTS.

3.4.1 Average thermal expansion

The comparison of thermal expansions between the initial and optimised tests showed large improvement of temperature homogeneity. This is evidenced by the gradient of the optimized plot in Figure 23b) where the thermal expansions at the end of heating and beginning of cooling are very similar in comparison to the initial tests. However, they are not identical, and in the absence of transformations of microstructure, this is thought to be a failure of representing temperature inhomogeneity in plotting the results.

Temperature gradients were shown to exist in the TM specimen during testing both before and after optimization and adjustment, however, the measured thermal expansions were plotted against the temperature profile recorded by the control thermocouple. When compared to all the temperature profiles recorded, the control thermocouple deviated the least from the target temperature, as it was the feedback for the HTS and toggled the applied power. The control

therefore tracked the target temperature within the user defined temperature limits on each set point. The measured thermal expansion is however, a summation of expansions that relate to the temperature gradients within the specimen, and so the thermal expansion does not relate to the control thermocouple temperatures recorded. The thermal expansion must then be considered an average expansion that relates to the average temperature of the specimen. For the TM specimen, a representative average temperature can be determined from the embedded thermocouples. In Figure 26 the measured thermal expansions are plotted against the average temperatures recorded, and alongside the expansions calculated from the 304L characterisation using the average temperature also.

When comparing Figure 26 to Figure 23b), the thermal expansions of the TM specimen are more similar for Figure 26, evidencing the discussions made; however, there remains a large difference between the recorded and calculated expansions. This is discussed below.
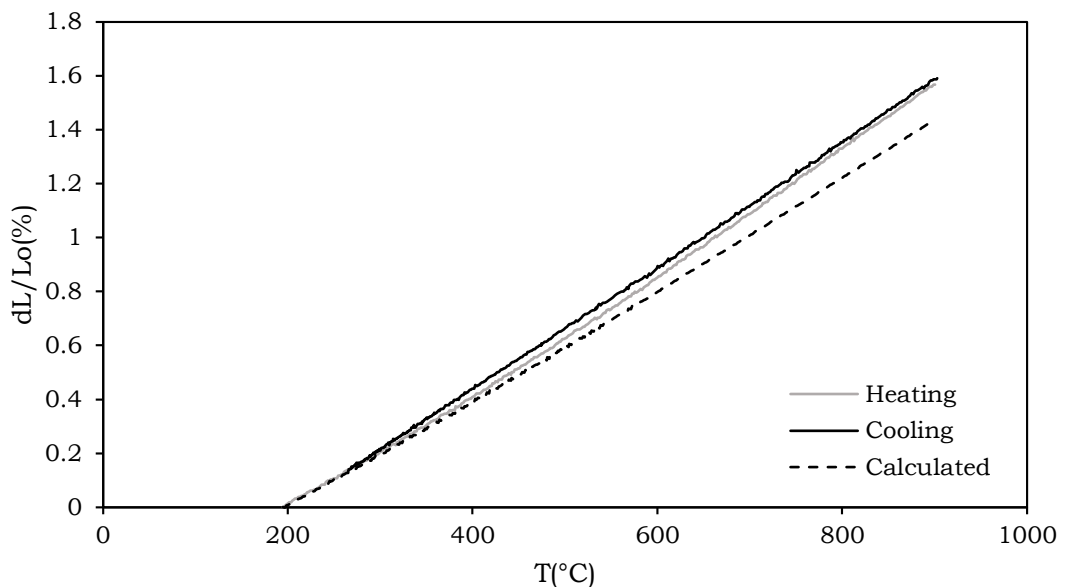

Figure 26 the thermal expansions following optimization and adjustment plotted against the average specimen temperature

3.4.2   Systematic error

It was observed in Figure 23 and 24 that while the optimization and adjustment had reduced overheating to only +1°C, the thermal expansion of the TM specimen remained larger than the expansion calculated from the 304L characterisation. This was also seen in Figure 26 despite the data being plotted against an average temperature profile. The reason for this is systematic error. Systematic error is a repeatable machine error that is present in all the results of a given experiment with equal magnitude. In the HTS, the error is thought to be due to the expansion of machine components due to secondary heating. The HTS heats TM specimens to 910°C that causes a differential linear expansion from 200°C of approximately 1.4%. However, the TM specimens are held in place by a pin and push rod that are in contact with the specimen. It follows that heat will be transferred to these machine components causing them to expand too, and sums with the expansion of the specimen and is measured. The HTS is a differential dilatometer that requires calibration for accurate data to be recorded, but at the time of testing no calibration procedure was developed for the HTS. However, in this work the aim was to investigate the temperature distribution of the HTS specimens, and to optimize performance respectively. Any calibration procedure can only effect the results of thermal expansion and so the temperature results acquired are not affected by the absence of calibration.

3.5   SUMMARY

The aim of the study presented in this chapter was to investigate the temperature homogeneity of HTS specimens during testing, and to optimize the performance of the HTS in this respect. The goal was to produce a volume of material in each specimen tested that was representative of the applied thermal program, and was of sufficient

size that it could be tested for both microstructure and mechanical properties. The findings of the study are summarised below:

1. Initial testing showed that specimens tested by the HTS suffered large temperature gradients and internal overheating. However, the result was predictable and yielded a method for improvement.

2. An optimization and adjustment procedure was developed to generate a representative volume of material within the core of each HTS specimen. This was verified by experiment.

3. The scale of the representative volume was quantified. This volume was found to be a smaller volume than desired by SFIL for mechanical testing, however, the representative volume is large enough to permit microstructure investigation and full scale mechanical testing in each test specimen.

4. The thermal expansions recorded during testing are subject to systematic error, and causes increased thermal expansion to be recorded due to the secondary heating of machine components. A calibration is therefore necessary for accurate analysis of HTS data.

4 ERROR CORRECTION IN LARGE SCALE DILATOMETRY

4.1 INTRODUCTION

The HTS can be considered a large-scale dilatometer that builds on current dilatometry technology by enabling full–scale mechanical characterisation of microstructures produced in specimens, following controlled thermal treatment. However, as a dilatometer, the HTS must provide accurate and reliable dilatation data for analysis too. In Chapter 3 it was identified that the data recorded contained large quantities of systematic error. In this chapter, the systematic error is investigated and reduced by calibration, conforming the HTS to ASTM standards for dilatometry.

4.1.1 Aims and Objectives

When a differential dilatometer heats a test specimen, it also heats the mechanical assembly with which it is in contact. This produces thermal expansion of the machine components in addition to expansion of the test specimen. The expansion of machine components is a characteristic of every differential dilatometer system that in turn

leads to a systematic measurement error. However, because the machine components are the same for each test, the magnitude of error as a function of temperature is repeatable for each repetition of each unique thermal program. Thus, for accurate data to be recorded, every differential dilatometer must be calibrated for each thermal program to remove the systematic error from the results.

The dilatometry calibration procedure is detailed as part of the ASTM standard E228-95 [65], and is achieved by testing a reference specimen with the exact thermal program intended for a test specimen. The reference specimen is made from a standard reference material (SRM) which is a highly detailed and traceable material characterisation [84]. The thermal expansion of the SRM can be calculated, and the difference between the reference specimen and the SRM is the magnitude of systemic error recorded for each test. Once determined, the systematic error can be subtracted from the results of the test specimen to yield absolute dilatation for the test material, for that thermal program.

Commonly used SRMs are alumina, sapphire, silica, quartz and platinum [58,61,62], however, the heating mechanism of the HTS is an induction coil that requires samples to be electrically conductive [80], and therefore the alumina, sapphire, silica and quartz standards cannot be used. Platinum is electrically conductive, but cannot be used due to the large cost of manufacturing a reference specimen to the correct scale.

To calibrate the HTS it is necessary to develop a new SRM, and to test the validity of the new SRM in service, by comparison to the performance of current dilatometer standards.

4.1.2 The Standard Reference Material

The properties that the new SRM should possess must be suitable for the experiments in which it will be used as was discussed in section 2.3.2.1. In the last section it was also discussed that the induction heating mechanism of the HTS requires the new SRM to be electrically conductive [61]. This means that a metallic material is necessary, however, many metallic materials undergo transformations during heating and cooling which effect the thermal expansion characteristics of the material [58]. There have been SRMs developed which do transform upon heating, but these standards are only certified to the onset of transformation, limiting the temperature range in which they can be used. It is appropriate to choose a well-known material that does not have any discontinuities of dilatation within the experimental temperature range. It is also remembered that the SRM must have similar thermal expansion characteristics to the material being tested, as a similar CTE limits divergence of thermal expansion over a large temperature range and improves uncertainty in calibration [58,65]. Another consideration is the oxidation characteristics of the new SRM at high temperature. During testing in the HTS, specimens are in an air environment, and for the reference specimen to be reusable, the new SRM must be resistant to oxidation under cyclic thermal loading at high temperatures.

A potential choice of material for developing the new SRM is the austenitic stainless steel AISI 310, which has many properties that fit well to the new SRM specification. It is a well-known material, which is commonly used in high temperature applications, and there exist a number of published datasets which characterise its thermal expansion properties [73,74,82]. 310 is chromium rich and imparts oxidation resistance due to the formation of thin and stable Cr_2O_3 scale.

The ASTM specification for SS310 is shown in Table 6. The alloying elements contribute to phase stability by either stabilising the austenitic FCC structure, or the ferritic BCC structure. The phase stability of 310 can be indicated using composition to calculate nickel and chromium equivalencies. The equivalences are a summation of the relative strength of alloying solutes to support the existence of either crystal structure. These are plotted on a constitutional diagram that indicates the phase stability at room temperature.

Table 6: Above, the ASTM composition for SS310 (wt. %) [74]. Below, the composition as measured by Inductively Coupled Plasma Atomic Emission spectrometry (ICP-AES).

C	Mn	P	S	Si	Cr	Ni	Fe
0.025	2.00	0.045	0.03	1.50	24.00-26.00	19.00-22.00	Bal.
0.059	1.56	0.032	0.003	0.47	23.7	19.59	Bal.

There have been many constitutional diagrams developed in respect to developments of stainless steels in terms of composition. The original diagram was developed and published by Shaeffler et al. [85], a modern version is shown in Figure 27 [86]. This diagram is accepted as accurate for predicting the phase stability of 310 because it belongs to the family of stainless steels that were used for the elemental regression of the nickel and chromium equivalencies.

The position of the measured composition on the diagram indicates that 310 is fully austenitic at room temperature and since austenite is stable at high temperature, no transformations will occur during heating and cooling. In addition, 310 is an iron based alloy and its FCC crystal structure has high temperature characteristics that do not vary greatly from those of other steels in the austenitic condition. Therefore, 310 is an ideal choice for developing into a new SRM.
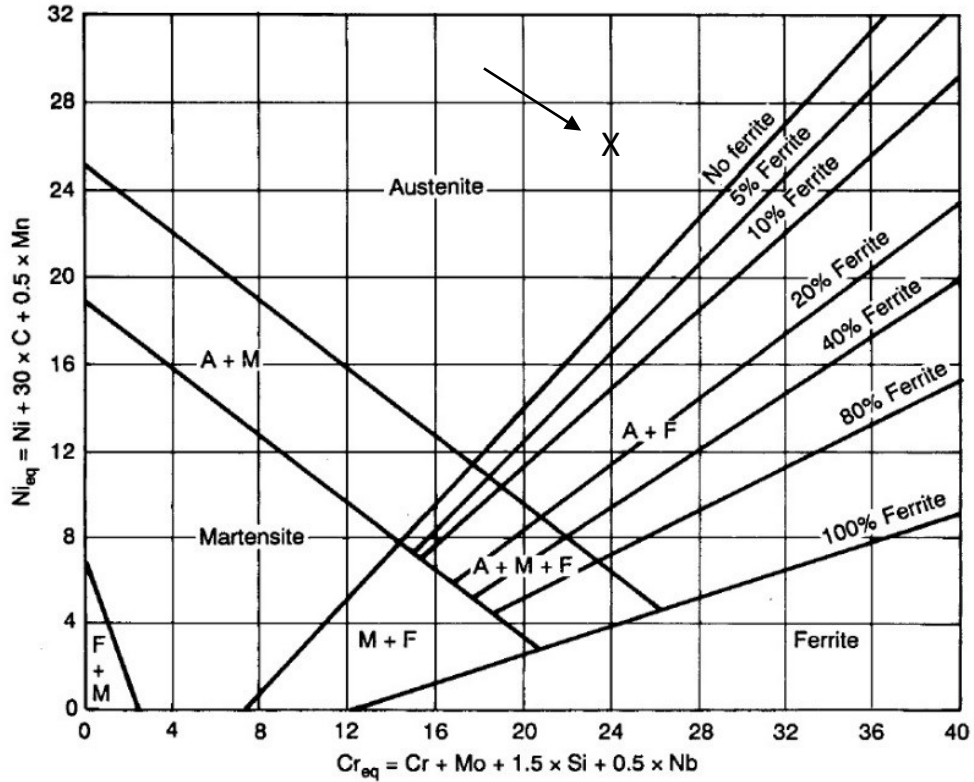
Figure 27: The Shaeffler diagram indicates phase stability as a function of composition

4.1.3   Theoretical Considerations

Thermal expansion is an intrinsic property of materials that is described mathematically by the CTE. Section 2.3.3.2 defined the CTE of a material as the fractional increase in length (thermal strain) of a material, per unit rise in temperature [58,73,74]. This was defined as:

$$\alpha = \frac{\Delta L}{L_0 \cdot \Delta T} \tag{3}$$

Where α is the linear CTE, ΔL is the change in length between two points, ΔT is the change in temperature between the same two points and the L_0 is the original length of the specimen. Equation 3 describes the linear gradient between two measurements, or graphically, the mean gradient between two known points. The CTE is, however, a

104

temperature dependent property which in most metals, gradually increases with temperature [58]. To define the true CTE of a material the gradient at a point must be known [73]. Since the dilatation plot is one of thermal strain against temperature the true CTE can be written as:

$$\alpha_T = \frac{d}{dT}\left(\frac{\Delta L}{L_0}\right) \qquad (4)$$

Where α_T is the true CTE of the material at any point and $\Delta L/L_0$ is the thermal strain at that point, or the dilatation at that point.

If the true CTE is known at any temperature, the dilatation of an SRM can be calculated, and can be subtracted from experimentally determined values to quantify the systematic error for the thermal program. The systematic error or calibration, can then be subtracted from the results of same thermal program applied to the test material to yield absolute dilatations [60,61]:

$$\left(\frac{\Delta L}{L_0}\right)_{CALIBRATION} = \left(\frac{\Delta L}{L_0}\right)_{REFERENCE\ SPECIMEN} - \left(\frac{\Delta L}{L_0}\right)_{SRM} \qquad (10)$$

$$\left(\frac{\Delta L}{L_0}\right)_{TEST\ MATERIAL} = \left(\frac{\Delta L}{L_0}\right)_{DILATOMETER} - \left(\frac{\Delta L}{L_0}\right)_{CALIBRATION} \qquad (11)$$

4.1.4 The Test Material

The test material in this study is steel alloy 20MND5. 20MND5 is a French designation for the alloy SA508 Grade 3 Class 1 discussed in

section 2.2.3, and is used in the same applications. The test material was taken from the testing coupon of a tubesheet forging manufactured at SFIL. Previous to this work, an analysis of the QHT given to this forging was conducted using the HTS [87].

4.2   EXPERIMENTAL

The calibration of the HTS in accordance to ASTM standards for dilatometry was completed by two objectives. The first objective was to characterise the thermal expansion of AISI 310 and create a new SRM. The second objective was to test the validity of the new SRM in service, by calibrating the HTS for the testing of steel alloy 20MND5 under continuous cooling conditions.

4.2.1   Characterisation of SS310

To characterise the CTE for the reference material, a single 310 specimen was tested in a Netzsch 402C dilatometer. The Netzsch 402C is a differential dilatometer that supplies heat to a specimen by an electric coil, and measures thermal expansion by a Linear Variable Differential Transformer (LVDT). The furnace chamber and specimen were submersed in an argon atmosphere during each test. The Netzsch 402C is a differential dilatometer that requires calibration for each test. For these experiments the alumina SRM was chosen for calibration [58,66]. Both the alumina specimen and 310 specimens had dimensions of 6mm diameter and 25mm gauge length. The specimens and experimental preparations conformed to ASTM standard E228-95 for push rod dilatometry [65].

The thermal program applied to the 310 specimen was: 1. heating from room temperature at a continuous rate of 3°C/min to a soaking temperature of 910°C; 2. holding for 30 minutes to allow the specimen

106

temperature to equilibrate; 3. continuously cooling at a rate of 3°C/min to room temperature. The experiment conformed to ASTM E228-95 for CTE determination. This was completed three times to two SS310 specimens with separate calibration for each experiment.

The results for each heating and cooling cycle were plotted individually alongside three published characterisations. Fourteen (14) data sets were averaged, plotted and curve fitted to generate a characteristic equation that defined the thermal expansion of the material. This is the new SRM:
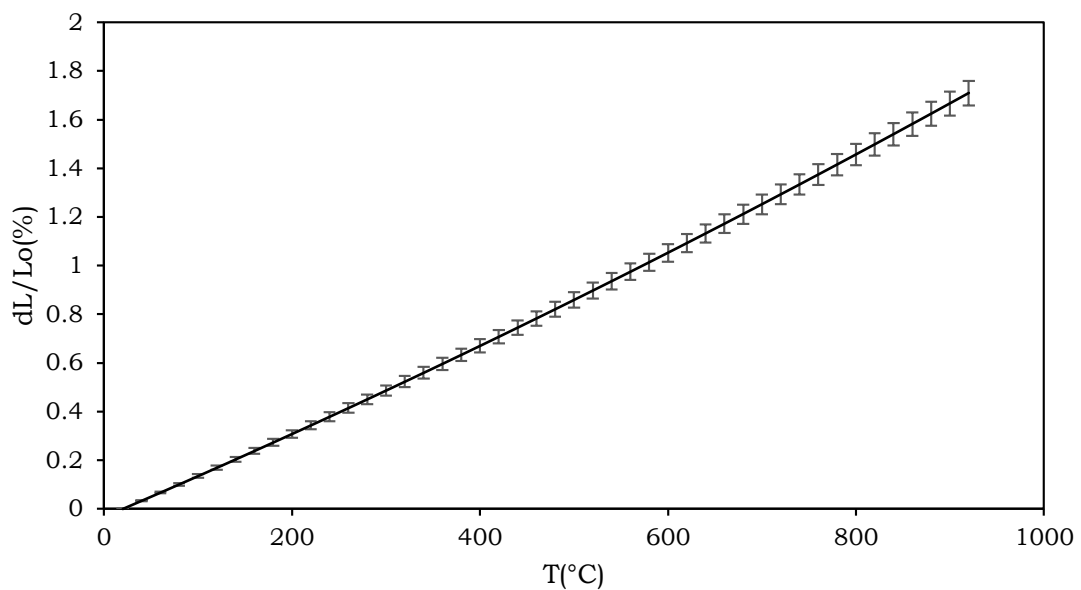

Figure 28: The SRM characterisation of SS310. Uncertainty is found to increase with temperature. Error calculated in 95% confidence.

$$\frac{dL}{L_0} = 0.26193E\text{-}6 \cdot T^2 + 0.15097\,E-2 \cdot T - 0.46484 \qquad (12)$$

The determination of this equation contained uncertainty that was calculated and found to increase with temperature. The maximum

uncertainty occurred at the highest temperature, where the uncertainty of dL/Lo was approximately ±0.05% with 95% confidence.

4.2.2   Testing of 20MND5

To validate the success of the calibration procedure for the HTS, two 20MND5 specimens were tested under continuous cooling conditions, and compared with the results of the same tests completed four specimens using the Netzsch 402C differential dilatometer. The tests consisted of heating at a constant rate of 20°C/min to an upper soaking temperature of 875°C, and cooling at specific rates. The cooling rates tested were 20, 10, 7.5, 5, 2 and 1°C/min, and were applied to 20MND5 specimens both sequentially and repeatedly. The goal was to test the material twice for each rate by using the HTS and Netzsch 402C dilatometer.

Since a large number of tests were completed using each specimen, and that comparable results came from separate specimens with different thermal histories, it was necessary to mitigate the effect of austenite grain growth on the transformation kinetics. This was achieved by soaking the specimens at a low temperature that still produced a homogenous austenitic microstructure. In previous discussions Pous-romero et al. [30] characterised austenite grain growth in SA508 Gr.3 Cl.1 at different soaking temperatures. Their results showed that grain growth was significantly retarded when soaking at temperatures below 910°C:
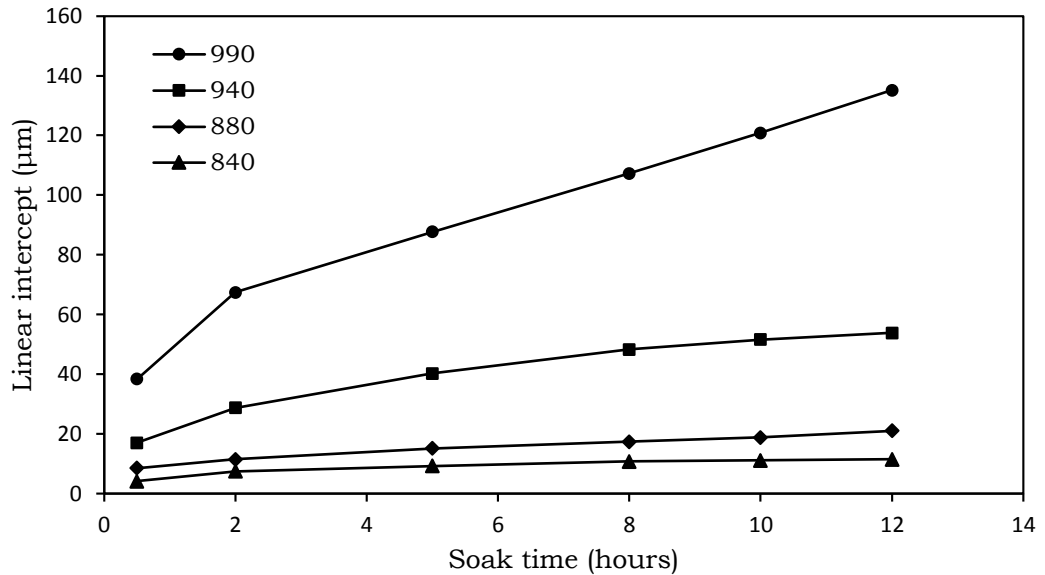
Figure 29: Austenite grain growth in SA508 Gr.3 Cl.1 as a function of time at specific soaking temperatures. Taken from the 2013 work of Pous-romero et al. [30]

To determine correct soaking temperature, the A_{C3} temperature of the test material was determined from its composition using Andrews' formula [78].

$$A_{C3}(^{o}C) = 910 - 203\sqrt{C} - 15.2Ni + 44.7Si + 31.5Mo \qquad (13)$$

The composition of the test material was determined by Spark OES, x-ray fluorescence (XRF) and energy dispersive x-ray spectroscopy (EDS), and was found to exist within the ASTM compositional limits of SA508 Gr.3 C.1 as shown in Figure 30. Values are omitted due to industrial sensitivity.
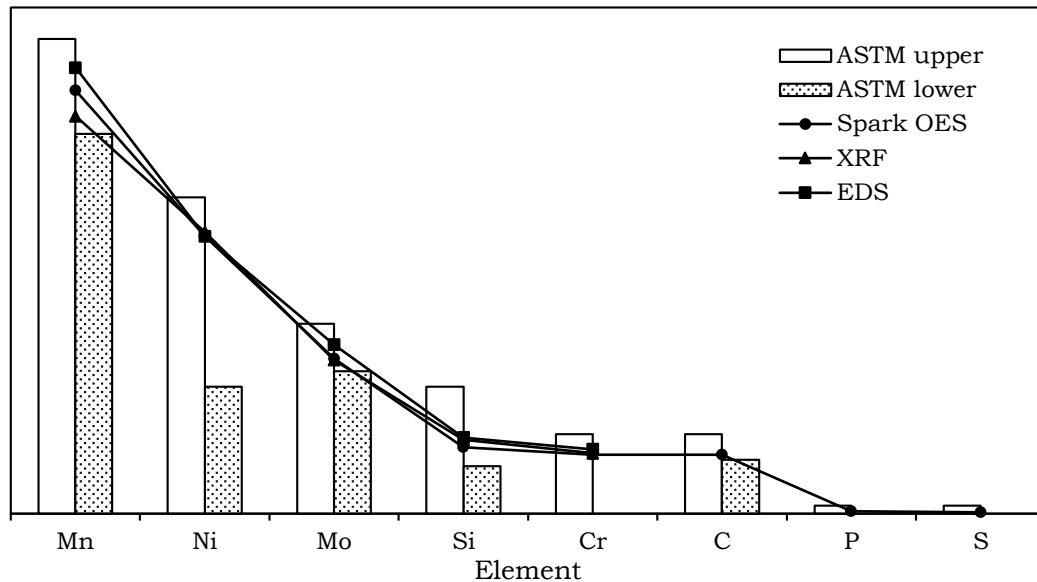
Figure 30: The composition of the 20MND5 test material as determined by Induction
Coupled Plasma Optical Emission spectroscopy (ICP-OES), XRF and EDS.

From the measured composition, Andrews' formula predicted an
average A_{C3} temperature of ~835°C, thus a midway soaking
temperature of 875°C was chosen to ensure complete transformation
to austenite, while limiting austenite grain growth in respect to the
work of Pous-romero et al [30]. Grain growth at this temperature was
then tested using the Netzsch 402C by cycling a single specimen with
a single program and monitoring changes in transformation kinetics
for each repetition. If austenite grain growth occurred, the total grain
boundary area will become reduced. Since diffusional forms of ferrite
nucleate at grain boundaries preferentially [69], the volume fraction of
ferrite will be reduced following transformation should the PAGS
increase with increased numbers of cycles. The program used to test
this hypothesis was: 1. heat the specimen at 20°C/min to 875°C. 2.
Soak at 875°C for 30 minutes. 3. Cool continuously at 3°C/min to
200°C. This program was cycled 5 times. The cooling rate was chosen
to conform to ASTM standards for CTE determination [64]. This rate is
assumed to produce near equilibrium microstructures and it was
assumed that a quantifiable volume of ferrite would be transformed for
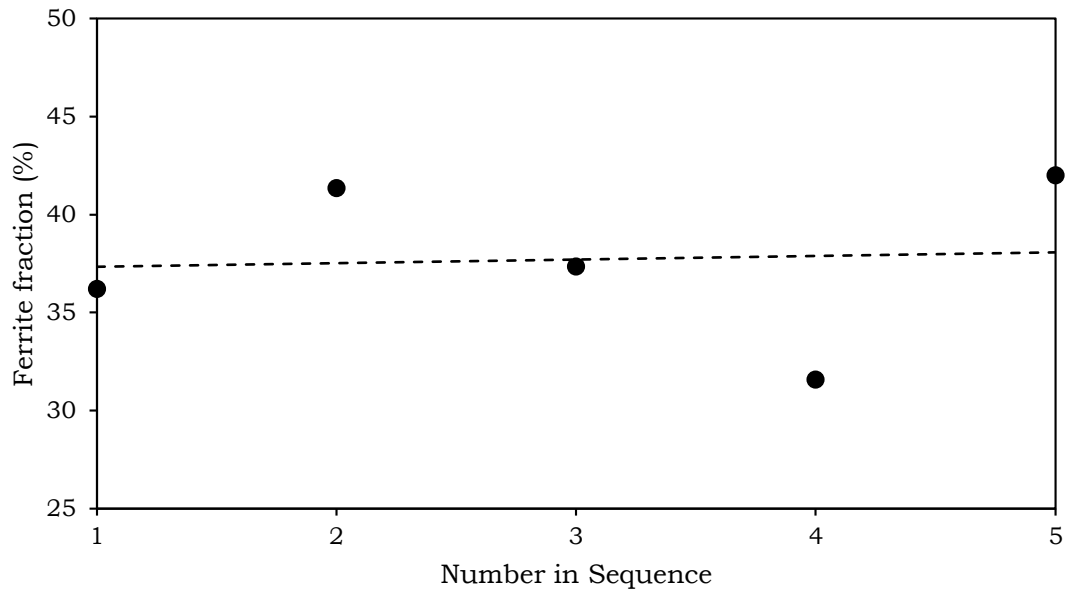this rate as indicted in the CCT diagram in Figure 10.

110

Figure 31: The result of the cycling experiment shows that the ferrite volume fraction does not change with the number of cycles performed, implying that PAGS did not change respectively.

Following confirmation of the experimental parameters, 20MND5 specimens were prepared and tested. For both the HTS and Netzsch experiments two specimens were used. The HTS specimens had the standard dimensions as shown in Figure 19, the Netzsch specimens had the dimensions detailed previously. All the specimens tested were manufactured from the same stock material, and on commencement of the experiment, it was assumed the initial microstructure of each specimen was identical and homogenous.

4.3 RESULTS

4.3.1 SRM Baselines

The AISI 310 reference specimen was tested for each cooling rate to generate error baselines. The measured dilatation from each reference test was plotted alongside a SRM calculation using the average temperature recorded during each reference test. The difference between the reference test and SRM was calculated, plotted and fitted

111

with an appropriate polynomial equation, which quantified the systematic error for the test as a function of temperature. This is the baseline for that specific test. For each cooling rate tested, two baselines were generated to assess repeatability.

In Figure 32a), the measured dilation of a reference test at 20°C/min is plotted. The result shows the dilatation of the reference specimen is greater than the SRM calculation, implying that the error contributions increased the magnitude of the measured dilatation. As previously discussed, the systematic error also reduces with temperature to become negligible at the arbitrarily chosen datum temperature of 200°C. The dilatation of the reference specimen during the test appears to be linear, however the difference between specimen and SRM, plotted in Figure 32b) shows the error of measurement reduces cubically with temperature within the tested range, at first more slowly, then accelerating at approximately 400°C. This trend however, is not the same for each cooling rate tested.

In Figure 33 the baselines are plotted for all the tested cooling rates. Chart a) contains the first set of baselines generated that measured accurate temperature tracking to within an allowable limit of ±10°C on the target temperature. Chart b) shows the second set of baselines generated, which measured an internal over heating of ~3°C above the allowable limit during soaking. Both sets of baselines show similarity despite the internal over heating measured in the second set. In both sets, the characteristics of error for each cooling rate are different, and change systematically with cooling rate as implied by the similarities between them. This indicates that the systematic error is not only due to expansions of machine components, but also due to the specimen's response to the HTS function with respect to the input parameters controlling for each test.

a)

20°C/min

dL/Lo(%)

SRM
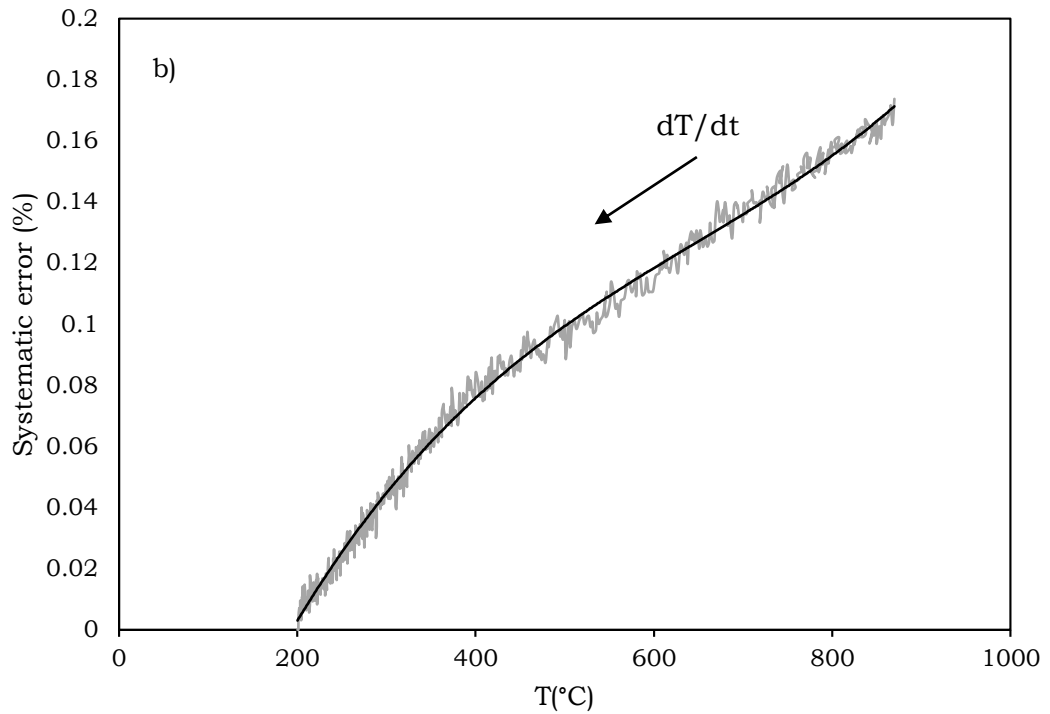
dL/Lo

T(°C)

b)

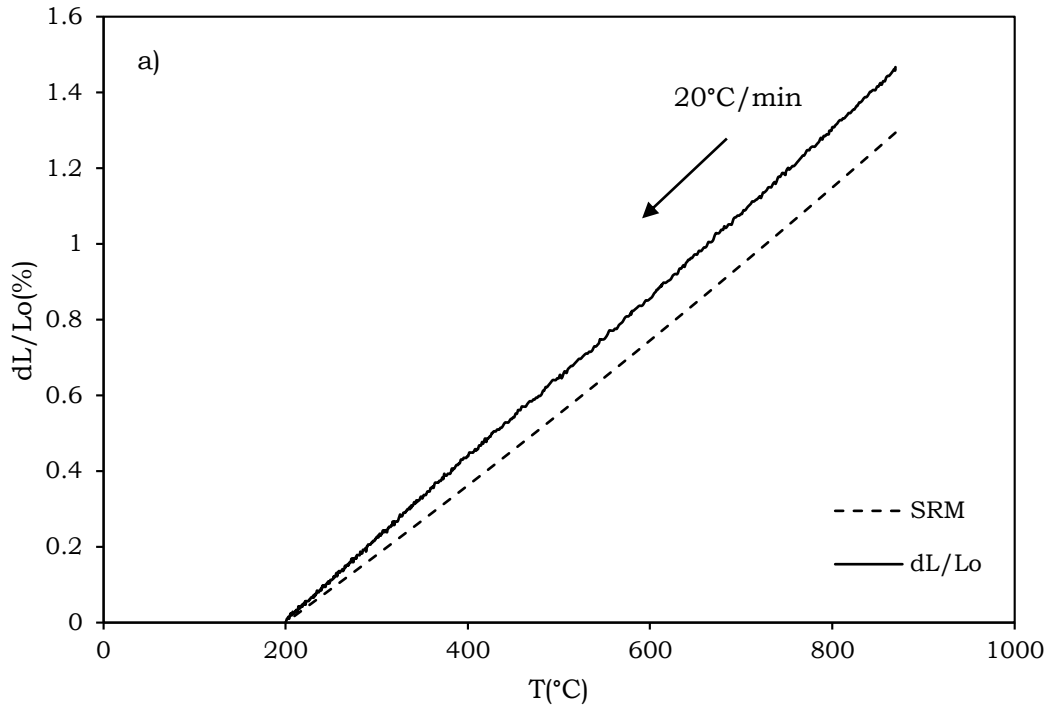dT/dt

Systematic error (%)

T(°C)

Figure 32: a) The recorded dilatation when cooling at 20°C/min and the SRM plotted against the average specimen temperature. b) The difference between the dilatation of the reference specimen and SRM quantifies the systematic error for the test.
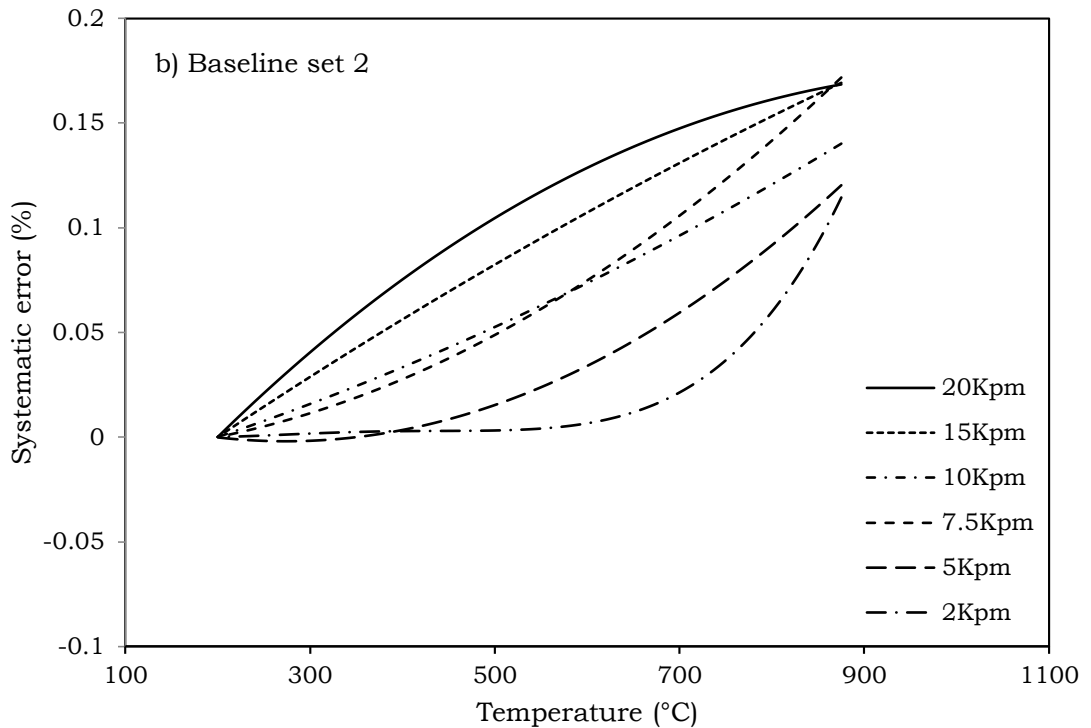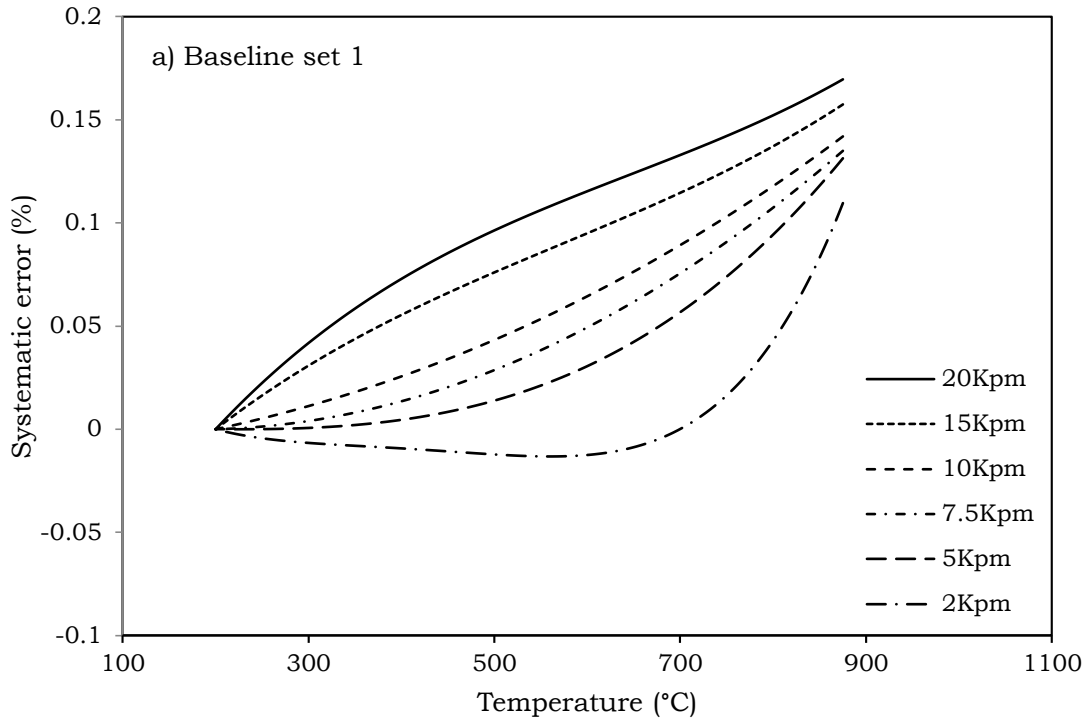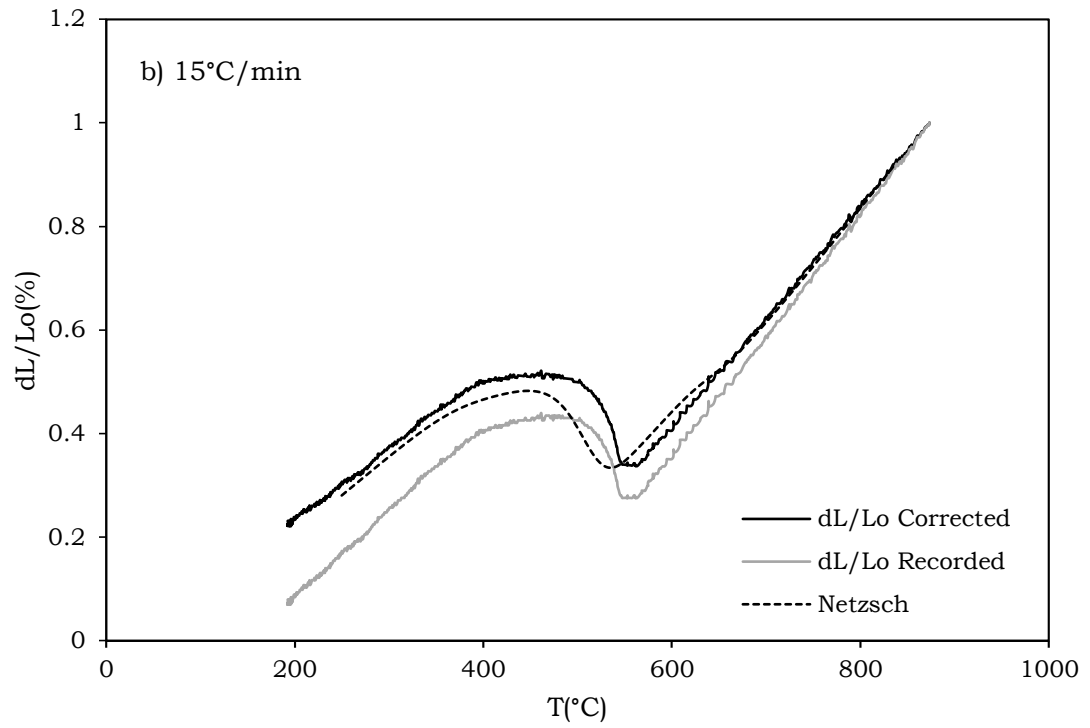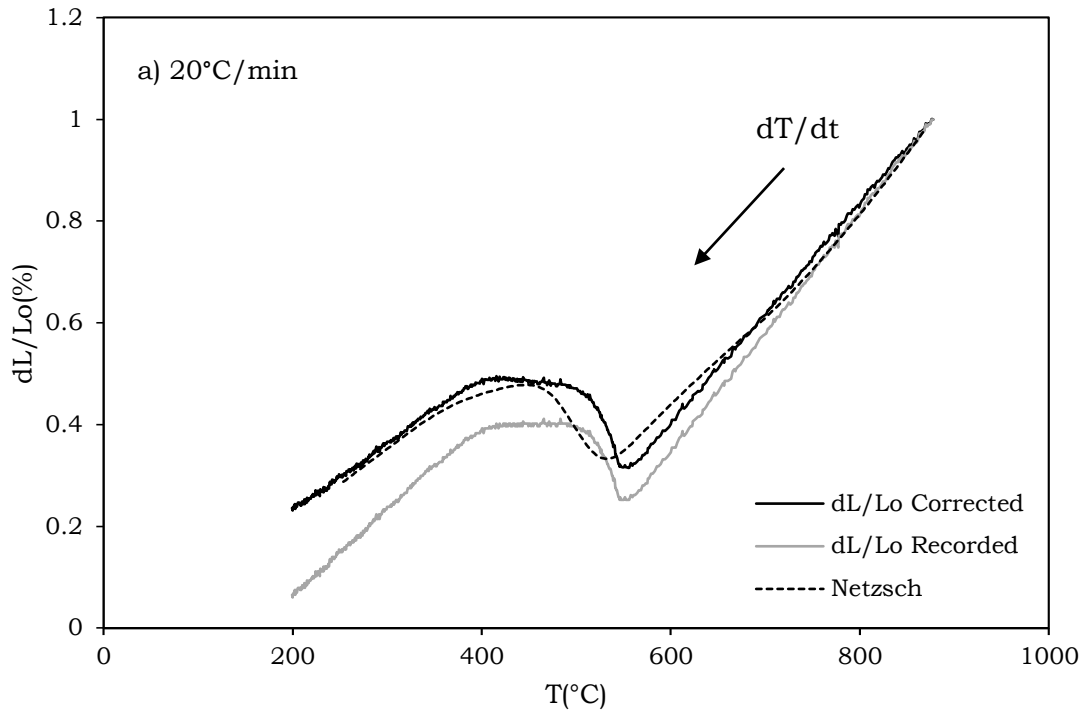
Figure 33: The systematic error as a function of temperature for the cooling rates tested. The result implies systematic error to be a function of temperature, and is characteristic of each cooling rate. a) The temperature tracking is accurate, b) the temperature tracking showed internal over heating of +3°C.
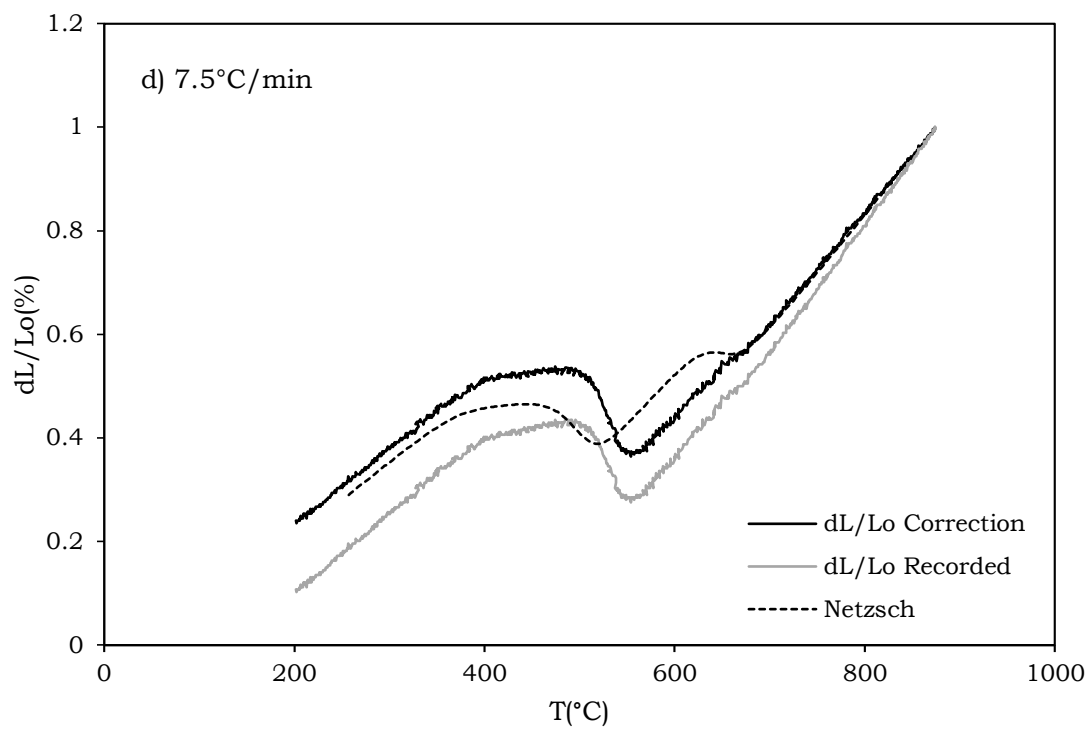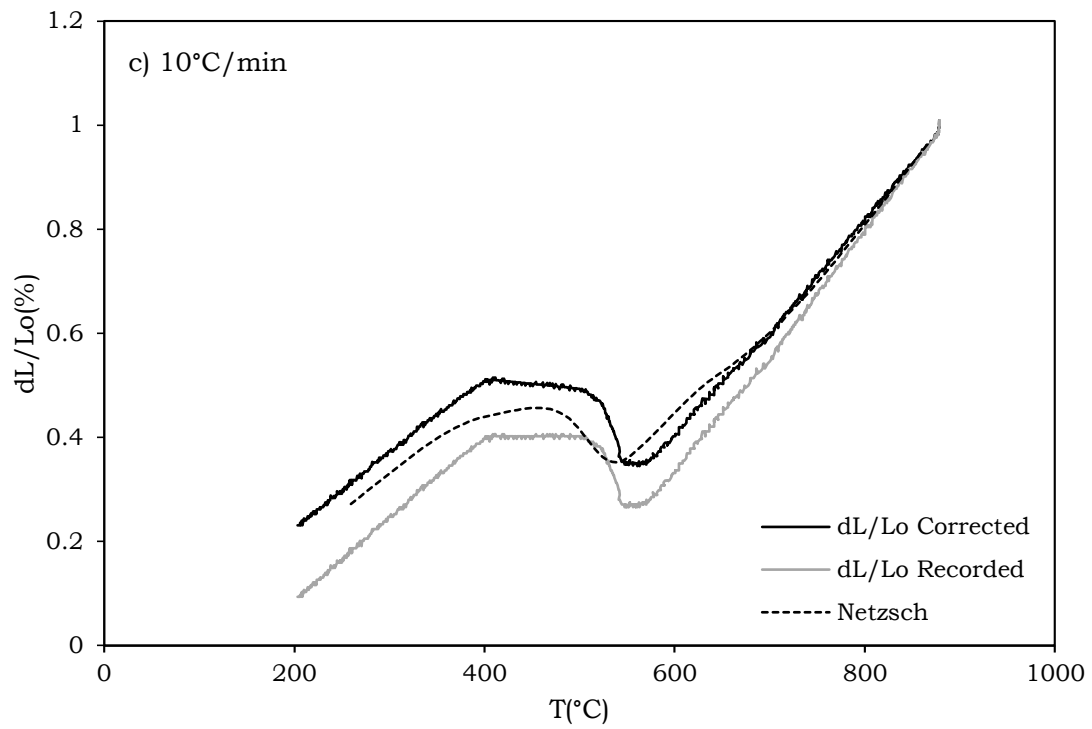
4.3.2 20MND5 Calibrations

The baselines were used to correct the data from each test using 20MND5 specimens. These were plotted alongside the results attained from the tests completed on two Netzsch 402C differential dilatometers. Two measures were used to verify the success of the calibrations for each test. These were the relative dilatation of the specimens between two known temperatures, before and after transformation, and the true CTE of the test specimens at those temperatures.

Figure 34 shows the results of the calibrations made with baseline set 1. In the charts the dilatation upon the onset of cooling has been equated to allow comparisons to be made, hence, the dilatation ordinate has been omitted from each chart, respectively. This is because the final microstructure of 20MND5 is a function of cooling rate; hence, it is most accurate to align data for comparison at high temperature where it is known the microstructure of all specimens is fully austenitic. The systematic error remains a function of temperature and will during normal expansion, decrease with decreasing temperature as previously discussed.

Comparisons between the dilatation plots show that improvement has been made to the HTS data for each test, both in terms of the true CTE and dilatation before and after transformation, however, some differences between them are noted. An apparent difference is the dilatations of the Netzsch and the calibrated HTS specimens following transformation. These appear to diverge as cooling rate decreases. A second observation is that the deviations from linearity that characterise transformations differ in magnitude between the HTS specimens and the Netzsch specimens for each test.

a) 20°C/min

dT/dt

— dL/Lo Corrected
— dL/Lo Recorded
---- Netzsch

b) 15°C/min

— dL/Lo Corrected
— dL/Lo Recorded
---- Netzsch

c) 10°C/min

dL/Lo Corrected
dL/Lo Recorded
Netzsch

d) 7.5°C/min

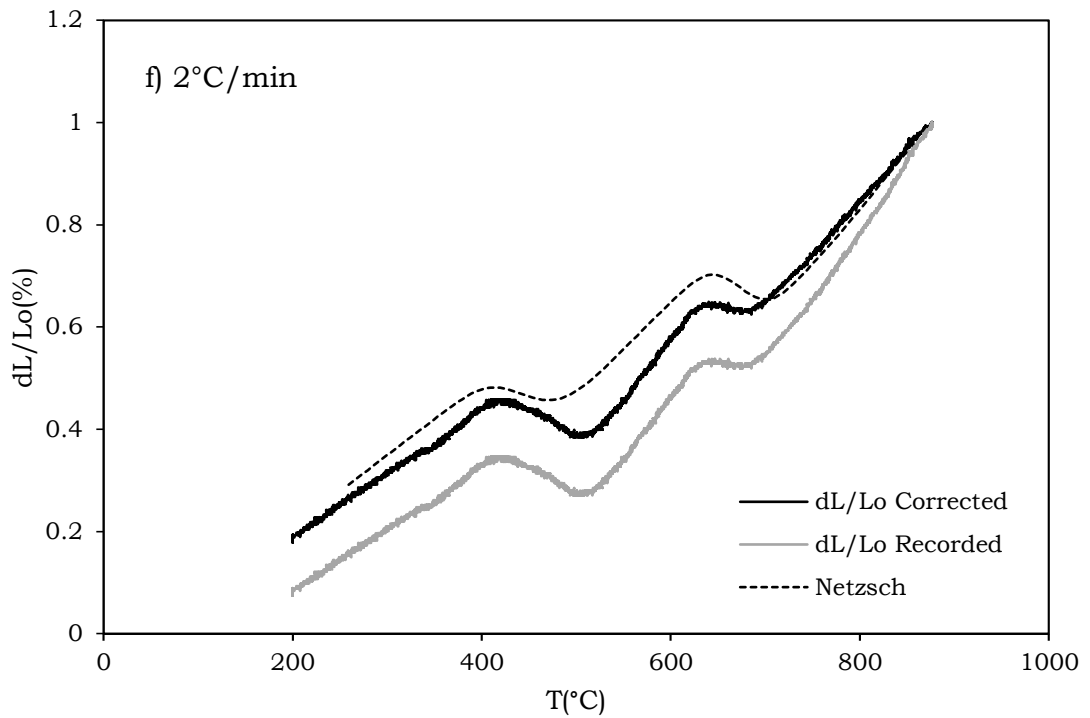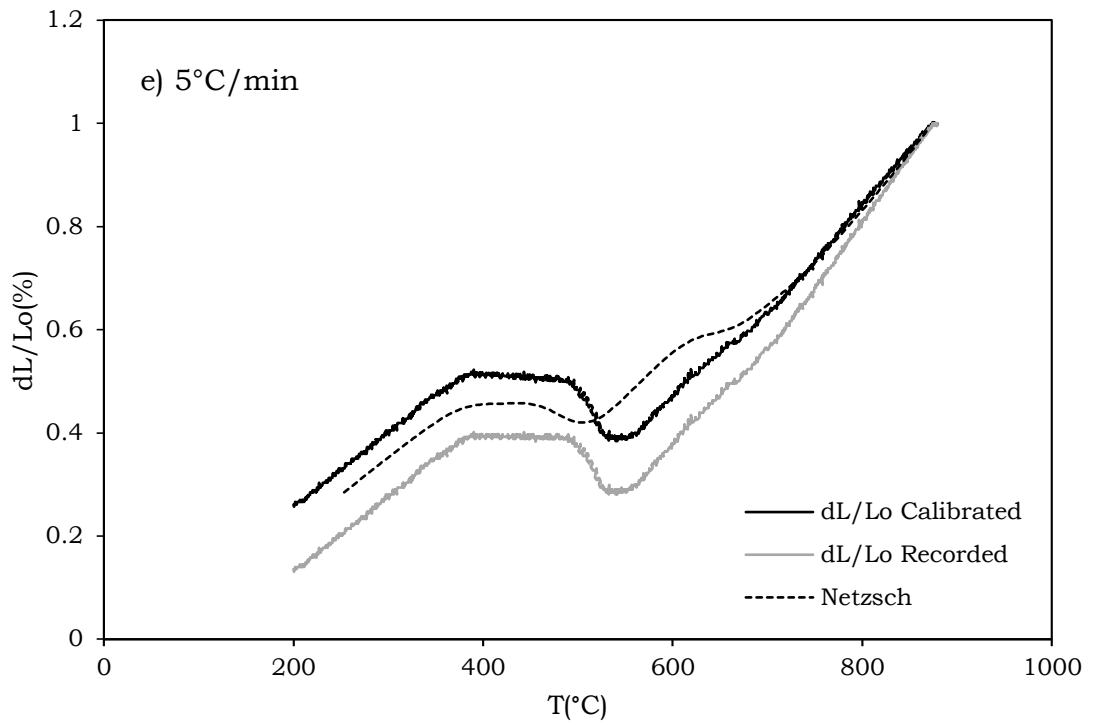dL/Lo Correction
dL/Lo Recorded
Netzsch

Figure 34: The results of correcting the HTS for testing 20MND5, using the new AISI 310 SRM

The dilation charts in Figure 34 positively indicate the success of the new SRM and calibration procedure; however, for success to be confirmed, the performance of the calibration must be quantified.

In Figure 35a), the true CTE for each test is calculated at the temperatures of 750°C and 300°C respectively. At 750°C, the difference between the calibrated and recorded HTS values appears to diverge with decreasing cooling rate. Initially, the recorded HTS values appear similar to the Netzsch results; however, the CTE quickly deviates, while the calibrated values remain similar to the Netzsch values at each cooling rate.

At 300°C, the calibrated and recorded CTE's appear to converge with reducing cooling rate, becoming almost identical at 5°C/min. The calibrated values are more similar to the Netzsch values throughout, however at the rate of 2°C/min both calibrated and recorded HTS CTE values are much less that the Netzsch CTE, and are more similar to each other.

In Figure 35b), the dilatation between the temperatures of 750°C and 300°C is presented. The chart indicates that the relative dilatation between these two temperatures remains greater for the recorded HTS data than for the calibrated data. In addition, the calibrated data remains more similar to the Netzsch throughout; however, it is observed that the difference between the Netzsch and calibrated HTS values increases with reduced cooling rate, as was indicated in the dilatation plots of Figure 34.
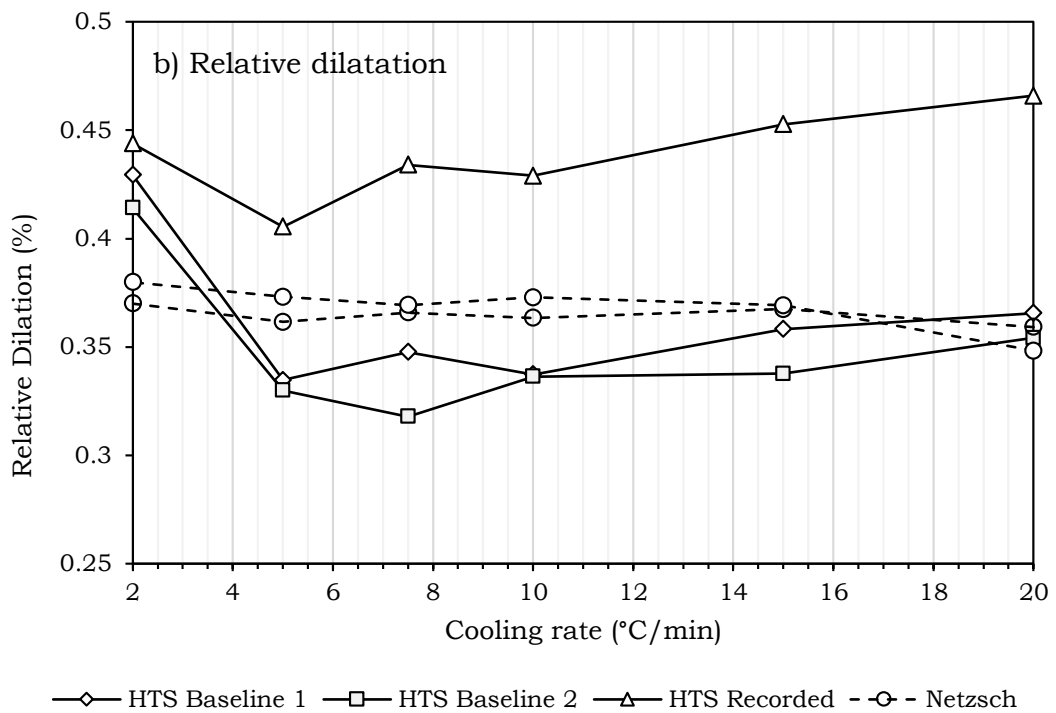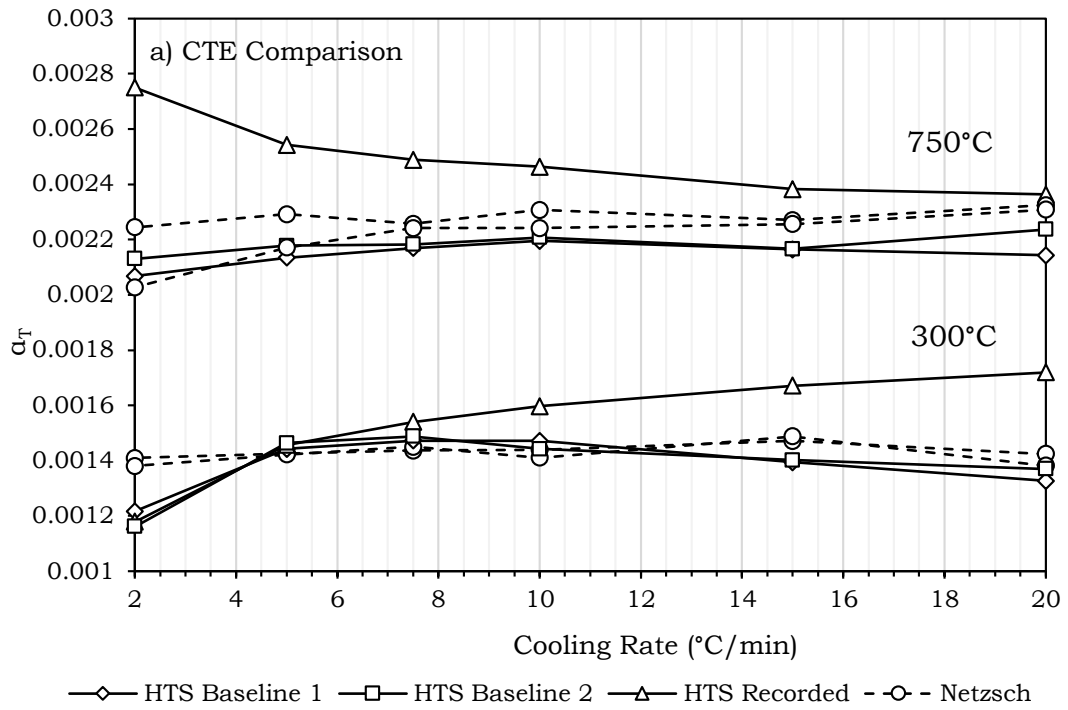
Figure 35: a) The variation of true CTE at 750°C and 300°C. b) The differential dilation of the specimens tested, between 750°C and 300°C.

4.4 DISCUSSION

4.4.1 Baselines

4.4.1.1 Characteristic error

The cooling behaviour of the HTS test specimens is a function of both the measured dilatation of machine components, and the response of the HTS to the input parameters. This is indicated in the form of the baseline equations that quantify the systematic error for each test, and is evidenced by the similarities between independent results for the same test parameters, as in Figure 33. However, while the behaviour of the specimens is evidenced as characteristic of the input parameters of each test, it does not explain why this is the case. To explain, the operation of the HTS must be considered.

The HTS heats each specimen by an induction coil that is controlled by a surface mounted K-type thermocouple. When the temperature is above or below the user defined limits on either side of a specific temperature set point, the induction coil is either on, or is switched off respectively. During cooling, heat is dissipated from the specimen surface primarily by natural convection. Internally, heat must be conducted to the surface to be dissipated. During rapid cooling, the dissipation of heat exceeds the rate of conduction. The induction coil is switched on when the surface temperature drops below the set point limit, when internally, the temperature remains greater than the surface. The induction coil provides heat through the thickness of the specimen; therefore, the average temperature becomes greater than the surface. This is measured by the HTS as an increased dilatation for the same temperature, and hence an increased quantity error is generated.

The opposite is true of slow cooling rates. Here the additional time allowed for cooling between set points, permits conduction of heat to the surface and prevents the induction coil from being switched on. The effect is a rapid reduction of error when cooling through high temperatures, which then slows as the internal temperature falls, inverting the driving force for conduction to the surface.

To show this, the difference between the control thermocouple and the average temperature was calculated for the baselines. This is plotted in Figure 36. What was found was that the difference between control and average for the test at 20°C/min reduced with reducing temperature, with the average being consistently greater, having maximum difference of approximately +5°C when at higher temperatures. The difference between control and average temperature of the specimen tested at 2°C/min however, increased with reducing temperature, with the average temperature of the specimen being consistently less than the control and having a maximum difference of approximately -15°C at low temperatures.
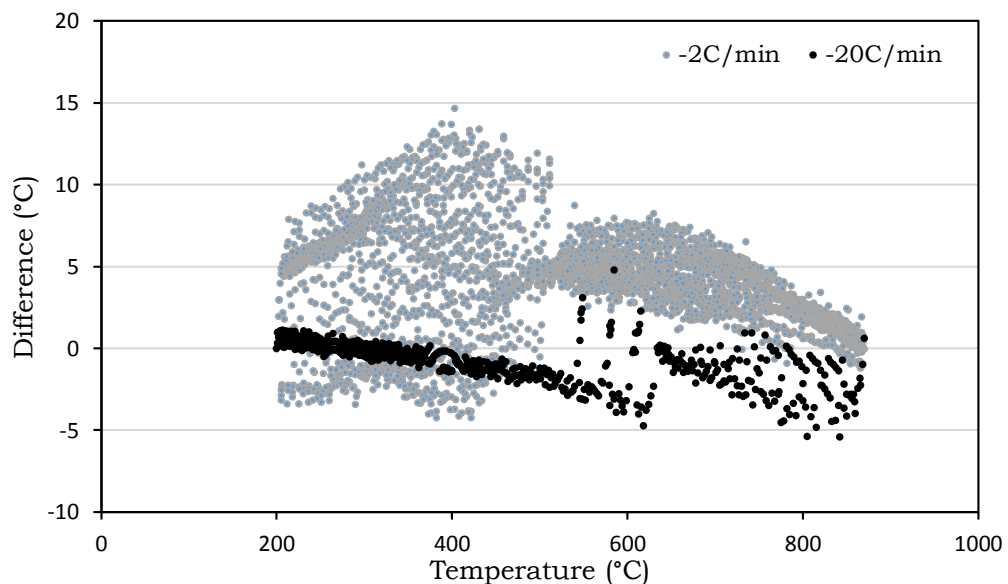

Figure 36: The difference between the control temperature, and the average specimen temperature for the SS310 reference tests at -20°C/min and -2°C/min.

This strongly suggests that the systematic error inherent of using the HTS, is a function of the input parameters, and is characteristic of them. However, since the systematic error can be quantified using the new SRM, the negative effect of this error on the results from testing using the HTS, can be greatly reduced.

4.4.2 Calibrations

The baselines were used to calibrate the HTS for testing 20MND5 specimens, and the success of the calibration was quantified by comparing the true CTE and relative dilatation of the specimens with control experiments, between two known temperatures. In this case, a set of identical experiments were completed on two existing and standardised, scientific dilatometers. The dilatation charts, presented in Figure 34, show visually that the calibration has improved both the CTE and dilatation of the HTS data; however, some unique features were noted. The performance measures were quantified from the dilation charts and presented in Figure 35, which showed that the calibration had corrected both CTE and relative dilatation disproportionately. This is now discussed below.

4.4.2.1 CTE

In Figure 35 the CTEs of each test following calibration are shown. The CTEs following calibration with both sets of baselines show strong similarities with the Netzsch data, and are improved over the recorded values. However, the result at 300°C shows the HTS CTEs before and after calibration converge on similar values, despite the dilatation being corrected by a significant quantity.

The CTE is an intrinsic property of a material that depends upon phase stability. For 20MND5, many transformation products can form as a

function of cooling rate, and at specific temperatures, transformation products and their volume fraction determine the CTE. The convergence of the CTE at 300°C as recorded by the HTS, to a similar value as the Netzsch and calibrated data, shows that the microstructures of the HTS and Netzsch specimens following transformation is similar too. However, to measure this accurately before calibration implies that the characteristic error discussed above is negligible for the input parameters at which convergence occurred. Considering the CTE's at 750°C it is noted that for all dilatation plots in Figure 34, the CTE of the recorded data is greater than the calibrated data, however, it is seen that through cooling to this temperature, the microstructure of all the tests is austenite, which has the same CTE for all tests for the same material. The larger CTE measured must then be due to the systematic error, which as previously discussed, remains greater at higher temperatures for faster cooling rates. At low cooling rates this error falls rapidly, to converge on the control and at the rate of 5°C/min becomes low enough for homogeneity of temperature before transformation begins. The result is the transformation of similar microstructures between the Netzsch and HTS, hence a very similar CTE with reduced cooling rate. Since the characteristic baselines reflect this trend, it follows that the gradient of the dilatation with respect to temperature following transformation requires less correction for lower cooling rates, and the thermal expansion of machine components is the only significant correction following calibration for cooling rates of 5°C/min and lower.

4.4.2.2 Relative Dilation

In Figure 34 it was noted that a divergence of dilatation between the Netzsch and calibrated data occurred for decreasing cooling rate. Following transformation, the values of the calibrated data appeared larger than the Netzsch values for the same temperatures. This was quantified in the calculation of relative dilatation, plotted in Figure

35b), and can be explained by considering the temperature profile of the HTS specimens, and the effect of this on the results by calibration.

The calibration procedure permits removal of systematic error from the results of testing using the HTS, but the quality of the calibration is dependent on the repeatability of the HTS. For example, consider the temperature profiles for the baseline and test specimen at 5°C/min, shown in Figure 37. The baseline chart Figure 37a) shows a near symmetrical profile both longitudinally and radially with little overheating above the target limit. However, a large amount of material remains below the lower limit of temperature, which by interpolation yields a volume fraction of representative material of ~67%. The chart of the test specimen in Figure 37b) shows better radial homogeneity than the baseline, but less longitudinal symmetry. Importantly, a large volume through central longitudinal volume is above the target limit by ~7°C.

a) 5°C/min baseline
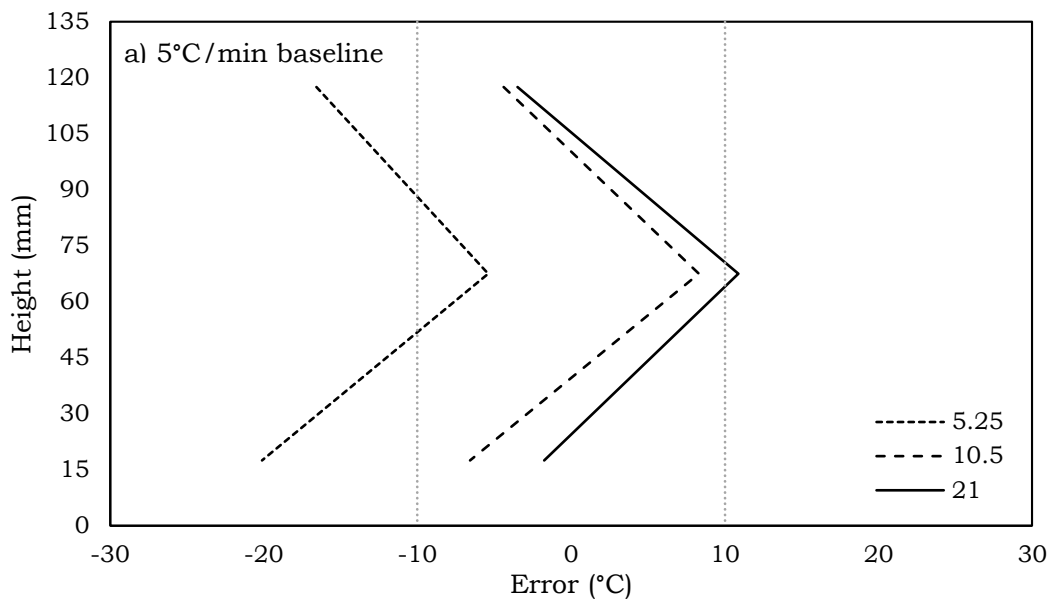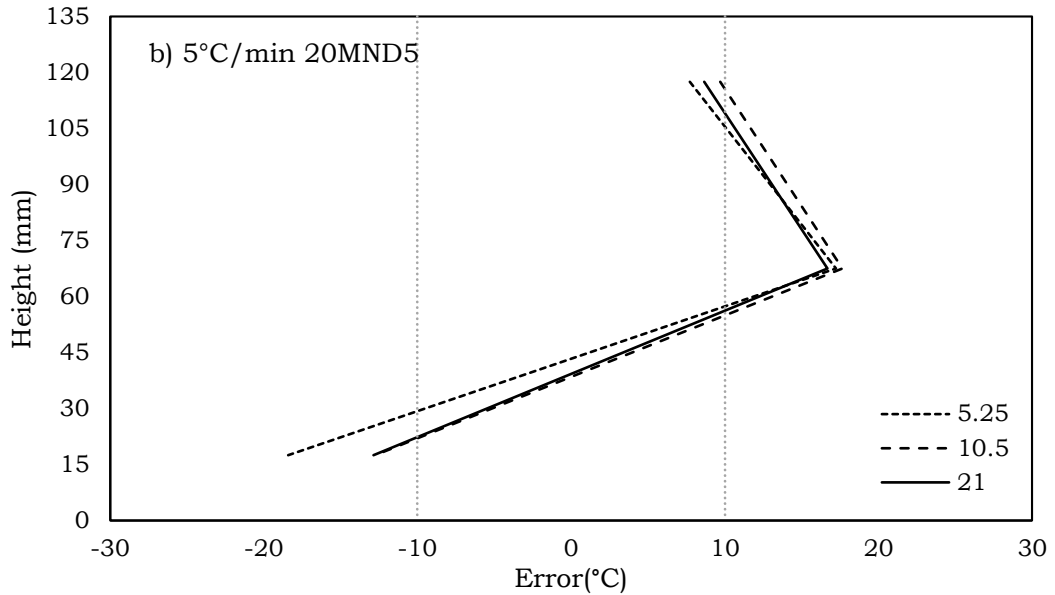
Figure 37: a) The longitudinal temperature profile of the 310 reference specimen b) the 20MND5 test specimen, upon soaking at 875°C. The vertical markers indicate the industrial limitation on temperature variation during experimentation.

Earlier, the baselines were discussed to be characteristic of input parameters, and at low cooling rates have reduced error. The baselines are used to calculate error from the average recorded temperature of the test specimens; however, the baseline does not contain the additional characteristic of overheating present in the test specimen at lower temperatures. In addition, the volume of material that is representative of the target temperature is greater in the test specimen, due to the increased radial temperature homogeneity. Since the baselines quantifies dilatation as a function of average temperature, the calibration does not account for the increased temperature homogeneity of the test specimen, and this translates through calibration as increased dilatation for the same temperature when compared to the Netzsch data.

4.4.2.3 Transformations

In section 4.3, the transformation events that occurred during the testing of 20MND5 were shown. The deviations from linear dilatation

126

that characterise the magnitude of each transformation event differ between the calibrated HTS and Netzsch data, and this must be discussed.

The important transformation event that relates to this observation is the ferrite transformation, which is the first transformation event to occur during cooling from austenite. Ferrite transforms at low undercooling, and the volume fraction transformed is strongly affected by cooling rate [88]. At low cooling rates, a greater volume fraction is transformed, and this is visible as a greater deviation from linearity of the dilatation plot. What is observed is that the calibrated HTS data did not deviate as greatly for the ferrite transformation as in the Netzsch data, implying that a smaller volume fraction of ferrite was transformed in the HTS specimens. This can be explained by considering the representative volumes of the Netzsch and HTS test specimens.

The Netzsch specimens are small and heated in a tube furnace under furnace control. In this arrangement, the specimen temperature can be considered homogenous because the specimens are small, and suffer negligible temperature error for the cooling rates tested. The measured dilatation can therefore be considered representative of the entire specimen. The HTS specimens, however, are more than 9 times greater in volume and tested in stagnant air, the temperature being controlled by conduction through the specimen. Temperature inhomogeneity occurs during each test as can be inferred in Figure 37, and therefore the measured dilatation is a summation of an infinitesimal number of dilatations that relate to discrete temperatures at every point in the specimen. For this work, the average temperature was used to plot representative data when compared to any of the individual thermocouple measurements; however, the measured dilatation is the dilatation of the entire volume, and not the

representative volume to which the average temperature relates. The representative volume can be calculated from the thermocouple data and ensures accurate physical characterisation can be completed, however, there is no working relationship yet developed, which relates the representative volume to the measured dilatation, and therefore the HTS cannot be used to characterise accurately the magnitude of transformation events at present.

4.5   SUMMARY

The aim of the work presented in this chapter was to develop a new SRM specifically for calibrating the HTS, and to test the validity of the SRM in service by comparison to the performance of ASTM dilatometer standards. The main findings of the work completed are summarised below:

1. A new SRM has been developed and used to calibrate the HTS by removal of systematic error for six unique, idealised experiments. Results show the calibration has been successful in improving the data recorded from all the experiments completed, when compared to existing standards.

2. The baselines generated showed that systematic errors removed by the calibration consist of expansion of machine components, and the characteristic thermal response of the specimens to the input parameters of each program. The effect of both on the results of the experiments is positively reduced by calibration.

3. While the new SRM and calibration improve results, some error remains due to the repeatability of the HTS. Limited repeatability is due to experimental or random error present in each

experiment, and cannot be mitigated by any systematic procedure.

4. While the HTS produces a representative volume of material from which physical characterisation is possible, temperature inhomogeneity is present, and contributes to the measured dilatation. Therefore, the magnitude of specific transformation events indicated in the HTS data cannot not be considered representative.

5 AN EXPERIMENTAL METHOD OF PREDICTING PROPERTY VARIATION IN LARGE FORGINGS

5.1 INTRODUCTION

Validating new materials and heat treatments for large forged steel components is often a long and iterative process, due to uncertainties of through thickness variations of microstructure and mechanical properties. Modern FE models provide some insight on the variables that control this variation, however, material characterisations remain determined from small-scale experimental simulations and/or the destructive testing of component test coupons following full-scale manufacture. The HTS can be used to accelerate the validation process because characterisation of both microstructure and mechanical properties can be obtained from individual test specimens, and this permits through thickness characterisation of properties without the need to manufacture full-scale component test coupons.

The following chapter presents the testing of this new experimental method of validating heat treatments for large forgings, by using the

HTS to predict both the final microstructure and mechanical properties in large forgings following heat treatment. Firstly, the calibrated HTS dilatation data attained for 20MND5 in Chapter 4, is analysed. This is used to characterise transformation temperatures and volume fractions of transformation products for continuous cooling conditions. This characterisation is used to predict microstructure evolution in a real forging by simulating a temperature profile recorded from a thermocouple embedded at the half thickness of a large tubesheet forging during agitated water quenching at SFIL. The forging profile is then tested using 20MND5 specimens, using both the HTS and by small scale dilatometry and the results are compared to validate the testing using the HTS. The validation gives confidence in the mechanical testing of the HTS specimens, and the combined result shows that full characterisations of large forgings following the quenching process can be achieved using the HTS.

5.1.1   Theoretical considerations

The data gathered in Chapter 4 was analysed to generate a characterisation of transformation temperatures and volume fractions, from which predictions could be made. The methods of analysis are discussed in the following pages.

5.1.1.1   Transformation temperatures

When a metallic material undergoes a transformation of one phase to another, the crystal structure of the material is rearranged to minimise the total energy of the system for a specific temperature and pressure. This is quantified as a change in Gibbs free energy [68]. During the change of crystal structure the material also undergoes a change of specific volume, and this change is quantifiable using a dilatometer [89]. Dilatometers measure these changes in a single dimension, as previously discussed, and the measurement of dilatation in a single

dimension can be used to characterise transformation events occurring during heat transfer. Figure 38 shows the dilatation curve, recorded for a low alloy steel that was cooled continuously at a rate of 10°C/min. In this figure, the measured dilatation of the specimen is normalised by dividing gauge length to yield thermal strain (dL/Lo), and plotted against temperature.
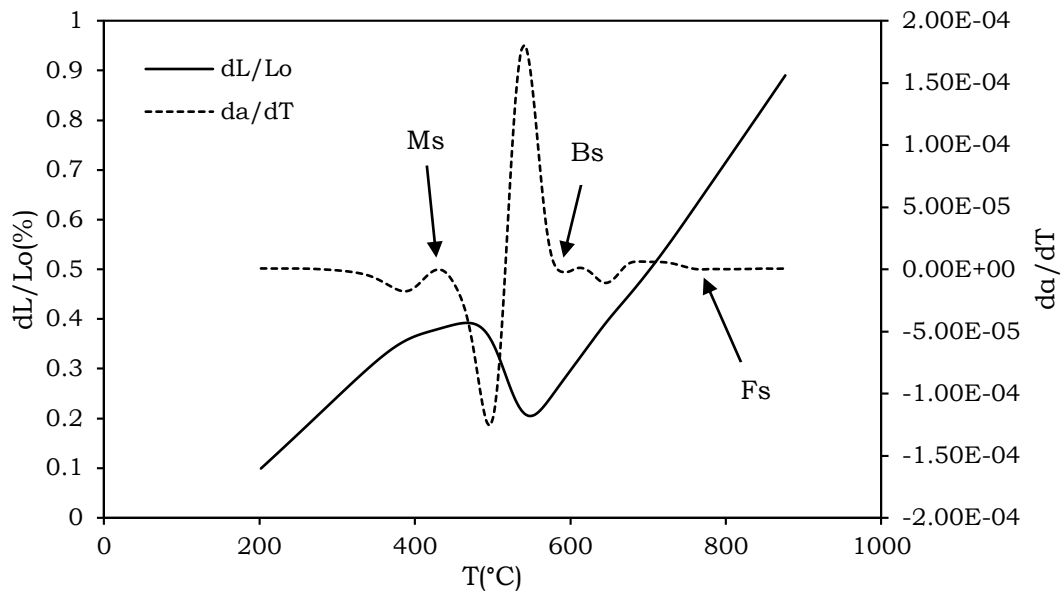
Figure 38: The recorded dilatation of a low alloy steel during continuous cooling at 10°Cmin^{-1}, and its second derivative of dilatation with respect to temperature.

With a stable microstructure, the thermal strain of metallic elements closely approximates a linear relationship with respect to temperature, however, when a transformation occurs the materials expansion characteristics deviate due to the change of crystal structure, and often, the liberation of latent heat.

Transformation temperatures are defined as the first deviation from the linearity of the dilatation plot [90], however, small volumes of transformed material do not cause large deviations of linearity, making it difficult to ascertain accurate transformation temperatures. This is seen at the start of the ferrite transformation (Fs) indicated in Figure

132

38. In open literature there have been some different methods developed that can be used to determine transformation temperatures from dilatometric data [36,47,91,92]. However, in this work, a simple method of differentiation has been used.

As previously defined, the gradient of the dL/Lo plot is known as the true coefficient of thermal expansion (α_T) which may be written for any point on the dilatation plot as:

$$\alpha_T = \frac{d}{dT}\left(\frac{dL}{Lo}\right) \tag{4}$$

During linear expansion, α_T is constant and therefore the derivative of α_T with respect to temperature is zero, and is not zero during transformations of microstructure. Transformation temperatures can therefore be easily observed as deviations from zero on a plot of $d\alpha_T/dT$ against T from the condition:

$$\frac{d\alpha_T}{dT} \neq 0; \quad when; \frac{dL}{Lo} \neq AT + B \tag{14}$$

This is highlighted in Figure 38, which shows a clear deviation from zero in the dα/dT when almost no clear deviation from linearity is seen in the dL/Lo plot at the same temperature.

When a number of cooling rates have been tested, the transformation temperatures for specific events can be plotted as a locus of points on a plot of temperature against time to form a CCT, and is a characteristic diagram of the material transformation kinetics under continuous cooling conditions. The CCT is separated by the loci into a

number of identifiable phase fields, and can be used to infer microstructure evolution for intermediate cooling rates.

5.1.1.2 Volume fractions

The dilatation plot can also be used to quantify the volume fractions of transformed material. This was first formulated and tested by Fisher and Geils [93]. The method permits the quantitative determination of transformed material on the assumption that both the initial microstructure and the transformation product have cubic crystal structures. It is therefore a universal equation and has the form of the common lever rule, Figure 39.
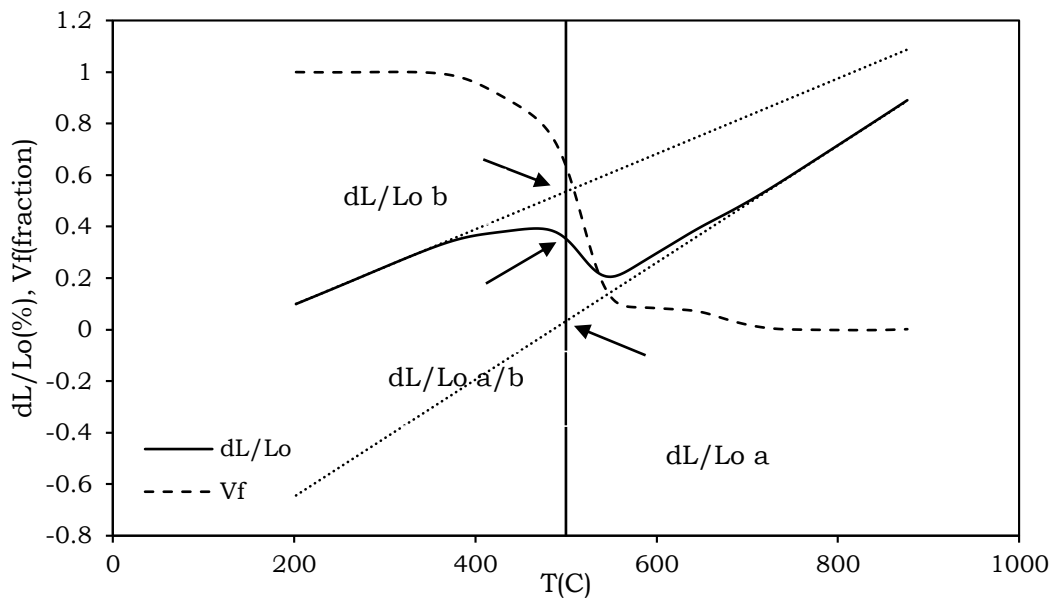
Figure 39: The recorded dilatation of a low alloy steel cooled at 10°C/min, and the volume fraction (Vf) curve calculated from it using Fishers' lever rule formulation.

As previously discussed, the thermal expansion characteristics of a material deviate from linearity during transformation events and thus delineate the region within the CCT diagram where phase transformation is occurring. To determine the magnitude of the transformation event characterised by the delineation, the linear

134

sections of the dilatation plot before and after transformation are extrapolated through the entire temperature range of the test, Figure 39. For any temperature, a ratio of the differences between the extrapolated dilatation and the measured dilatation yields a fraction that represents the volume of transformed material at that temperature.

$$Vf = \frac{(dL/Lo)_{a/b} - (dL/Lo)_a}{(dL/Lo)_b - (dL/Lo)_a}$$ (15)

With a knowledge of specific transformation temperatures, specific volume fractions can be determined. These can be plotted as a locus of points in a plot of volume fraction against cooling rate, to yield a characteristic diagram for the material. From this diagram, the volume of transformed material as a function of cooling rate can be inferred, allowing predictions to be made.

5.2   EXPERIMENTAL

The objectives of the work required a number of experimental procedures to be completed. Firstly, the characterisation of 20MND5 was needed to construct both a CCT diagram, and a characteristic volume fraction diagram from which predictions could be made. Following predictions, it was necessary to test the material by simulating a thermal profile taken from a forging during quenching using the HTS and small scale dilatometry, validate the result by comparison of microstructure and hardness testing, and test the HTS specimens for mechanical properties.

5.2.1   Further characterisation of 20MND5

The data required to characterise 20MND5 was obtained during the testing completed in Chapter 4. The dilatation data recorded during those tests was smoothed using a LOESS quadratic regression filter that reduced noise levels and allowed clear differentiation to be completed. The critical temperatures were determined from second order derivatives of dilatation with respect to temperature, using the method discussed in section 5.1.1.1. The transformation temperatures were plotted as a locus of data points for each cooling rate to form a CCT diagram for the material. This is shown in Figure 40.
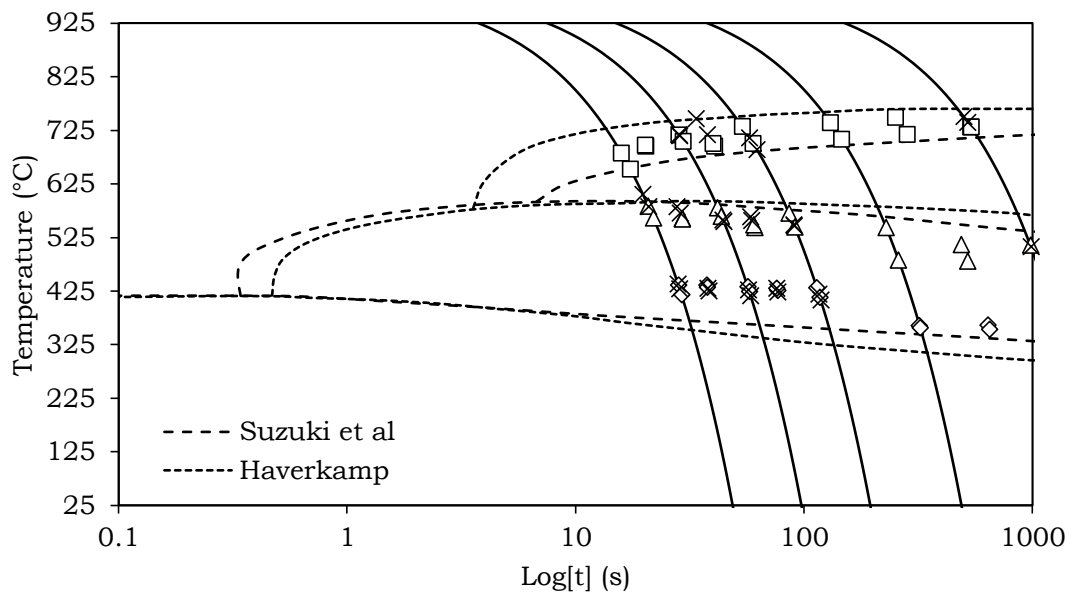
Figure 40: The CCT diagram for 20MND5 calculated from repeated measurements using the HTS and a Netzsch 402C differential dilatometer. The material was tested four times per cooling rate, twice using the HTS, and twice on using Netzsch dilatometer. Two further two CCT's are shown for comparison. These were published were for 20MND5 by Haverkamp et el [44], K Suzuki [94].

With critical temperatures known, stable volume fractions of fully transformed material at room temperature (RT) can be ascertained; if it is assumed that no further ferrite can be transformed upon the onset of the Bainite transformation, then the volume fraction of ferrite at the Bainite start temperature must approximate the stable RT ferrite

136

volume fraction. Similarly, the martensite volume fraction can be determined from the Bainite finish temperature, and the Bainite volume fraction from the difference. The Bainite start and finish temperatures were then used to calculate the volume fractions for each cooling rate tested, from the lever rule formulation discussed in section 5.1.1.2. The calculated volume fractions for all tests were plotted against cooling rate to form the characteristic volume fraction diagram. The plots were then fitted with appropriate equations using the software Origin Pro 9.1, which allowed volume fractions to be calculated for intermediate cooling rates. The characteristic volume fraction diagram is shown in Figure 41:

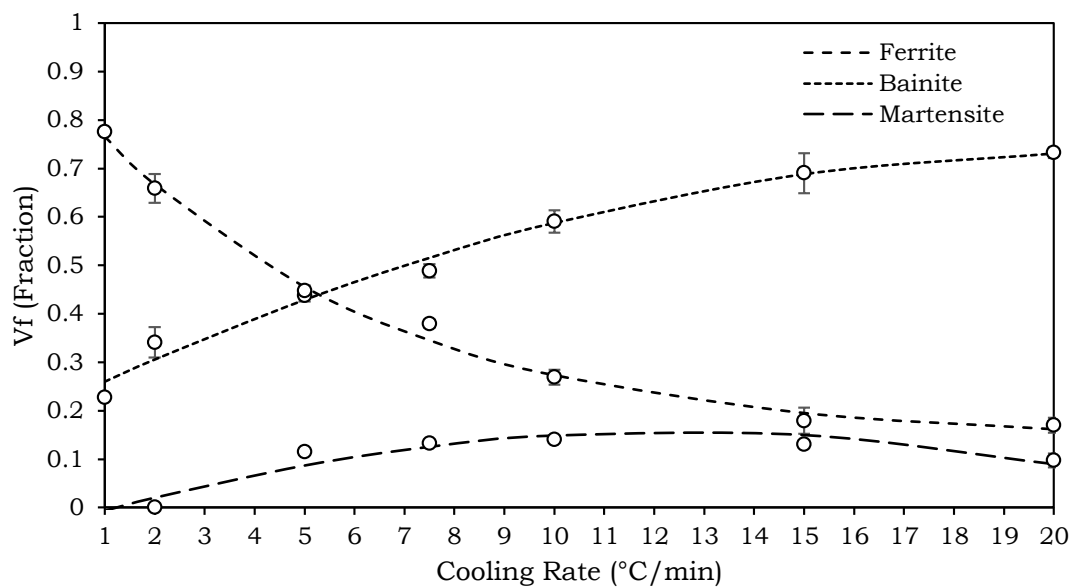Figure 41: The characteristic volume fractions of transformed material in 20MND5, as a function of cooling rate. Uncertainty was calculated in 95% confidence.

5.2.2   Simulation

5.2.2.1   The forging profile

20MND5 is a material that releases latent heat when undergoing transformation on cooling. When this occurs, the latent energy liberated transfers into the bulk and retards the local cooling rate. This

influences the transformation kinetics. The effect of latent energy on transformation kinetics is a phenomenon known as recalescence, and is a topic which has been discussed in open literature [70,95]. In large forgings, the effect of recalescence can be significant because large quantities of latent heat are released. This is due to the large volumes of transforming material, and the large distances required for conduction controlled dissipation of the heat through the forging. In small-scale simulations, these factors are often considered negligible, as the thermal masses and conduction distances are much smaller. Latent heat is however, released during transformations, and this presents a problem with simulating thermal profiles: If a small-scale simulator simulates the latent heat released in a large forging during transformation, a supposition of latent energies must occur causing the simulation to be inaccurate. If the latent energy of the forging were ignored, the true effect of recalescence on transformation characteristics of the forging would not be simulated. Thus, to simulate accurately the thermal profiles of forgings, it is necessary to investigate the effect of simulating thermal profiles both with and without the presence of latent heat.

The forging profile simulated in this work was recorded at the half thickness a 315mm thick tube sheet forging during agitated water quenching, and contains significant quantities of latent heat. The recorded temperature profile possessed a very large number of fractional co-ordinates. To conform to the programming limitations of the HTS and small-scale dilatometry, the recorded data was interpolated using Origin Pro 9.1, and rounded to plot coordinates with integer values. The latent heat was then removed from this profile to produce a comparative profile from which the effect of latent heat could be evaluated. The resulting profiles for simulation are shown in Figure 42.

The forging from which the profile was recorded was made from the PV material SA508 Gr.3 Cl.1; an alloy of very similar chemistry to the 20MND5 alloy used for the forging profile simulations. This similarity of composition was shown in section 4.1.4. It was therefore assumed that the transformations, and hence latent energies, would occur at similar temperatures and magnitudes for both 20MND5 and the forging profile. Accurate predictions and representative test results would then be attained from testing the forging profile using 20MND5 specimens. 20MND5 specimens were prepared and tested for both forging profiles, with and without latent heat, using both the HTS and small-scale dilatometer.
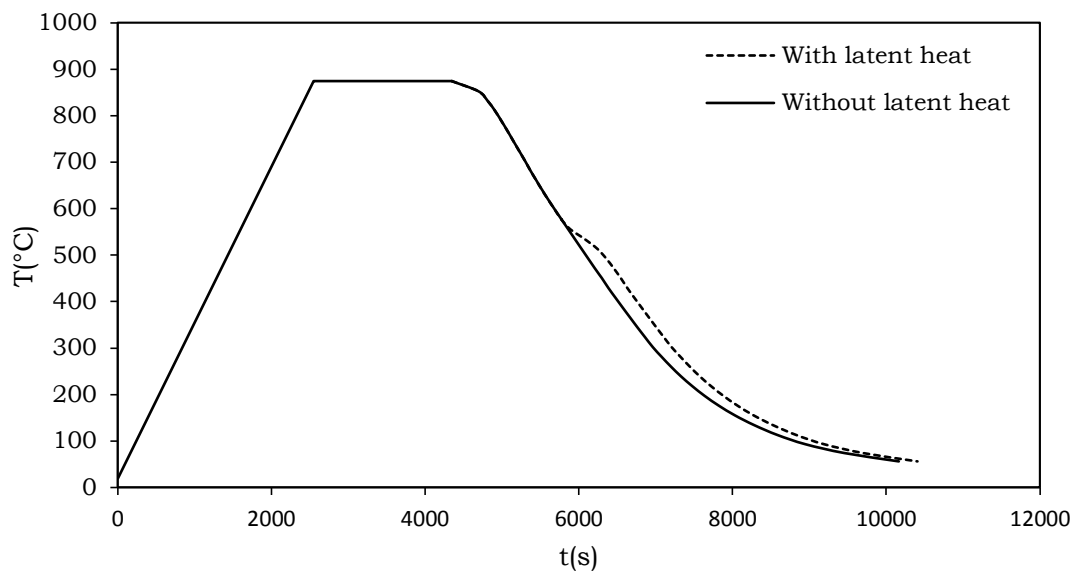
Figure 42: The thermal profile used for simulation. The profile was recorded at the half thickness of a 315mm thick forging during quenching.

5.2.2.2 *Testing and analysis*

The simulation of the forging profile was performed using the HTS and a small-scale scientific dilatometer. The small-scale dilatometer used in this work was a Baehr DIL805. The Baehr DIL805 is a differential dilatometer that employs an in-situ, vitreous silica standard reference specimen. The specimens' dilatation during testing is transferred by a

139

vitreous silica push rod to a LVDT, and measured concurrently with the reference specimen during testing. In similarity to the HTS, the Baehr heats the specimen by an induction coil and employs forced inert gas quenching to track temperature accurately throughout each program. During the Baehr simulations, helium was used as the inert gas coolant.

The specimens for the Baehr DIL805 were 4mm diameter and 10 mm gauge length and two specimens were made and tested. Each experiment was controlled by an S-type thermocouple spot-welded to the surface at the longitudinal centre of each specimen. This system and the testing procedure conformed with ASTM standards for dilatometry [65].

The HTS specimens and experimental setup for this work were as described in previous chapters. Two HTS specimens were made from 20MND5 for this work and were tested with active forced air quenching to simulate the forging profile accurately.

Following testing, validation of the HTS was completed by comparing the results of microstructure and hardness testing with the Baehr DIL805 specimens. Microstructure was evaluated using a Nikon Eclipse LV150 bright field microscope following etching of the specimens in a 4% alcoholic nitric acid solution. Hardness tested was completed using a Struers Durascan micro-hardness indenting machine measuring the Vickers hardness at 1KgF [96].

Following validation, the HTS specimens were mechanically tested by tensile, and Charpy impact testing. The mechanical testing was completed in SFIL using a Zwick-Roell tensile testing machine at a strain rate of 0.015/min, and a Zwick-Roel Charpy impact testing

machine. The testing was completed at room temperature (RT) and to ASTM standards [97,98], as this temperature aligned the mechanical data to the RT condition of CCT diagram. This allowed the material properties as a function of the simulated heat treatments to be determined with confidence, showing that the HTS can be used to characterise through thickness property variation in large forgings fully.

5.3   RESULTS

5.3.1   Predictions and volume fractions

To predict microstructure evolution of 20MND5 when tested, it was necessary to determine critical temperatures for the forging profile for each transformation. Cooling rates could then be calculated and compared with the characteristic volume fraction diagram in Figure 41, to form a prediction. To determine critical temperatures, the thermal profile was plotted on the CCT diagram developed for 20MND5 and critical temperatures were taken as the intercept of the profile and the loci of start temperatures for each transformation field of the CCT.

The driving force for each transformation is the temperature difference between AC_3 and the critical temperature for that transformation, however, if recalescence occurs after the transformation start, the cooling rate is slowed reducing the driving force for continued transformation and retarding the kinetics. The method of prediction outlined requires a cooling rate to be defined; however, the effect of recalescence is that the cooling rate varies continuously through transformations, as seen in Figure 42. It is therefore applicable to investigate the boundaries to the transformation kinetics as an indication of accuracy in the results of the tested specimens: If the cooling rate is only slowed by recalescence then an average cooling rate

calculated from Ac_3 to the transformation finish temperatures must predict the smallest effect of recalescence on microstructure evolution. However, if the transformation kinetics are wholly controlled by recalescence, then the local cooling rate between the start and finish of each transformation must predict the greatest effect of recalescence. With cooling rates calculated, the volume fractions of transformation products could be determined in series. Firstly, the ferrite fraction, then bainite, with the martensite fraction taking the value of the remaining untransformed austenite. The results of the predictions made, both with and without the inclusion of latent heat, are shown in Figure 43.

The predictions indicate that the effect of latent heat on the ferrite transformation is 0%. This is thought to be because the kinetics of ferrite are slow due to diffusion-controlled growth. The latent energy released can therefore be dissipated in this forging, and is not present in the forging profile. In addition, the volume fraction of ferrite is small for the cooling rates recorded in the forging through the ferrite transformation range, and so less is produced and less latent energy is liberated. The bainite transformation however, is greatly affected by the presence of latent heat for both predictions made. As a displacive transformation the kinetics of bainite are far more rapid, and initial transformation liberates significant quantities of latent heat. The effect of this liberated energy is to slow the transformation kinetics and reduce the volume fraction of bainite, however, since the ferrite transformation has ended and less bainite is produced, the remaining austenite must transform to martensite. The predictions imply that for this thermal profile and hence this forging, the effect of the latent energy released during the bainite transformation is to make 20MND5 more hardenable.
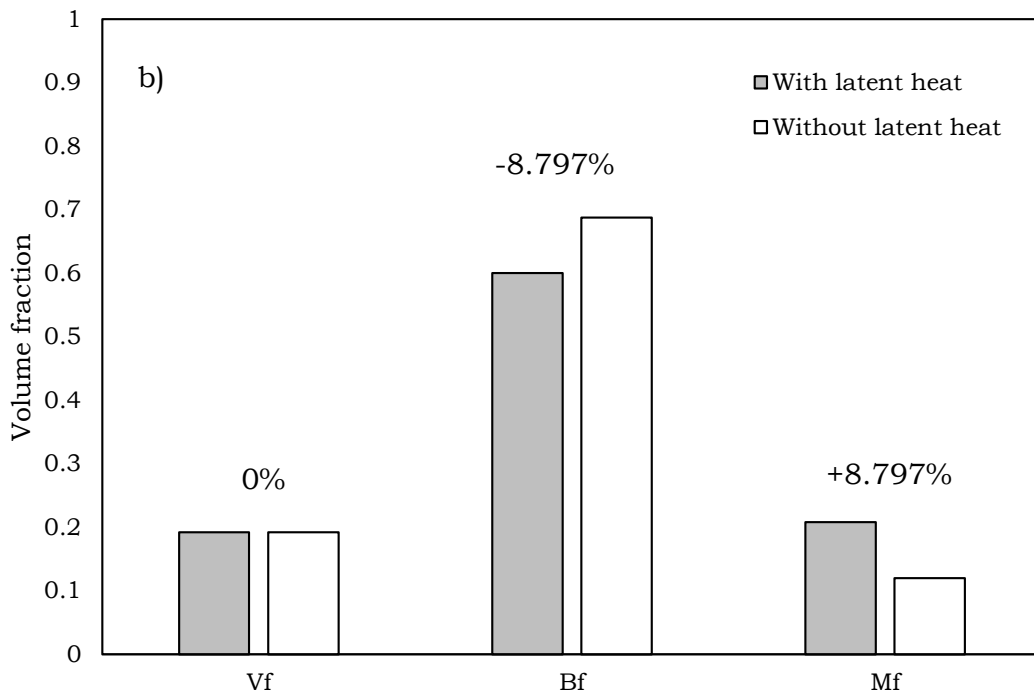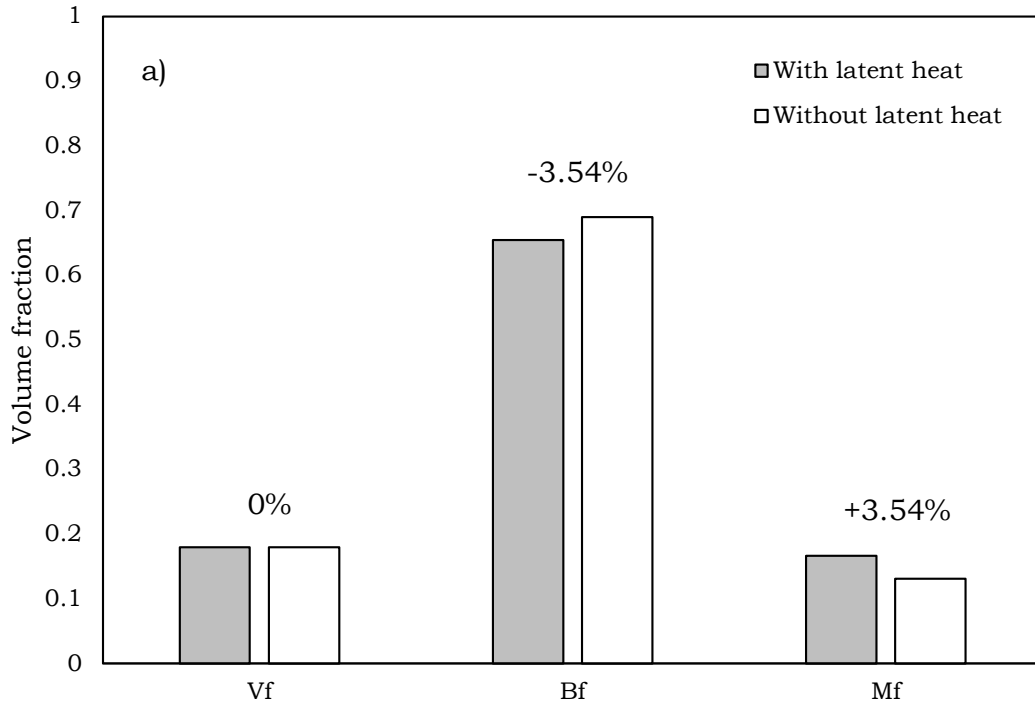
Figure 43: The predicated volume fractions of transformed microstructure for 20MND5. a) The cooling rate used was an average between AC_3 and the transformation end temperature. b) The cooling rate used was local to the transformation start and end temperatures.

The results of testing the profile using the HTS and Baehr dilatometers, both with and without latent heat, are plotted in Figure 44. The results show trends which correlate with the predictions in Figure 43; the effect of latent heat within the tested thermal profile and hence the forging, is to increase hardenability by reducing the bainite fraction, and increasing the martensite fraction. This correlation positively indicates that the HTS is able to simulate thermal profiles accurately; however, there are differences between the predictions and test results. For example, the effect of latent heat on microstructure in the Baehr tests, is within the boundaries of the predictions made and indicates a successful simulation, however, the difference in the fractions calculated for the HTS data are greater in comparison, with the bainite fraction being greater than the upper boundary of the predictions.

This is thought to be because of temperature gradients during testing. During testing, the HTS specimens are cooled by a forced air quenching system, which simultaneously with the provision of heat, acts to track the specimen cooling-rate in accordance with the forging profile. Internally, however, heat must be transferred to the surface by conduction before being dissipated. Conduction is less efficient than convection [83,99], and so potential exists for temperature gradients to develop during testing of the HTS specimens. The greatest effect of this will likely occur at the corners of the specimen as the increased surface area leads to increased heat loss. This was shown in the testing of Chapter 3, and therefore temperature gradients do occur in the HTS specimens both radially and longitudinally.

Transformation temperatures are calculated from thermal expansion as previously discussed, and any temperature variation is measured in this quantity. Because of this, greater volumes of transformed material are recorded for higher transformation temperatures if heat loss due to end effects is present; in the specimens tested by the HTS,

the temperature of the sample is measured halfway along its gauge length using a surface thermocouple. End effects present during testing mean that transformation is occurring at the ends of the sample prior to the bulk of the sample, and is recorded as dilatation, thus the recorded temperature associated with the transformation is marginally higher than the actual temperature of the transforming material.

The transformation temperatures are used to determine volume fractions from Fishers formulation (section 5.1.1.2). When evaluating increases in transformation temperature using the example in Figure 39, the reason for the larger difference in transformation fractions in the HTS specimens can be seen: If the transformation temperatures are higher, then for continuous cooling the ferrite fraction is reduced, the martensite fraction is increased, the bainite fraction being calculated from the difference. The simulation without latent heat may be approximated in this way, however, for the simulation with latent heat, more martensite is produced by retardation of bainite, and if the ferrite fraction is also reduced by temperature inhomogeneity, the effect of latent heat on bainite becomes bigger by calculation.

However, the differences between the predictions and HTS results are small, implying good temperature homogeneity through the thickness and along the length of the large specimens. When comparing the absolute volume fractions of each phase for each test, it is noted that HTS fractions are more similar to the predicted volume fractions in both HTS tests too, and this strongly indicates that a large volume of the specimen material is representative of the imposed thermal profile.
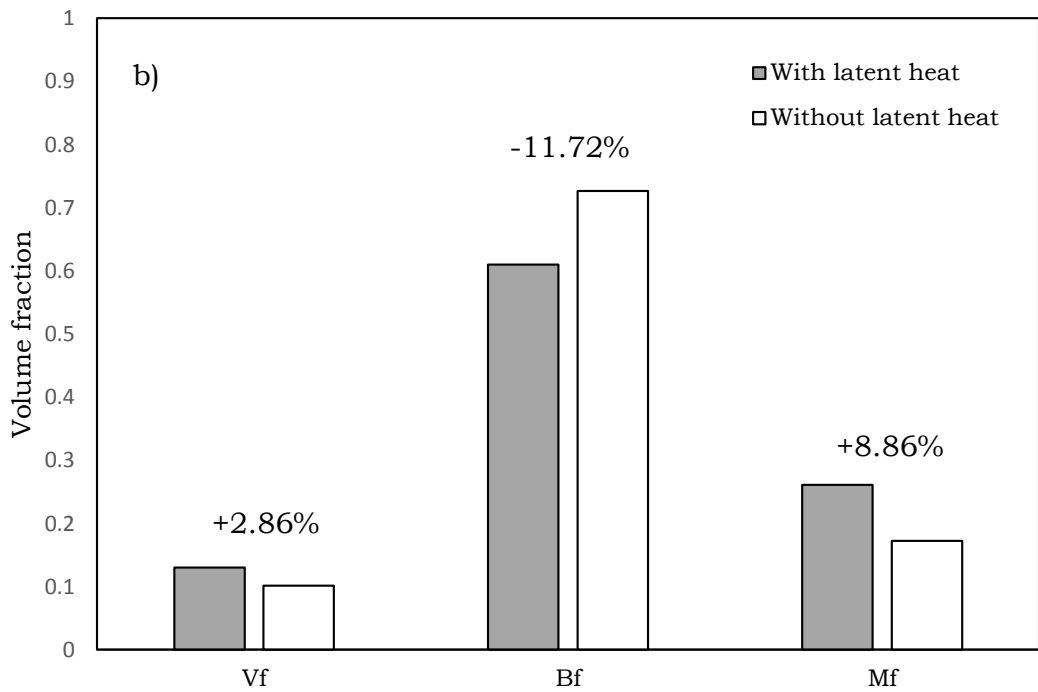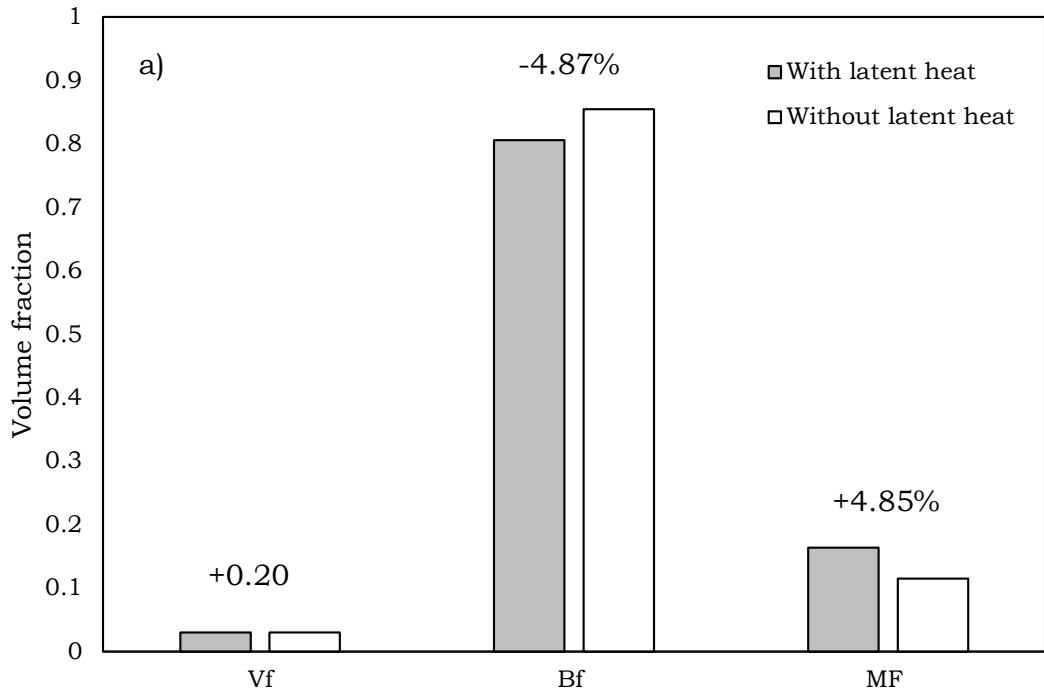
Figure 44: The volume fractions of transformed microstructure for 20MND5 tested for the forging profile both with and without latent heat, using, a) the Baehr DIL805 and b) the Heat Treatment Simulator.

5.3.2 Microscopy and hardness

The results and discussions in the last section indicate that a large volume of the HTS specimens is representative of the imposed thermal profile. Confirmation of this remains needed to have confidence that the HTS can simulate complex forging profiles, such that the mechanical testing of the HTS specimens is representative of that forging profile too. It is necessary then to analyse the microstructure of the specimens.

In Figure 45 the micrographs of the specimens at 50x optical magnification are displayed. The initial comparison of microstructure between the HTS and Baehr specimen micrographs show similarity both with and without latent heat, indicating accuracy in HTS simulation of the forging profile; the simulation of the forging profile has produced largely bainitic microstructures with low volumes of ferrite in all tests. To confirm, the micrographs were analysed by point counting. What was found was that the ferrite fractions of the HTS specimens, with and without latent heat were 14.5% and 14.9 % respectively. The similarity supports the volume fractions quantified in section 5.3.1, and confirms that the difference calculated in the ferrite fraction of the HTS specimens was due to errors in calculation caused by temperature inhomogeneity. In the Baehr micrographs, ferrite was not observable in the microstructure, supporting the results of that testing too. Martensite however, could not be distinguished in any of the micrographs taken, and therefore no difference could not be determined between the tests with and without latent heat, for each test method. Since the volume fraction analysis indicates that the material becomes more hardenable by the liberation of latent heat, and that martensite cannot be distinguished from the micrographs in Figure 45, it is appropriate to test for hardness, to confirm the effect of latent heat. These results are given in Table 7.

	With	Without
HTS		
Baehr		
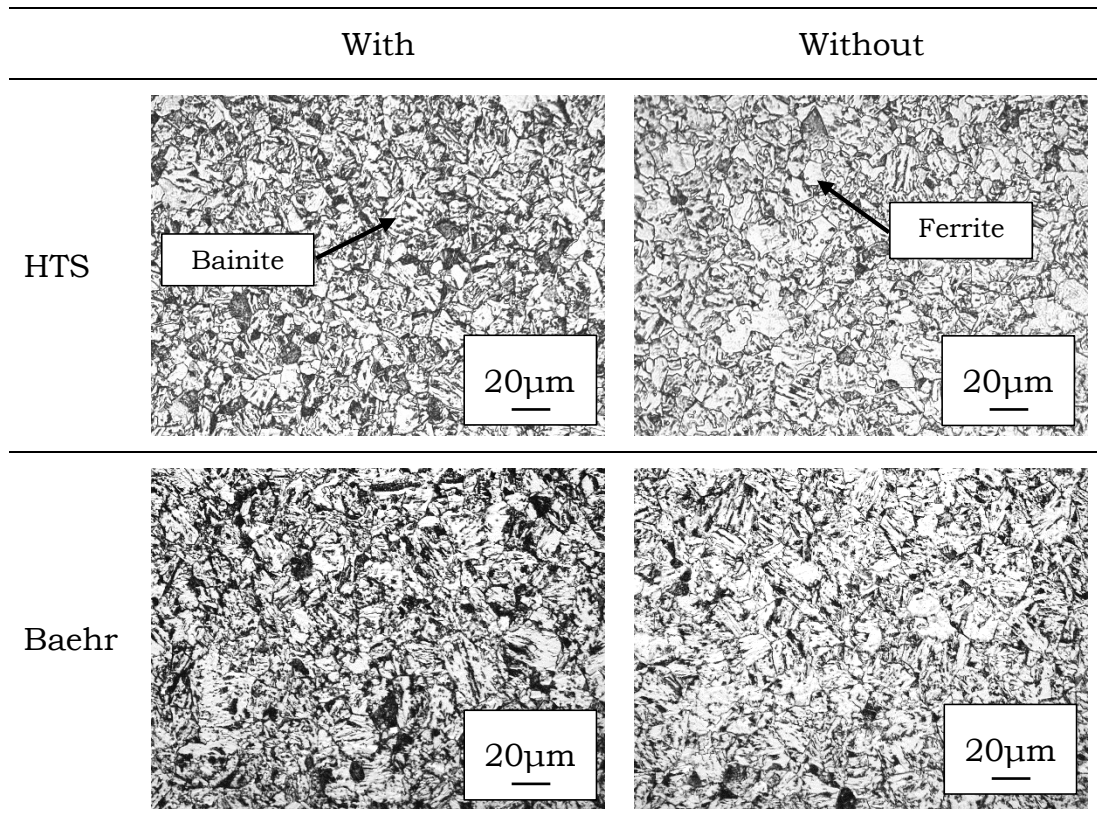
Figure 45: Microstructure of 20MND5 tested by the HTS and Baehr DIL805 for the forging profile, both with and without latent heat.

Table 7: The Vickers hardness number (HV) of the microstructures presented above. These are reported here with a confidence limit of 95% (K=2)

	With latent heat	Without latent heat
HTS	255.50 ±2.29	255.94 ±3.58
Baehr	262.50 ±4.02	260.42 ±3.13

The result shows that the hardness of the Baehr specimens becomes greater with the inclusion of latent heat, indicating an increase in the martensite volume fraction, and supporting the increased hardenability predicted, however, the hardness values of the HTS specimens are almost identical to each other, despite the volume fraction analysis following the trend of hardenability. This can be explained by considering the value of each indentation and the increase of martensite sought for detection.

The hardness value of each indentation represents an average of the local microstructure for each indentation. Good practice is to choose an indenting force that yields indentations much larger than the average grain diameter; this reduces scatter, and therefore reduces uncertainty. For the forging profile tested in this work, a negligible change in volume of ferrite was confirmed by point counting, and therefore any change of hardness is due to martensite alone. The predicted change in martensite was between 3.54% and 8.80%. The Baehr specimens produce a change of 4.87%, which is low in the predicted range. The change of hardness in respect was only 2.08HV, with the calculated uncertainty being greater than this value. For the HTS, the ferrite volume fraction was confirmed to be greater than the Baehr specimens were, and so it follows that the hardness measured is lower, however, the change of ferrite was shown to be negligible by point counting, confirming the error in calculating the volume fractions from the HTS test data. Complimentary to this, the calculated change in the martensite fraction also contains that error too, and is therefore likely to be smaller.

Since the change of martensite is likely to be small and the uncertainty is of the same scale despite best practice being followed, it becomes very difficult to detect the change of martensite fraction for this forging profile from hardness testing. However, the hardness result for the HTS specimens does confirm the discussions of error made in section 5.3.1, and supports that the ferrite volume fraction is similar to the predicted volume, and this adds to the confidence gathered in the HTS to simulate forging profiles accurately.

5.3.3   Mechanical properties

The volume fraction calculations given in section 5.3.1 confirm the general behaviour of 20MND5 for the temperature profile both with

and without latent heat, showing that the consequence of latent heat is to increase the quantity of martensite by retarding the Bainite transformation. An investigation of microstructure has supported the discussions made, and confidence is possessed that the HTS can accurately simulate complex thermal profiles. The mechanical testing of the HTS specimens is therefore considered representative of the forging profile, and results of this testing are shown in Figure 46.

The results show that the consequence of the latent heat liberated in the forging during quenching is to decrease the 0.2% proof strength, increase the ultimate tensile strength, and reduce impact toughness. Since the change of ferrite in the HTS specimens is shown to be negligible, the reason for changes in mechanical properties is due to the retardation of bainite, and the increase of martensite fraction, as the consequence of the latent heat released during the Bainite transformation.

Martensite is a displacive transformation that occurs by shear of the crystal lattice. This produces a transformed microstructure with high dislocation density that is very strong but very brittle, and therefore its presence in the microstructure has a direct effect on mechanical properties of the material. The effect of latent heat released in the forging was shown to increase the quantity of martensite, and therefore to increase the dislocation density of the microstructure. The UTS is a property that is functional to dislocation density as the movement of dislocations is necessary for plastic deformation. If the dislocation density is increased, it follows that the UTS will increase in respect. This is observed in Figure 46. Similarly, an increased dislocation density will reduce ductility, as higher density will reduce the movement of the dislocations by entanglement. This means a lower absorption of energy under loading and so it is expected that the

impact toughness should reduce with the liberation of latent heat in the forging. This is also seen in Figure 46.
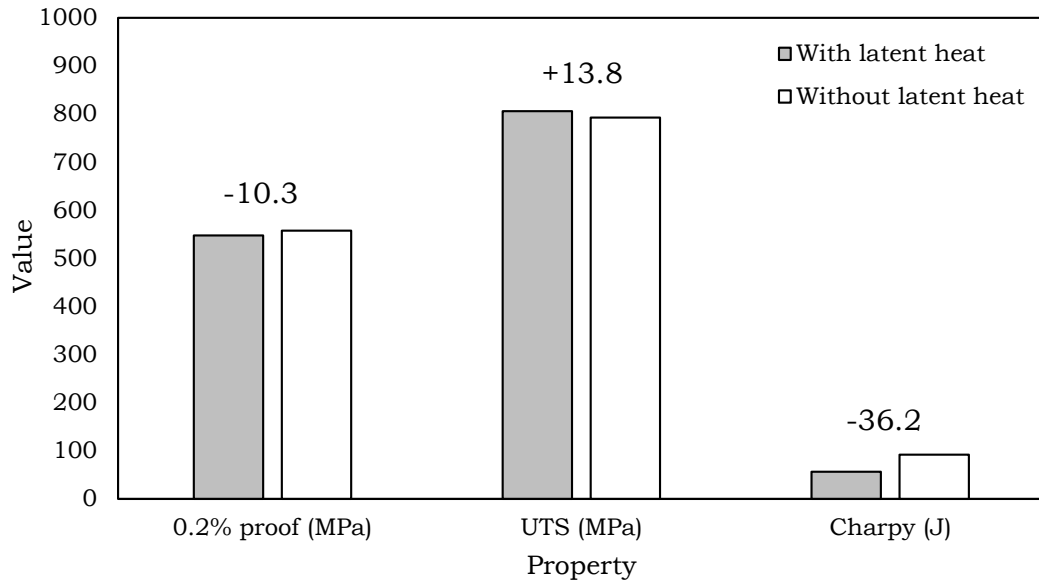

Figure 46: The difference in mechanical properties by testing 20MND5 for the temperature profile both with and without latent heat.

The proof stress however decreases with increased volumes of martensite. The reason for this is that yielding does not occur in the martensite. Since martensite has increased strength, yielding is most likely occur in the bainite. In the experiments conducted here dislocation density of bainite is unlikely to change, however, the retarded transformation kinetics caused by the inclusion of latent heat allows further diffusion of carbon from the microstructure. This relaxes the strain field in the lattice and allows dislocations to move more easily, the result is that the proof strength is reduced as is observed in Figure 46.

5.4   DISCUSSION

The aim of this work was to fully characterise the microstructure evolution of 20MND5 at the centre of a thick forging, by simulating the

thermal evolution of that location using the HTS. Prediction and control experiments were used to validate the testing, and the results positively indicated a successful characterisation, however there are some discontinuities in the results, and limitations in the work, which remain to be discussed.

5.4.1 The Baehr volume fractions

In the volume fraction results presented, it was noted that the absolute volume fractions of the forging simulations, with and without latent heat, were more similar to the predictions when tested by the HTS. The Baehr results predicted ferrite fractions that were notably smaller, and Bainite fractions that were notably greater. This is thought to be due to uncertainty of measurement.

It was discussed in section 5.1.1.1 that small volumes of transformed material do not cause great deviation of linearity in the dilatation of specimens, and since the volume fraction is calculated from this measurement, it follows that inaccuracy of measurement must contribute too. The Baehr DIL805 measures dilatation by the displacement of an LVDT and measures changes of length with a uniform uncertainty of ±0.5µm/°C. However, using a published CTE for ferrite [100], the change in length due to transformation within the Baehr specimens is approximated to be in the order of 12nm/°C. The measurement uncertainty is very large when compared to the accuracy of measurement required and while this error becomes small when large volumes are transformed, is significant when the transformation volumes are small. For the thermal program tested here the volume of ferrite remains small and must therefore contain a significant measure of uncertainty, and through calculation, this inaccuracy must sum with the next transformation in series, therefore, the bainite volume fraction becomes bigger as a consequence of this inaccuracy.

5.4.2   Limitations of the work

In this work, the experiments were designed towards testing the new experimental assessment method. The results attained for the forging profile were very positive of success, however, the specificity of experiment design meant the effects of some variables were not investigated and for different experiment parameters, may limit the success of the new method. These must be discussed.

5.4.2.1   New materials and new components

In this work, the forging profile selected for testing came from a forging of similar chemistry to the test material. This meant that the latent heat released within the profile occurred at a similar location in the profile to the test material, and that the test material would release similar magnitudes of latent heat relative to the forging. However, for less similar materials, latent heats released will occur at different locations, and have different relative magnitudes. This limits the application of the method when investigating the suitability of new materials in existing applications, as existing profiles will not be representative of their thermal evolution.

One way to develop the method for new materials is to use FE models to predict thermal evolution in forgings during heat treatment. Figure 47 is shows the hardness testing of a FE generated profile developed by Howson et al. [101], which was tested using the Baehr DIL805 for three different forging materials. This has been plotted in comparison to the forging profile (FO) tested in this work for the same materials. The FE profile is much slower than the FO profile and the results indicate that between these forgings, the microstructure of alloy SA508 Gr.4N does not greatly change. The microstructures of both 20MND5 and SA508 Gr.3 notably changed, with the latter having greater scatter, indicating inhomogeneity of microstructure also. This implies

that for each forging, the best material to use would be SA508 Gr.4N; however, both thermal profiles were developed for SA508 Gr.3. The chemistry of SA508 Gr.4N makes it a more hardenable alloy, and therefore the liberation of latent heat will not correlate with the imposed thermal program. In addition, their model was an attempt to model profiles recorded from a real SA508 Gr.3 Cl.1 forging; however, the FE model was unable to match that forging profile exactly. This shows that there were limitations within that model, which they discussed in their work, and these limitations raise questions as to the validity of the simulating FE modelled profiles that represent the thermal evolution of real forgings.

Despite this, the HTS has been shown as an accurate tool in the new method of predicting property variation in large forgings presented in this chapter, and with continued developments in FE modelled thermal profiles of large forgings, the HTS will remain the tool required in the new method when developing new materials and component also.
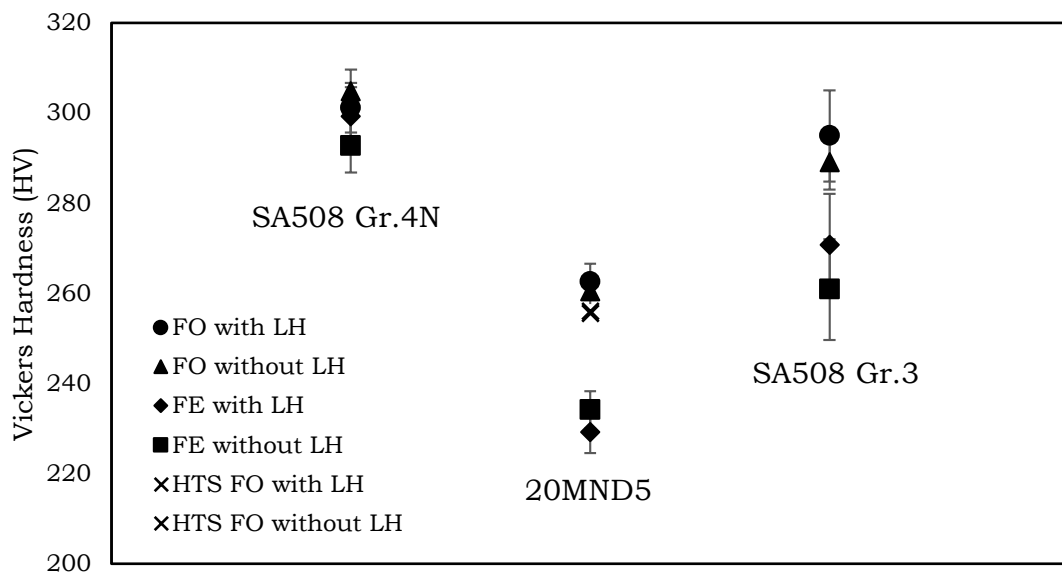

Figure 47: The hardness testing of three PV materials for two different thermal profiles, both with and without latent heat. FO profile is the forging profile used in the work, the FE profile is a profile generated by FE modelling of a 1m thick component under quenching.

5.4.2.2 Material characterisations

The method of prediction used in this work required a characterisation of the material to be tested. This characterisation gave transformation temperatures and cooling rates that were compared to a characteristic volume fraction diagram to make a prediction. The method was shown here to perform accurately on a basic level however; prediction in this way contains error, and has limiting effect to the development of the new method.

In Figure 40 was shown the two published CCT diagrams for 20MND5. The transformation temperatures determined in this work correlated well with this work and so predictions were made in respect, however there are differences between these critical temperatures. In this work, the transformation temperatures of the forging profile were taken as the average with respect to the 20MND5 characterisation. Since averages were used and that these differed from literature, it follows that there is error within in each calculation using those temperatures; hence, the predictions of volume fraction must contain this error too. This indicates a limitation to the development of the new method; if characterisations are required to validate HTS testing, it follows that each material tested requires a CCT and volume fraction diagram. However, as seen in Figure 40, existing characterisations differ, and do not have volume fractions of transformation products, microstructure, or mechanical property information. This implies that for the new method to be industrially useful, material characterisations are needed for each material tested, and this slows analysis by the new method.

The HTS can be used to complete these tasks, as materials can be fully characterised from each specimen, and given that application of the new method will result in further characterisations, a data base will be

generated which will benefit industry by being up to date and more relevant than the historical data bases and small scale researches currently available.

5.5   SUMMARY

The aim of this work was to test a new method of predicting property variation in large forgings, only possible using the HTS. The method allowed the testing of mechanical properties in addition to microstructure and hardness, yielding a full material characterisation following heat treatment. The HTS was found to be accurate for this purpose. A forging profile was simulated and the effect of latent heat in that profile was investigated. The work was validated using predictions and by small scale, control experiments and the contributions to error were identified and discussed. The findings of this work are summarised below:

1.   A characterisation of the alloy 20MND5 has been made which contains both a CCT diagram and characteristic volume fraction diagram. Predictions were made from the characterisation and the test results to confirm their accuracy.

2.   A forging profile was simulated using the HTS, and the volume fractions of transformed material in the HTS specimens correlate with predictions. Errors have been identified and discussed.

3.   The effect of latent heat in this forging was investigated, by volume fraction analysis, microstructure investigation and hardness testing. The effect of latent heat was found to make the material more hardenable.

156

4. Specimens were tested by tensile and impact testing. The increase of hardenability due to latent heat was shown to decrease the 0.2 proof stress, increase the UTS and decrease impact toughness.

6 MICROSTRUCTURE AND MECHANICAL PROPERTY EVOLUTION OF SA508 GR.3 Cl.1 UNDER CONTINUOUS COOLING CONDITIONS

6.1 INTRODUCTION

SA508 Grade 3 Class 1 is a low alloy forging steel specified by the ASME for the manufacture of pressure vessels (PVs) [42]. A PV, as a safety critical and life-limiting component, must possess a unique combination of mechanical properties. This has led to much research being conducted to characterise the effect of process variables on the variation of mechanical properties in PV materials [4,28,31,37,43,87].

One important processing variable affecting mechanical properties is variation of cooling rate during quality heat treatment. PVs are very thick components, and can measure up to 1m thick for some forgings [87]. During rapid quenching, heat dissipation is largely controlled by

conduction through the component thickness [24], and this produces cooling rates which vary with depth. In turn, this produces significant variation of microstructure and mechanical properties throughout the component cross-section. It is therefore important to know how the microstructure and mechanical properties of SA508 Gr.3 Cl.1 vary with cooling rate, to ensure that mechanical property specifications are met.

The most common way to present microstructure variation as a function of cooling rate from high temperature austenite, is through the construction of continuous cooling transformation (CCT) diagrams. The CCT diagram is a plot of the critical temperatures of different transformations for iso-cooling rates, which are connected as a locus for each transformation, and separate the diagram into identifiable phase fields. Some CCT diagrams developed for SA508 Gr.3 Cl.1 are available in open literature [44,46,102], and are shown in Figure 10, however, as previously discussed there is disagreement between these diagrams leading to confusion about specific transformation kinetics. Furthermore, these diagrams do not contain any information regarding mechanical properties resulting from the variation of microstructure produced. Consequently, it is up to manufacturers to decide which microstructures (and thus cooling rates) are required to meet the specified mechanical properties. In addition, the ASTM material specifications for PV materials [26] are specified in the quenched and tempered condition; a condition that is not defined as part of CCT diagrams. Thus, in their current form, existing CCT diagrams have limited industrial use. For large forgings, the development of heat treatments for large forgings remains largely empirical, and is inefficient due to necessary iterations of destructive testing applied to component test coupons, following full-scale manufacture.

The HTS has been created to address these issues. It produces volumes of material that represents any applied thermal history, and are large enough to characterise both microstructure and mechanical properties from each specimen tested. This is a significant improvement in the development of heat treatments for large forgings as it increases the speed of analysis, and increases efficiency by reducing waste.

The work presented in this chapter validates the HTS for this task by developing a CCT diagram for SA508 Gr.3 Cl.1, which in addition to the traditional reporting of microstructure and hardness, also reports the tensile and impact properties both in the As-Quenched (AQ), and in Quenched and Tempered conditions (QT). This is completed in a number of stages: Firstly, a CCT diagram is developed for SA508 Gr.3 C.1 using ASTM standard dilatometry practices [64,65]. The critical temperatures, microstructure and hardness, are compared with the testing of four cooling rates using the HTS. The correlation between these results gives confidence in mechanical testing, and the results are presented together to produce a transparent CCT diagram.

The subject material is then tested using the HTS a second time for the four cooling rates. These specimens are tempered in accordance to ASTM standard tempering parameters specified for SA508 Gr.3 Cl.1. The specimens are then analysed, and the results are summed to complete the CCT diagram, characterising SA508 Gr.3 Cl.1 in an industrially valuable context.

6.2   EXPERIMENTAL

6.2.1   SA508 Grade 3 Class 1

The material used in the work was taken from the testing coupon of an SA508 Gr.3 C.1 tube sheet forging, manufactured at SFIL. The material was manufactured into a cylinder measuring 42mm diameter and 145mm gauge length. Following manufacture, each cylinder was normalised at 875°C to homogenise the microstructure while avoiding grain growth as shown in Chapter 4. The normalised cylinders were then manufactured into the standard HTS specimen geometry as detailed in Figure 19. This procedure was adopted to allow manufacture of small-scale dilatometry specimens and composition testing from each HTS specimen. Each HTS specimen was tested for composition by either Inductively Coupled Plasma Optical Emission Spectroscopy (ICP-OES) or Atomic Emission Spectroscopy (ICP-AES) depending on sample size, and all were found to exist within the ASTM specification limits for the material [25].

6.2.2   Small-scale dilatometry

To generate a CCT diagram for SA508 Gr.3 Cl.1, two specimens of 6mm diameter and 25mm gauge length were manufactured from each HTS specimen following normalisation. A total of 16 Netzsch specimens were made and tested. The specimens were tested using a Netzsch 402PC differential dilatometer for a range of cooling rates. All specimens were heated at 20°C/min to a temperature of 875°C where they were soaked for 30 minutes. Following soaking, the specimens tested on the Netzsch were cooled continuously at one of eight cooling rates: 30, 20, 15, 10, 7.5, 5, 2 and 1°C/min. Each test program was tested twice to produce a measure of uncertainty.

The critical temperatures for each cooling rate were calculated from the measured thermal expansions using the method discussed in section 5.1.1.1 These were plotted as a locus of points for each transformation on a plot of temperature against time to form the CCT diagram.

Following dilatometry, the Netzsch specimens underwent investigation by optical microscopy and hardness testing. The specimens were firstly mounted, then polished and etched using a 4% nitric acid solution. Optical images were taken of the etched specimens using a Nikon Eclipse LV150 bright field microscope, and the volume fractions of transformation products were quantified from the images by point counting. Hardness testing was undertaken to ASTM standards [96] using a Struers Durascan micro-hardness testing machine, using the Vickers hardness standard at 1kgF.

6.2.3   Large-scale dilatometry

Eight HTS specimens were tested on the HTS for four of the unique cooling rates tested in small-scale dilatometry. Two specimens were tested at each unique rate, 8 specimens in total. The rates tested by the HTS were 20, 10, 5 and 2°C/min, which were chosen to yield a large scope of rates for comparison. One set of four specimens that were cooled at these rates were analysed in the AQ condition, the remaining set of four underwent tempering and were analysed in the QT condition.

Following heat treatment and tempering, both the AQ and QT specimens were analysed using the same processes applied to the small scale Netzsch specimens, but in addition, were also tested by full scale tensile and Charpy impact testing methods. The mechanical testing on these specimens was completed using a Zwick-Roell tensile

testing machine at a strain rate of 0.015/min, and Zwick-Roell Charpy impact testing machines at SFIL. All testing was completed at RT and to ASTM standards [97,98] as this test temperature reflected condition of the CCT diagram. One tensile specimen and two Charpy specimens were manufactured from the representative volume of each HTS specimen.

6.2.3.1 Tempering

The ASTM standard tempering parameters for SA508 Gr.3 Cl.1 are a temperature of 650°C, and a duration equal to 30 minutes per inch of the component's maximum section thickness. This is followed by quenching in a liquid medium [25]. These tempering parameters correspond to the development of peak toughness, with respect to the preceding quench. Durations exceeding 30 minutes per inch are assumed to lead to temper embrittlement, during which the material toughness reduces rapidly.

During heat treatment of large forgings, components respond more slowly to heating and quenching due to increased section thicknesses. This increases the effective soaking time of the material with thickness leading to microstructure and properties that deviate from the assumed peak. For industry, it is important to know the effect of the tempering parameters on through-thickness. The ASTM standard accounts for varying component thickness using a design by rule criteria, but it does not detail the effect of variable cooling rate through thickness on the microstructure and properties. To assess the effect of tempering parameters for thick sections using comparatively small specimens accurately, it becomes necessary to determine a set of tempering parameters that yield an equivalent effect.

The Larson-Miller parameter has commonly been used to quantify equivalent effects of different tempering parameters, and is defined as:

$$LMP = T[Log(t) + C]$$ (16)

Where *LMP* is the Larson-Miller parameter, *T* is the temperature in Kelvin, *t* is the temper duration in hours, and *C* is a constant, which for Cr-Mo steels is commonly assumed to have an approximate value of 20 [103]. Using the *LMP* it is possible to compare the equivalencies of mechanical properties for different tempering parameters (temperature and time). To assess equivalent tempering parameters in respect to thickness, it is necessary to plot how the Larson-Miller parameter varies with temper duration for fixed tempering temperatures. This is plotted in Figure 48.
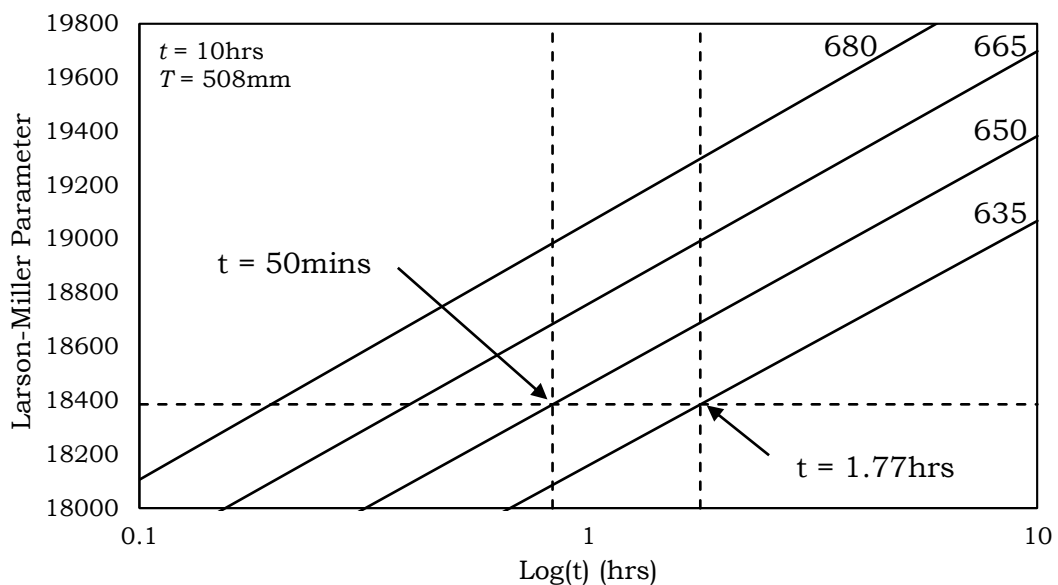

Figure 48: The Larson-Miller parameter plotted as a function of time for a number of tempering temperatures.

For the ASTM tempering parameters, the value of *LMP* is 18386.76. Using the diagram above, this value may be compared for all tempering

temperatures, giving the temper duration required for each temperature to attain equivalency. In the ASTM standard, a special requirement for SA508 Gr.3 Cl.1 states that the minimum tempering temperature permitted is 635°C. The duration for equivalency for this temperature is 1.77 hours, which corresponds to a section thickness of 90mm as per the ASTM guidelines. Since the HTS specimens are ~half this thickness, it is postulated that this better represents the effect of tempering for the ASTM tempering parameters in thicker sections using the HTS, and so these parameters were applied for the tempering process in this work.

The equivalent tempering parameters were applied identically to all four of the QT specimens using a feedback-controlled furnace. The specimens were heated in the furnace at a rate of ~20°C/min, held for the duration of 1.77 hours (~106 minutes), then removed from the furnace and quenched in an iced water bath to room temperature.

6.3   RESULTS

6.3.1   The CCT diagram

The CCT diagram generated from testing SA508 Gr.3 Cl.1 specimens using the Netzsch 402PC and HTS is shown in Figure 49. In this figure the ferrite, bainite and martensite start temperatures calculated from the Netzsch experiments are depicted using open symbols. The critical temperatures calculated from the HTS tests are depicted by crosses for each transformation for comparison.

The comparison between the HTS and the Netzsch experiments show strong correlation, however, there are some notable features between the Netzsch and HTS data sets. For example, the critical cooling rate for complete suppression of the ferrite transformation is greater for the

165

Netzsch specimens than for the HTS specimens. This is thought to be due to the volume fraction of ferrite transformed at faster rates. As discussed in Chapter 3 the representative volume of transformation is much less than the volume of each HTS specimen. When small volumes are transformed, it is difficult to ascertain accurate transformation start temperatures from the dilatation data. For the HTS, this temperature is more ambiguous due to the reduced sensitivity of the system when compared to the Netzsch dilatometer, and by the increased noise present during testing. A clear start temperature could not be determined for the ferrite transformation at for 20°C/min test, and so no critical temperature was included in these results in respect.
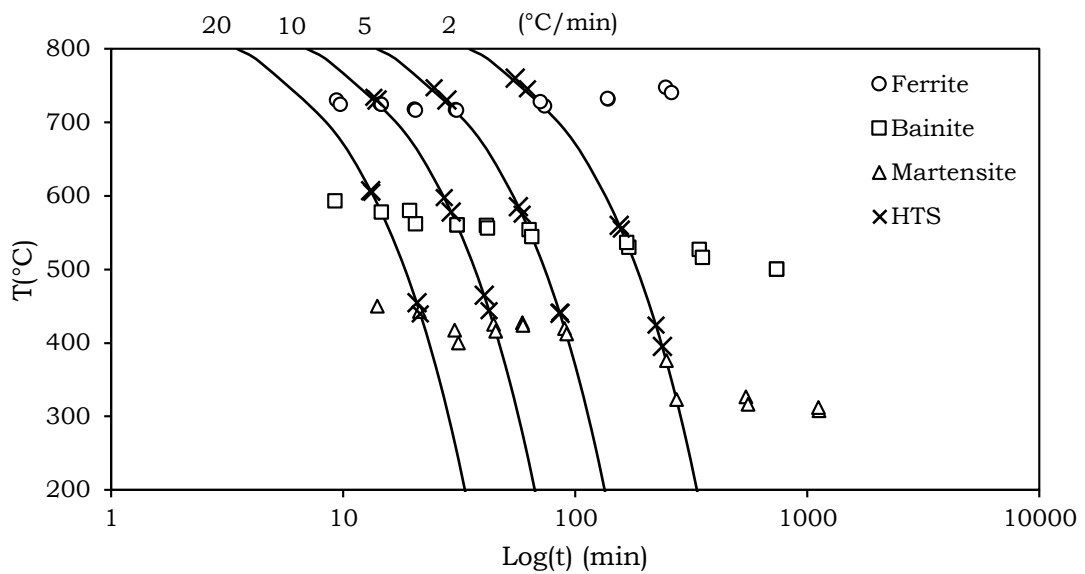

Figure 49: The CCT diagram determined for SA508 Gr.3 Cl.1. The crosses mark the critical temperatures for the specimens tested using the HTS.

The Netzsch dilatometer is more accurate in this respect, as the specimen scale is small enough to allow the assumption of homogeneity in temperature when heated and cooled rapidly. The critical cooling rate for ferrite was therefore investigated using the volume fractions calculated from dilatation. This is shown in Figure 50. The figure shows that the ferrite fraction reduces exponentially

166

with cooling rate, implying that the critical cooling rate for suppression of ferrite cannot be determined with great certainty. It is then appropriate to specify a volume fraction limit for transformed ferrite, which may be considered as negligible, and can be taken as the critical cooling rate for the suppression of ferrite. A detectable fraction limit discussed in open literature is 3% [104]. Using this volume fraction limit in this work also, Figure 50 indicates a critical cooling rate of ~29.2°C/min is needed for the suppression of the ferrite transformation in SA508 Gr.3 Cl.1.
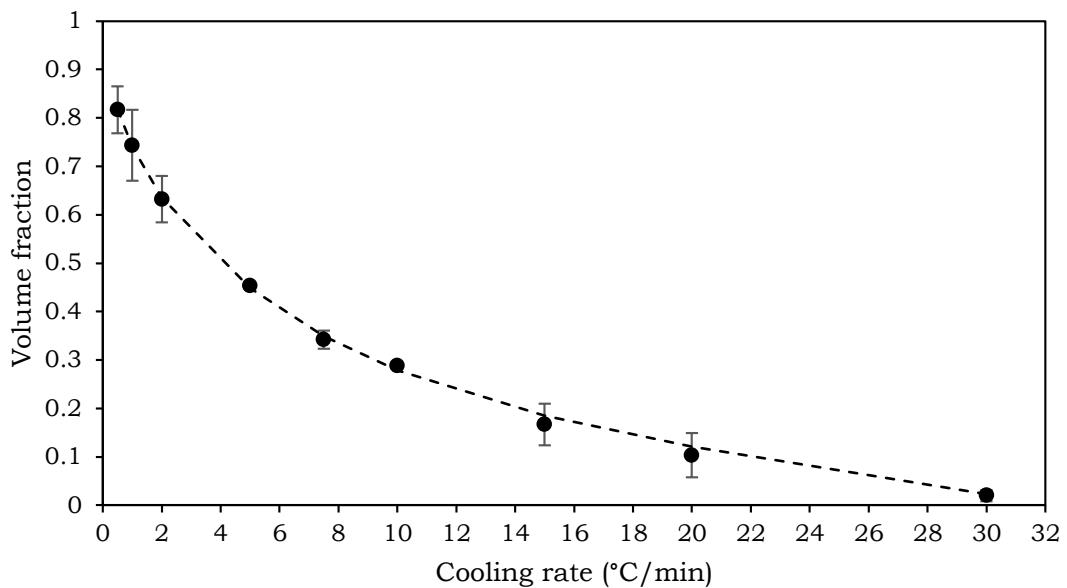

Figure 50: The volume fraction of ferrite transformed in SA508 Gr.3 Cl.1 as a function of cooling rate.
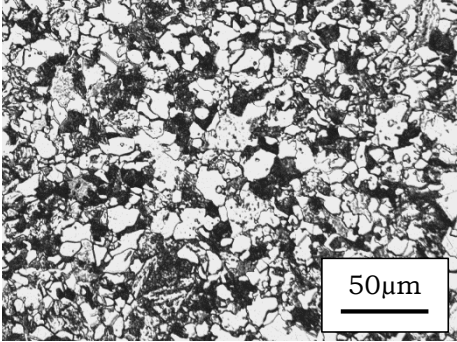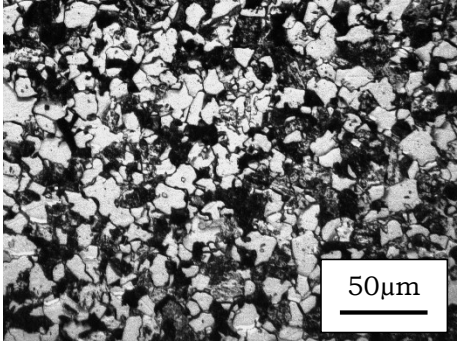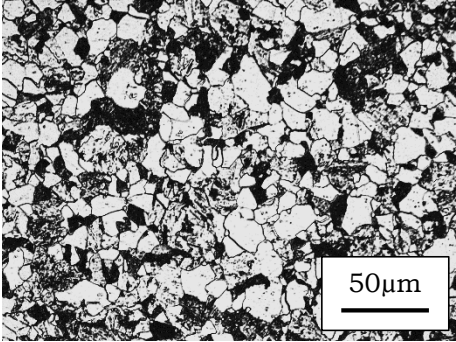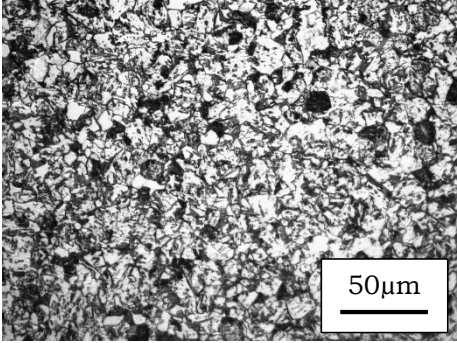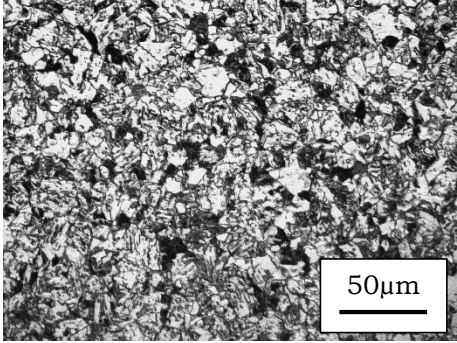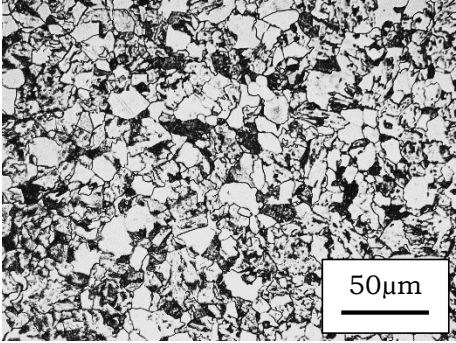
Another feature of the CCT developed is that in all cases, the critical temperatures determined from the HTS tests are slightly greater than the small-scale dilatometer. This is thought to be because of temperature variation in the much larger HTS specimens under testing. Transformation temperatures are calculated from thermal expansion as previously discussed, and any temperature variation is therefore measured in this quantity. Because of this, greater volumes of transformed material are recorded for higher temperatures when

heat loss due to end effects is present. In the large specimens tested by the HTS, the temperature of the sample is measured halfway along its gauge length using a surface thermocouple. End effects present during testing mean that transformation is occurring at the ends of the sample prior to the bulk of the sample, which is recorded as dilatation, thus the recorded temperature associated with the transformation is marginally higher than the actual temperature of the transforming material. However, the differences here are small, implying good temperature homogeneity through the thickness and along the length of the large specimens, and suggesting a large volume of the specimen material is representative of the imposed thermal profile.

6.3.2   Microscopy

While there is strong correlation of the critical temperatures plotted on the CCT diagram in Figure 49, it is necessary as part of the CCT development to confirm the identity of the phase fields from the test specimen's microstructure. In this work, a quantitative comparison of microstructure between the Netzsch dilatometer and HTS specimens was also necessary as part of the validation process, and so a microstructure investigation was performed on all the specimens tested.

A comparison of microstructures produced in the Netzsch specimens is shown in Figure 51. Both the HTS AQ and QT specimens are arranged for visual comparison. In Figure 52 are plotted the volume fractions of ferrite produced for each method as a function on cooling rate.

Cooling Rate	Netzsch As-Quenched	HTS As-Quenched	HTS Quench and Tempered
2°C/min			
5°C/min			

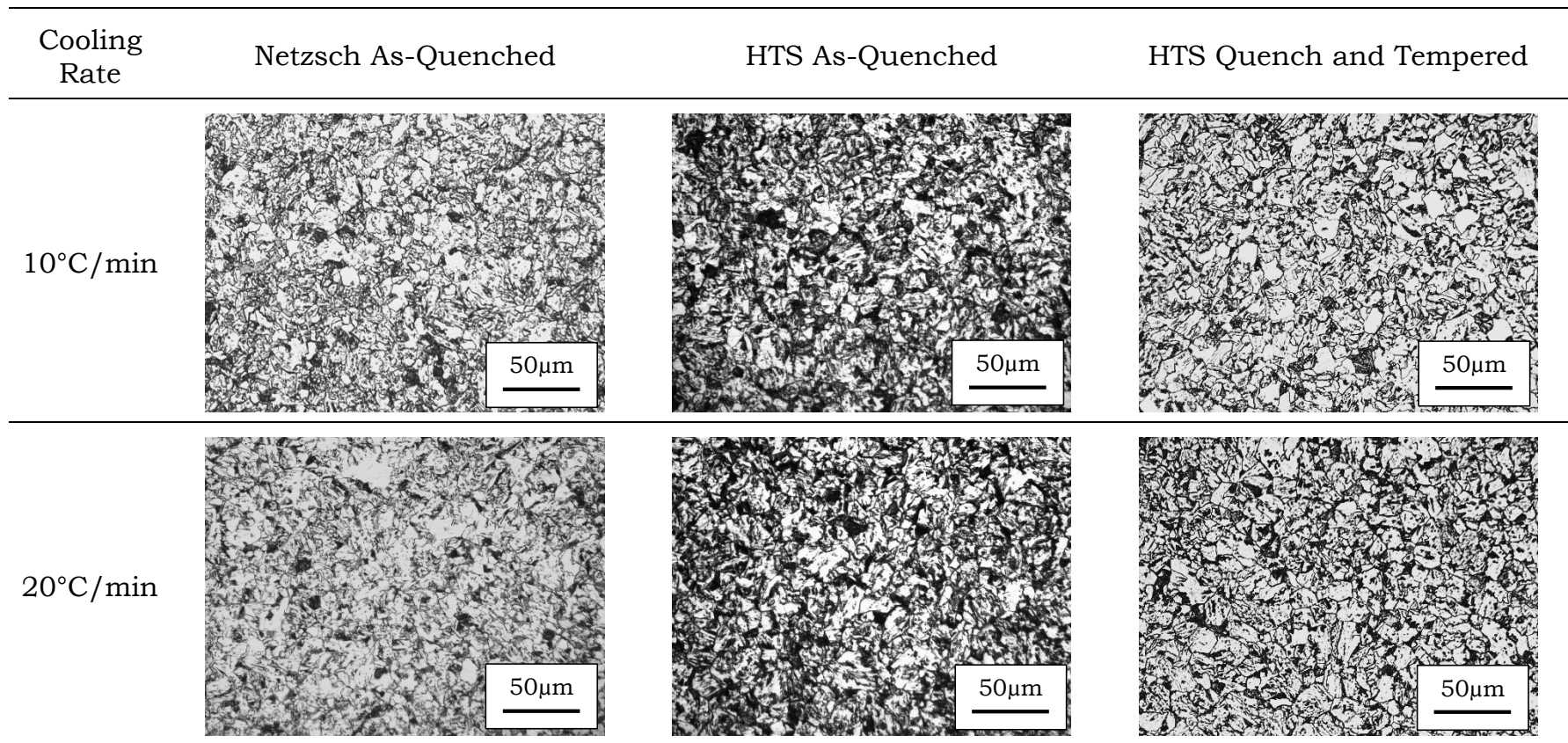| Cooling Rate	Netzsch As-Quenched	HTS As-Quenched	HTS Quench and Tempered
10°C/min	50µm	50µm	50µm
20°C/min	50µm	50µm	50µm

Figure 51: A comparison of microstructure between the Netzsch and HTS AQ specimens, and the HTS QT specimens for the cooling rates tested.

Reviewing the AQ microstructures of the Netzsch and HTS specimens, the visual comparisons show good correlations, indicating that accurate temperature tracking was achieved in the specimens when testing using the HTS: At 2°C/min the microstructure consists of ferrite, pearlite and bainite. At 5°C/min, the ferrite and pearlite volume fractions are reduced, and these volumes are replaced by Bainite respectively. At 10°C/min the ferrite fraction is reduced further, the Bainite fraction is increased further, and at 20°C/min, this trend is sustained. However, when comparing the micrographs between the HTS AQ and QT specimens the microstructures differ, with greater quantities of ferrite being noted. The magnitude of this observation appears to reduce with increased cooling rate.

It is easily seen that the fraction of ferrite varies significantly over the range of cooling rates tested. It is also easily identified in the microstructure; therefore, it is appropriate to quantify this transformation product for validation between the specimens tested in the Netzsch dilatometer and by the HTS. These volume fractions are plotted in Figure 52. In previous work the volume fractions have been calculated from the dilatation data, however, as discussed previously, the volume fractions of ferrite in the bulk of the HTS specimens is marginally greater than the Netzsch specimens due to the temperature inhomogeneity of end effects. This inhomogeneity affects the measured dilatation respectfully, and so calculation of volume fractions from the HTS data is not accurate of the tested representative volume. Point counting of the representative volume of each specimen tested was then needed for comparison of ferrite volume fractions between the HTS and Netzsch specimens.
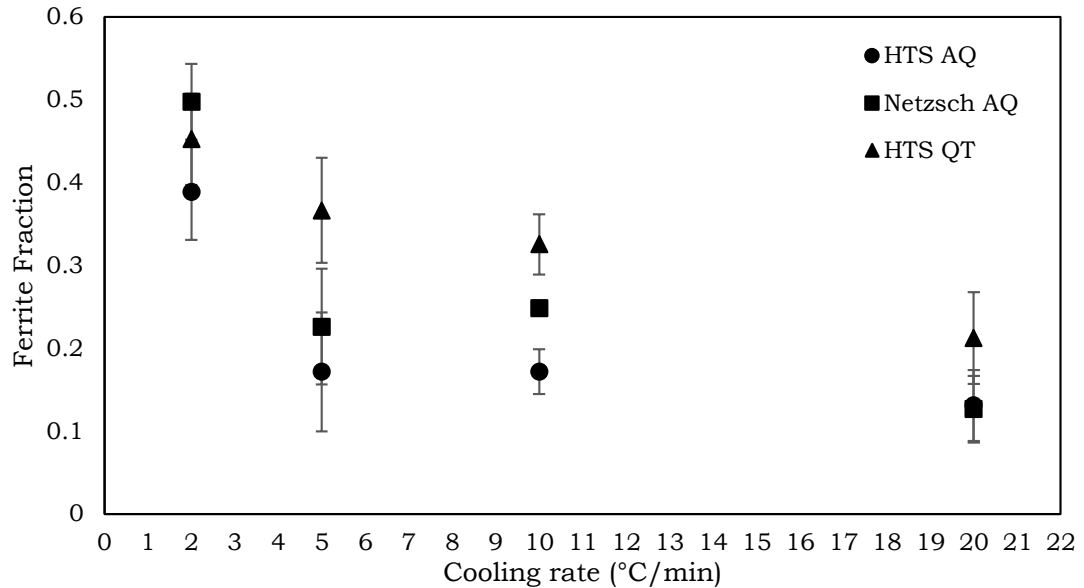
Figure 52: The volume fractions of ferrite in the Netzsch AQ, HTS AQ and HTS QT specimens, as determined by point counting. Values are reported with 95% confidence limits.

The ferrite fractions shown in Figure 52 show that for the AQ microstructures the fractions correlate well for each cooling rate, however, the Netzsch ferrite fractions appear to be consistently greater. This difference reduces for increased cooling rate and converges at 20°C/min.

The increased quantity of ferrite observed in the Netzsch specimens is thought to a consequence of increased partitioning of carbon in the HTS specimens. As previously discussed, the transformation of ferrite occurs at higher recorded temperatures due to heat loss by end effects. Internally the transformation is not begun, however the consequence of transformations nucleated at the surface of the specimen, is partitioning of carbon internally to the untransformed austenite, further stabilising it, and retarding transformation of ferrite. Since the transformation of the bulk proceeds along the temperature gradient towards the centre of the specimen, it follows that partitioning of carbon must occur along that gradient too. For each cooling rate, the quantity of ferrite produced in the HTS specimens must be less within

172

the representative volume than the Netzsch specimens are. Overall, the differences observed are small, and reduce with increased cooling rate. As cooling rate increases, the driving force is also increased for displacive transformations and so less ferrite is produced and less carbon is partitioned. Convergence in this way is anticipated for increasing cooling rate.

Critical to the conversation above is the consideration that there are experimental factors that affect the Netzsch specimens also. For example, as a specimen's scale is reduced, the ratio of surface area/ volume becomes greater. The surface of specimens can be considered as a defect of the microstructure that acts to increase the number of nucleation sites for diffusive transformations such as ferrite. This leads to partitioning of carbon also, however, as cooling rate is increased, the driving force for displacive transformations such as Bainite is increased as before. In actuality, many sources of inaccuracy contribute to the results attained from both testing methods, however, the comparison shows that a strong trend is sustained between the AQ samples tested by the Netzsch and HTS. This strongly suggests that the HTS can test and produce samples that represent the applied thermal profile with high accuracy, and provides confidence that the microstructure of the QT specimens is representative of the applied thermal program prior to tempering also.

6.3.3 Mechanical properties

The previous results build confidence that the HTS can accurately produce volumes of material that represent an imposed thermal profile. Confidence is then acquired that the mechanical properties of the tested specimens also represent the applied thermal profile.

Before the application of the HTS, mechanical properties were inferred from empirical relationships based on hardness testing. In this work, mechanical properties were tested directly from the HTS specimens. The Netzsch and HTS specimens were firstly tested for hardness as an additional validation measure, and then the material response to each cooling rate in the AQ and QT condition was tested mechanically by Charpy impact testing, and by tensile testing, directly from the tested HTS specimens.

6.3.3.1 Hardness and proof strength

Figure 53a) presents the results of hardness testing on the AQ and QT specimens tested by both methods. For the AQ specimens the results show good correlation of hardness for each cooling rate. Both data sets agree that hardness begins to fall at cooling rates descending from 10°C/min; however, there is divergence of the AQ values for reducing cooling rate. This is thought to be because of increasing hardenability of the HTS specimens at lower cooling rates. In the previous section, the partitioning of carbon in the HTS specimens due to temperature inhomogeneity was discussed. It follows that if the representative volume of the HTS specimens becomes marginally enriched in carbon for lower cooling rates, then the volume fraction of Martensite will be marginally increased too, increasing the measured hardness. This is underpinned when comparing the hardness of HTS AQ and QT hardness for each cooling rate. These are consistently separated by a Vickers hardness of ~65±3 for each cooling rate, implying that this same phenomenon is occurring repeatedly when using the HTS. However, a constant separation implies that the coarsening of ferrite occurs identically for each cooling rate tested. Since the point count in Figure 52 shows that this is not the case, it follows that the reduction of hardness by tempering is also due to the elimination of dislocations in the quenched microstructures, and by precipitation of carbon from the supersaturated microstructure components during the tempering

174

process. The sum of contributions is then thought to be constant within the experiments conducted here, with the individual contributions to hardness being proportionate to the volume of each transformation. However, this has not been investigated.

The hardness testing increases confidence that the HTS can simulate thermal profiles with a high degree of accuracy, and sums with previous evidence that supports validation of the HTS function. The evidence then provides confidence in the results of mechanically testing HTS specimens also being representative of the applied thermal programs, allowing complete material characterisation for each test.
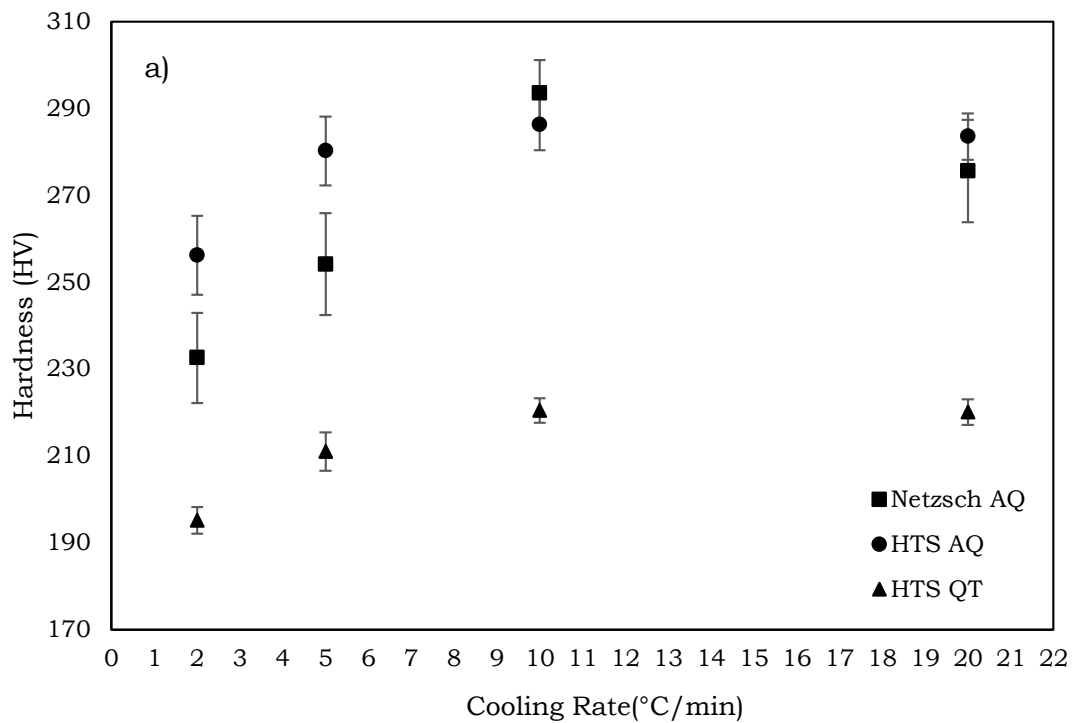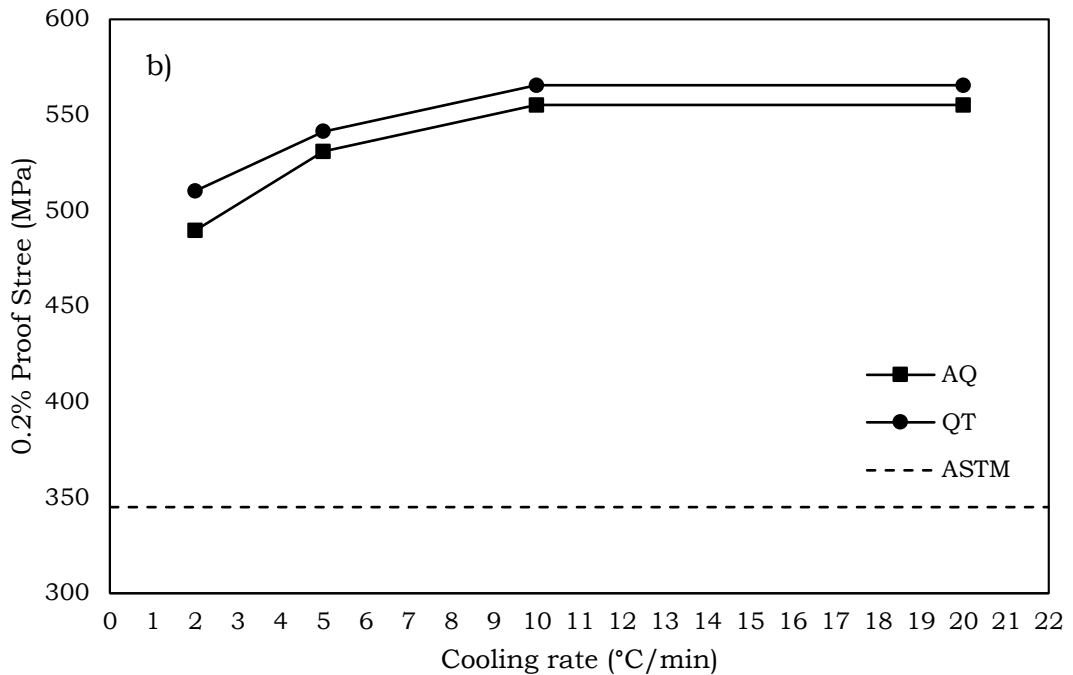
Figure 53a) A comparison of the Vickers hardness numbers for the microstructures generated by testing using the Netzsch dilatometer and HTS for AQ and QT conditions. The values are averages of between 18-33 indentations, and are plotted with 95% confidence limit, b) a comparison of the 0.2% proof stress of the AQ and QT specimens with respect to the ASTM standard minimum value.

In Figure 53b), the 0.2% proof stress of SA508 Gr.3 Cl.1 is plotted for each cooling rate, both in the AQ and QT conditions. The result shows tempering does not affect the proof stress greatly: the occurrence of yielding, as quantified here by the 0.2 proof stress, occurs during a transition from elastic to elastic-plastic deformation. In the elastic regime, deformation occurs without the movement of dislocations, and so the proof stress is primarily a function of material composition. The alloying solutes affect elasticity by distorting the crystal lattice, creating strain fields. Since the bulk composition for all specimens tested does not vary greatly, it follows that the proof stress does not vary greatly either. This also evidences why the proof stress of both the AQ and QT specimens reduces with reducing cooling rate, because at higher cooling rates the microstructure is more saturated with carbon, producing more martensite, a body-centred tetragonal crystal

176

formed from the distortion of the BCC crystal lattice upon transformation from FCC Austenite, and produces a higher proof stress.

6.3.3.2 UTS and impact toughness

In continuation of the discussion above it follows that during elastic-plastic deformation, the movement (or lack of movement) of dislocations has a large effect on mechanical properties. The UTS occurs at the transition of elastic-plastic to full plastic deformation and as previously discussed, has a functional relationship with dislocation density. Therefore, it is expected to vary between the AQ and QT conditions.

In Figure 54a), the UTS values are plotted for the AQ and QT specimens tested for each cooling rate. A large difference is seen between the AQ and QT samples, with the AQ samples having greater UTS values in all cases. This is due to the strengthening effects of dislocation entanglement. During tempering, the highly entangled dislocations caused by rapid quenching rearrange themselves to reduce the total energy state. The result is more dislocations can move under loading and the strengthening effect of entanglement is reduced. Supporting this is the observation that the UTS reduces with cooling rate. This is because of reduced quantities of displacive microstructure components.

In Figure 54b), the absorbed energy of the HTS AQ and QT specimens after Charpy impact testing is plotted. In the AQ condition, the result shows that the material does not meet the ASTM specifications for cooling rates of ~4°C/min and greater. However, the effect of the tempering process is to increase the impact energy for all cooling rates

significantly, such that all specimens meet the ASTM standard requirements.

In the AQ condition, the impact energy increases with decreasing cooling rate due to increased quantities of ferrite, however, the high dislocation density, and increased lattice strain field, control the fracture behaviour and keep the impact energy low. Following tempering these factors are reduced, increasing the impact energy significantly, however, the trend of impact energy to cooling rate is inversed, reducing with reducing cooling rate. This is due to the coarsening of allotriomorphic ferrite which provides continuous crack propagation paths for failure [47]. However, the fracture at low cooling rates following tempering absorbs significantly more energy than the ASTM standard specifies for the material. This implies ductile fracturing which is a necessity in the specification of safety critical pressure vessels.
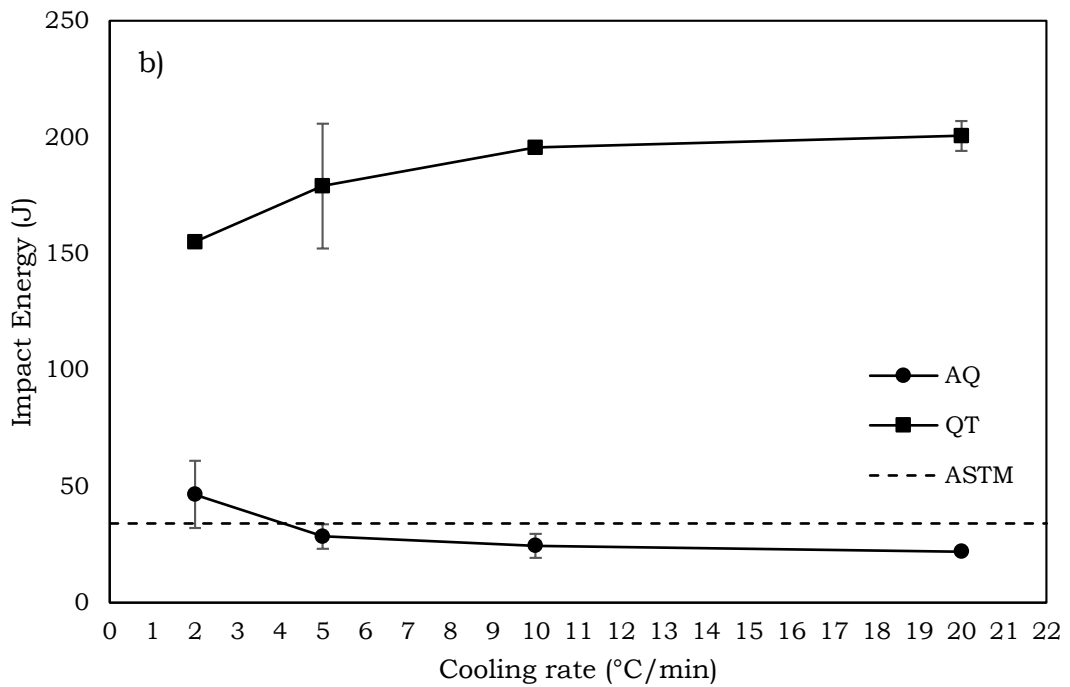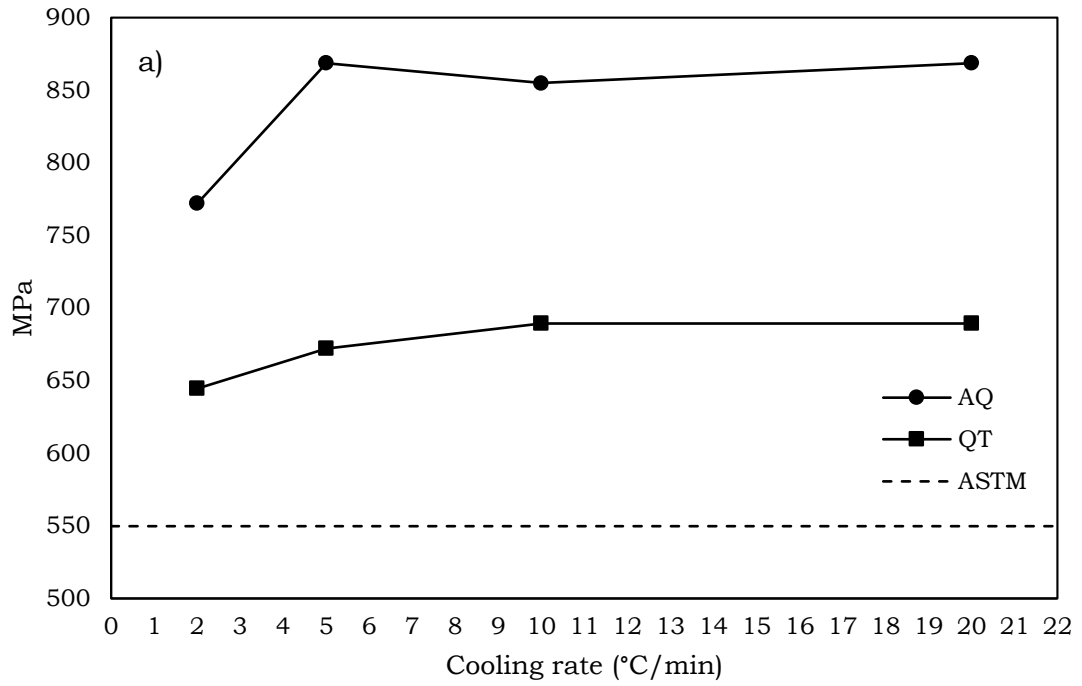
Figure 54a) The Ultimate Tensile Stress (UTS), and b) the Charpy impact energy of the HTS specimens in the AQ and QT conditions. The Charpy are averages of between 2 and 3 specimens and values are plotted with 95% confidence limits.
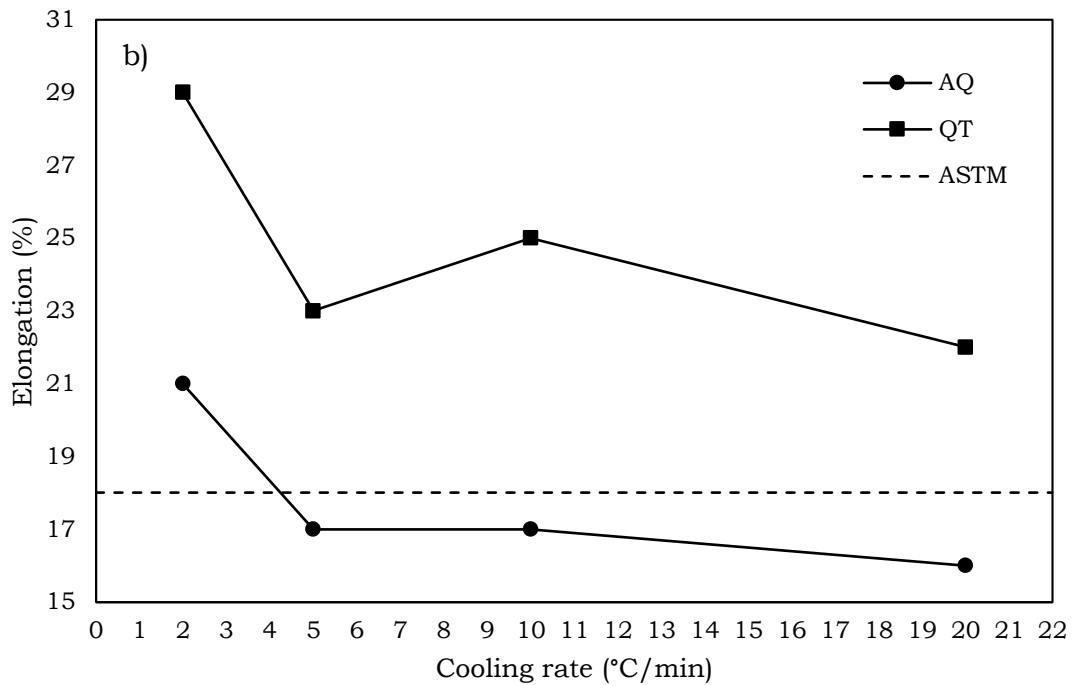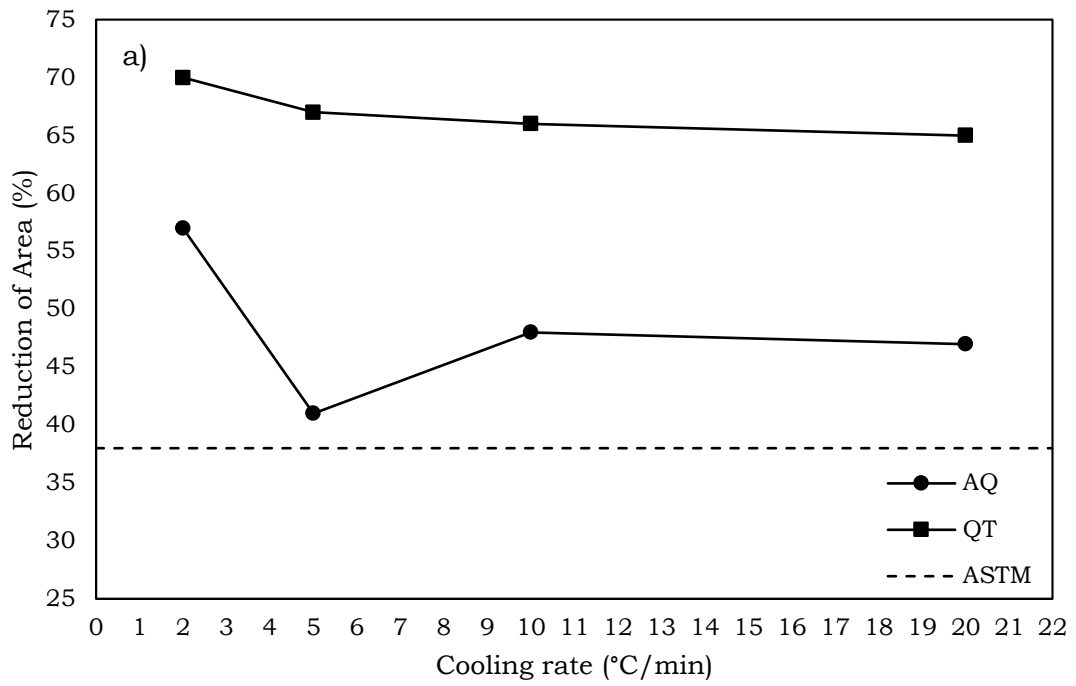
Figure 55a) The percentage reduction of areas (%RA), and b) the percentage elongation (%EL) of the HTS specimens in the AQ and QT conditions.

6.3.3.3 %RA and %EL

The percentage reduction of area (%RA), and percentage elongation (%EL) of tensile specimens are commonly quantified as measures of ductility. For the material tested in this work, these measures were also quantified, and plotted for the AQ and QT condition in Figure 55.

Figure 55a) shows how the %RA varies with cooling rate both in the AQ and QT conditions. In all specimens the ductility by this measure implies the material is better than the ASTM specification. In Figure 55b) however, the %EL shows that the ductility of the material does not meet the specification in the AQ condition for cooling rates of ~4°C/min and greater. This corresponds with the observations made for impact toughness in the AQ condition, but in similarity to impact toughness, the effect of tempering is to increase significantly both the %RA and %EL such that the material ductility is greater than the standard for all the cooling rates tested.

6.4   DISCUSSION

The aim of the work contained in this chapter was to validate the HTS as a general tool in analysing the effect of heat treatments on large forgings. The objective was to use it to produce a CCT diagram for the PV forging material SA508 Gr.3 Cl.1 that is more useful for industry due the addition of mechanical properties, and tempering characterisations, only possible by using the HTS. The results were positive with respect, however, in the absence of large quantities of data, some discussions are necessary to understand the limitations of the results, and so that the HTS can become validated.

6.4.1 The ferrite nose

The critical cooling rate at which suppression of the ferrite transformation is achieved is commonly known as the ferrite nose. In this work, it was discussed that there is disagreement in literature regarding this cooling rate, and so a transparent investigation was completed to investigate its magnitude. Its value was found be by ~29.2 C/min for a negligible volume of 3% transformed material, however this value is only similar to the CCT presented by Suzuki et al [102], and he did not reference or discuss the acquisition of that CCT diagram in his work. The other CCTs present ferrite noses that differ more greatly. Again, the work of Haverkamp et al [44] was not discussed or referenced, and the work of Francis et al [46] was modelled work for which the limitations have been discussed in the literature review.

The reason for this disagreement is the experimental process used for investigation. This is because the sensitivity of the equipment to small volumes of transformed material is the limiting factor. This was highlighted in section 6.3.1, when the ferrite nose was found to differ between the Netzsch dilatometer and HTS. Both the Netzsch and HTS measure dilatation with respect to temperature, and the sensitivity in detecting transformations depends on the resolution in measuring both quantities. There are however experimental procedures which are more sensitive than dilatometry when detecting transformations. One such method is Differential Scanning Calorimetry (DSC). Consider the plot in Figure 56.

A comparison of results from testing an SA508 Gr.3 Cl.1 specimen from a different PV forging than used in this work, at a cooling rate of 20°C/min using a Netzsch 402C dilatometer, the HTS, and a Netzsch 404 DSC. DSC is a method that characterises microstructure

transformations by measuring changes of specific heat (C_p). During a change of crystal structure, a material will either absorb or liberate energy in the form of latent heat, and this is measured as a specific quantity using DSC. It is clear from Figure 56 that the DSC is the only device sensitive enough to identify the start of the ferrite transformation clearly. The difference is thought to be because the quantity of heat liberated from each transformation is proportionate to the transformation mechanism. For diffusive transformations, the mass transport of atoms is greater, leading to proportionately more latent heat per unit volume, making small volumes easier to detect using DSC.
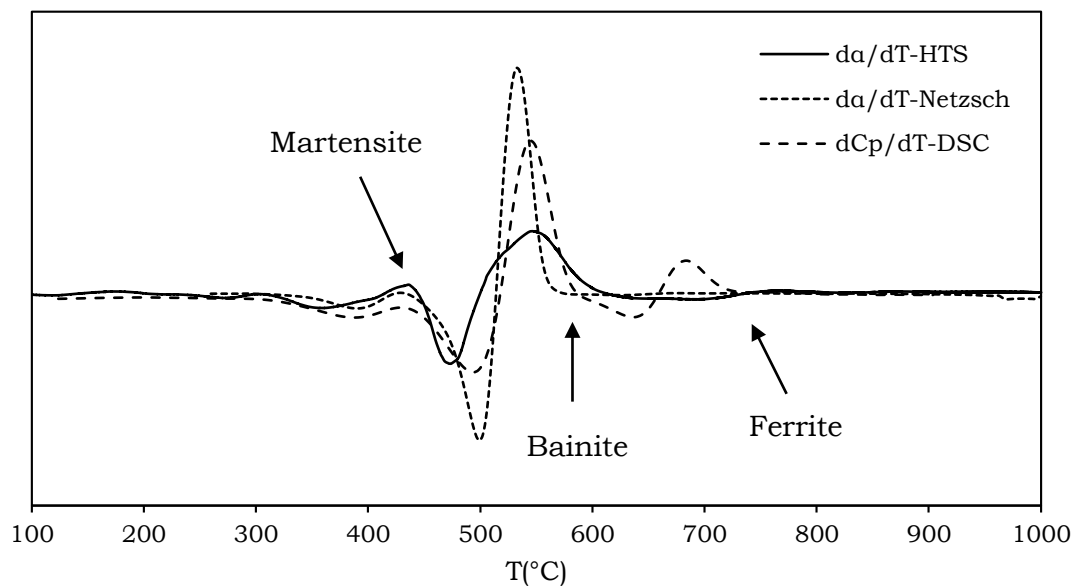
Figure 56: A comparison of experimental measures when testing SA508 Gr.3 Cl.1 cooling at the rate of 20°C/min.

Increased sensitivity in measurement is beneficial from a scientific perspective but it can lead to ambiguity when publishing results, as without comprehensive reporting of data comparisons between different sources will be notably different. From the industrial perspective, it is also an unnecessary degree of accuracy as the cooling rates achieved in large forgings are much slower than any of the ferrite

noses discussed, and at slow rates, the analysis of data is more accurate due to increased volume fractions. Other factors related to scale such as temperature homogeneity and composition variation also effect the determination of the ferrite nose, and so must be included for completeness. However, in this work the ferrite nose has been investigated and determined transparently, with full reporting of process variables, and therefore has reduced ambiguity surrounding the location of the ferrite nose in SA508 Gr.3 Cl.1, and has been completed with an industrially meaningful degree of accuracy.

6.4.2   Pearlite in SA508 Gr.3 Cl.1

The existence of pearlite in SA508 Gr.3 Cl.1 has not been discussed in open literature; however, the pearlite phase field has been included in some published CCT diagrams. In this work, this transformation field was omitted from those CCT diagrams to increase clarity in presentation; however, pearlite was said to exist in section 6.3.2 and so must be discussed.

In SA508 Gr.3 Cl.1, pearlite cannot be identified as a unique and hence identifiable transformation from dilatation alone. In the published works that identify the pearlite transformation, this transformation field is presented as a part of the ferrite phase field. In the work completed here, the pearlite transformation was difficult to characterise, as its volume and proximity to both the ferrite and Bainite transformations, made accurate identification of critical temperatures very unclear if at all, hence, this transformation was not studied in depth as it deviated from the aims and objectives of the study. However, the identification of all transformation products was necessary as part of this work and the existence of pearlite was indeed confirmed.

To confirm the existence of pearlite, the specimens were analysed at high magnification using an FEI Inspect F, Scanning Electron Microscope (SEM). Since pearlite is a reconstructive transformation that forms at low undercooling, it was assumed that larger quantities of pearlite are likely to form at low cooling rates. In Figure 57, images are taken of the Netzsch specimen cooled at 1°C/min.

At low magnification, ferrite can be easily identified. Bainite and pearlite cannot be so easily distinguished, but with increasing magnification, two different intra-grain morphologies containing carbide are identified. The first is a non-continuous arrangement of ferrite and cementite in a lath morphology within larger equiaxed grains. This is a typical morphology of upper bainite. The second is a continuous and finer ferrite/cementite structure within smaller equiaxed grains. At the highest magnifications the finer structure is seen to be lamellar in morphology and is therefore identified as granular pearlite [105].

The granular pearlite was identified in reducing quantities to a rate of 5°C/min. and the hardenability of SA508 Gr.3 Cl.1 assures the granular morphology remained at slow rates.

Pearlite does not exist in large quantities, or in the traditional lamellar plate morphology within the experimental work completed here, but it does exist, and therefore its contribution to the results shown here remains a subject further study.
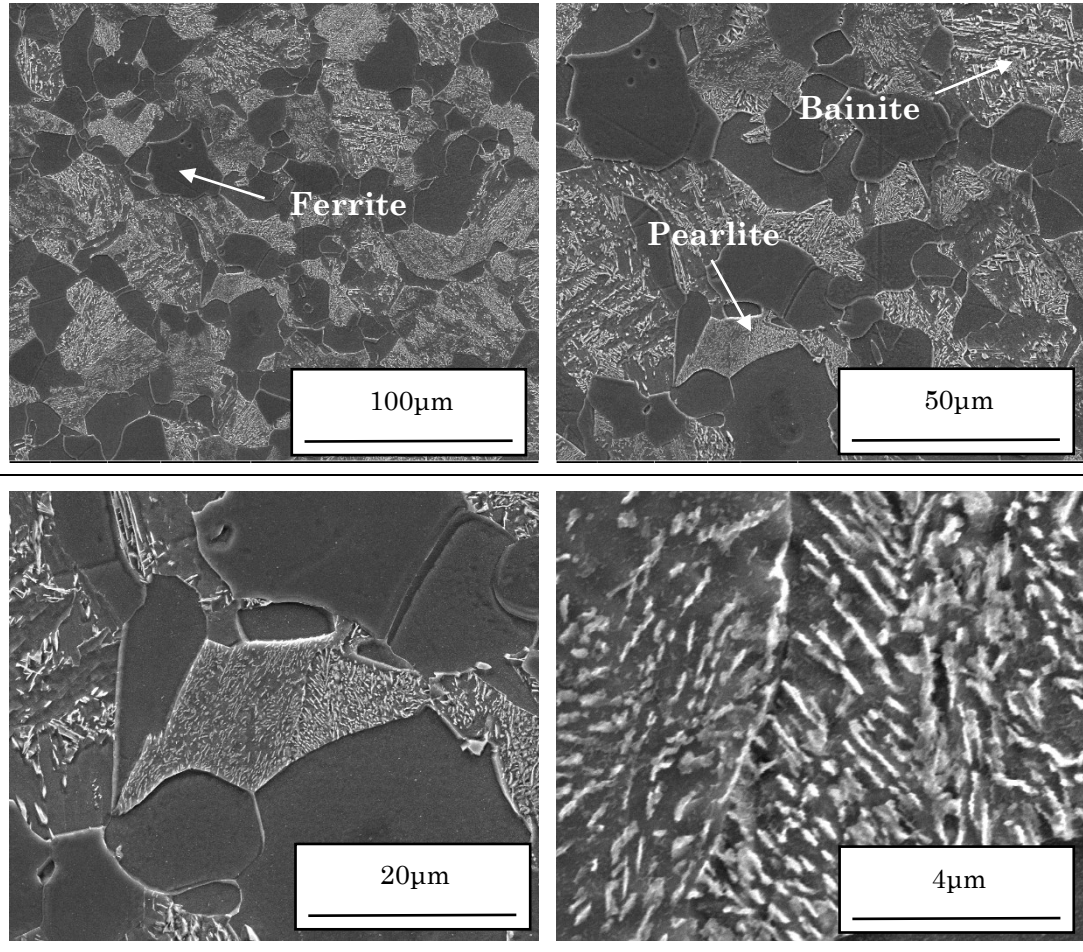
Figure 57: The SEM images of SA508 Gr.3 Cl.1 when cooled at 1°C/min. Images identify the existence of Granular Pearlite.

6.4.3 Composition variation

The results presented in this work were discussed in terms of data trends; however, it is observed that there was discontinuity to the trends for many of the results attained for the specimen tested at 5°C/min. This was thought to be because of composition variation within this specimen and was therefore investigated in respect.

The HTS specimens have scale of 42mm diameter and 135mm gauge length. These were machined from the test coupon of a 1m thick tubesheet forging following manufacture. The test coupons are designed to be representative of the slowest cooled regions of the

186

forging, and so are very thick. In total ten HTS specimens were made from the test coupon, this number of specimens represents a large length scale within the test coupon, and so it is likely for some composition variation to occur across these specimens.

The ten HTS specimens were identified numerically and the specimen tested at 5°C/min was denoted specimen five. From these specimens were also manufactured the Netzsch specimens, and these were tested at 5°C/min also. Two Netzsch specimens were tested at 5°C/min with markedly different results, as is seen in micrographs displayed in Figure 58:
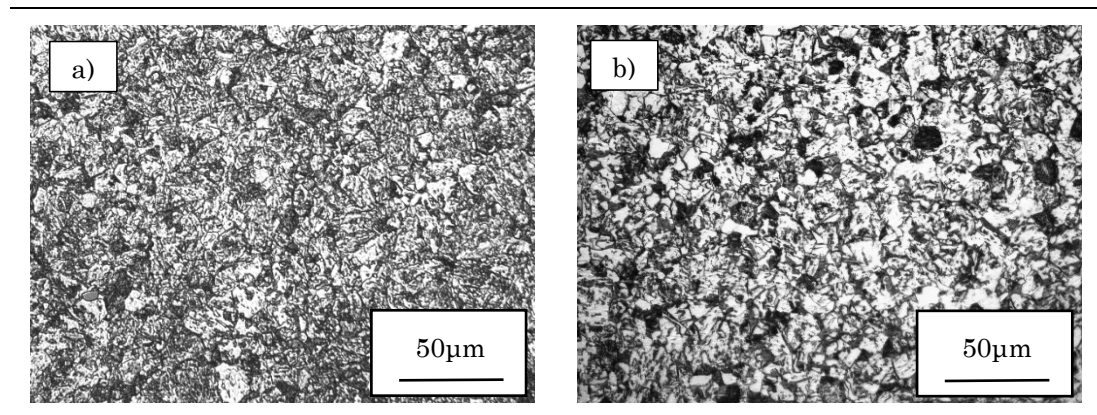
Figure 58: The micrographs taken for the two Netzsch specimens tested at 5°C/min.

A visual comparison between the micrographs implies an increased quantity of carbon in solution in image a). Increased carbon content stabilises austenite on cooling, increasing hardenability. Hardness testing and a volume fraction analysis from the dilatation data were then completed to investigate further, and the result confirmed increased hardenability and hence increased carbon content in the microstructure of image a):

Table 8: a comparison of hardness and microstructure for the two Netzsch specimens tested at 5°C/min.

	Hardness (HV)	Ferrite (%)	Bainite (%)	Martensite (%)
a)	317.78	34.43	42.59	22.98
b)	254.13	45.30	42.01	12.69

The reason for two different results from the same HTS specimen is segregation. In this work it has already discussed that micro-segregation due to partitioning of carbon in the solid state, exists due to temperature gradients during quenching, however, each specimen in this work was normalised and analysed prior to testing to ensure homogeneity of the initial microstructures. Any further segregation following this process must therefore be a macroscopic artefact of the casting process. Pickering studied macro-segregation in SA508 Gr.3 Cl.1 and found that bands of carbide were precipitated sympathetically with allotriomorphic ferrite formed along A-segregations during ingot casting [36]. It is postulated here that the HTS specimen five was taken from a region that possessed these precipitates, causing scatter in the results. However, the composition of specimen five was found to have the nominal ASTM composition when tested, and since the two Netzsch specimens taken from specimen five were different, the evidence suggests that composition variation is highly localised and while not identified in the other specimens tested, may still exist.

The effect of segregation is a random error in respect to the specimens tested here, and cannot be mitigated for except for through extensive quantitative analysis or by omitting. In this work, there was limited material available and so no repeat experiments could be completed, however, the results showed strong trends that have characterised SA508 Gr.3 Cl.1, suggesting the effect is negligible, and therefore have contributed positively towards validating the HTS.

6.4.4 Simulating tempering

The tempering parameters used in this work were chosen to represent thicker sections when compared to the specimen tested, while maintaining equivalency to ASTM standard tempering parameters. The goal was to avoid embrittlement by over-tempering. The result showed that the mechanical properties of the specimen were greatly improved by the tempering procedure, indicating that equivalent parameters and hence thicknesses, can be evaluated using the HTS, however, the usefulness of this result to industry remains limited.

In real PV forgings, the temperature lag associated with increased section thickness causes increased temper duration over the specified parameters. The result is that over-tempering does occur in real PV forgings with respect to the tempering parameters. In this work the assumption of tempering procedure was idealised; while a section thickness of 90mm can be simulated at a smaller scale, it was assumed that the no lag occurred during quenching, and therefore the resultant microstructure was a function of a constant temper applied to different quenched microstructures. In PV real forgings, this is impossible, and since the properties of SA508 Gr.3 Cl.1 following quality heat treatment are needed for completion of an industrially useful CCT, further investigation is needed.

To analyse fully the effect of tempering parameters for PV forgings for a range of thicknesses, a systematic and quantitative study is required. In this study, a single quench parameter (cooling rate) would be tempered for a range of Larson-Miller parameters that would then detail equivalent microstructure and properties for a number of tempering temperatures and durations. By testing for a number of unique quenches, a matrix of information could be plotted alongside the CCT diagram to define microstructure and mechanical properties

following complete quality heat treatments fully. For industry, the resulting CCT would display the quantifiable influence of tempering in an industrially useful context, and allow accurate predictions to be made. However, the work present here has shown the HTS can be used to simulate quality heat treatments accurately, and has tested a method of simulating heat treatment of large sections using the HTS with success. This has underpinned the usefulness of the HTS as a tool in industry, for quantifying the effect of heat treatments on large forgings.

6.5 SUMMARY

The aim of the work presented in this chapter was to validate the HTS by developing a CCT diagram for SA508 Gr.3 Cl.1, which in addition to the traditional reporting of microstructure and hardness, also reported the tensile and impact properties both in the As-Quenched (AQ), and in Quenched and Tempered conditions (QT). The findings of the study are summarised below:

1. The HTS has been used to generate a CCT diagram for the PV forging material SA508 Gr.3 Cl.1. The CCT has been verified by comparison to existing dilatometry standards.

2. The critical cooling that will suppress the formation of ferrite in SA508 Gr.3 Cl.1 has been evaluated by small-scale dilatometry, and found to be ~29.2°C/min, for a negligible transformation volume of 3%.

3. The HTS has been validated by comparisons of critical temperatures, microstructure, and hardness, against existing dilatometry standards under continuous cooling conditions.

4. The validation provides confidence that the mechanical properties attained from the HTS specimens are representative of each test. Mechanical properties for continuous cooling conditions were attained, fully characterising the material for each test.

5. A method of assessing the effect of tempering parameters on large forgings using the HTS was tested without validation. The test was successful but with limitation, as the parameters used were idealised. Therefore, further work is required to detail the effects of tempering parameters in an industrially meaningful context.

7   SUMMARY AND CONCLUSION

The aim of the project, whose findings are presented in this thesis, was to experimentally verify and validate a new large-scale heat treatment simulator for use in industry. The experimental work was designed to meet this aim, and each chapter presented, completed a specific objective in respect to it.

In Chapter 3 the objective was to investigate the temperature homogeneity of specimens under testing, and to optimize and correct the HTS performance respectively. The results of the optimization and correction procedure showed that a volume of representative material was systematically generated in HTS specimens. This volume was ~67% of the specimen bulk, and had dimensions that allowed both microstructure and mechanical properties to be determined from it. However, the result also showed that while the physical volume of each specimen was found to be representative, the recorded data was inaccurate due to systematic errors.

Chapter 4 investigated systematic error in the HTS data and found the error to be a function of cooling rate. A calibration procedure was developed using a specifically developed standard reference material, and was tested in comparison to small-scale dilatometry. Correlation

of the results in terms of CTE and relative dilatation showed that calibration had greatly reduced the magnitude of systematic error recorded for all cooling rates.

The combined results of chapter 3 and 4 verified that the HTS can accurately simulate industrial heat treatments, and so this was tested.

In Chapter 5, a thermal profile of a forging was simulated on the RPV material 20MND5. The study identified the limitations of simulation in terms of latent heat, and the effects latent heat on simulation were investigated. The result showed that the HTS could simulate accurately in comparison to small scale testing, and in comparison to predictions formed from material characterisations: The effect of latent heat on simulation was found to make the material more hardenable. The limitations to the new method were discussed, and it was noted that material characterisations were required for predictions to be made. However, the HTS is an instrument designed to characterise heat treatments on materials with greater functionality, and so a detailed material characterisation was performed.

In Chapter 6, a characterisation of the RPV material SA508 Grade 3 Class 1 was made using the HTS. The study tested the material for a range of cooling rates and for a tempered condition that related to a thick forged component. The results were compared to small-scale dilatometry, and found to be accurate, giving confidence in the values of mechanically testing HTS specimens. The results were plotted as a CCT diagram that was reported with mechanical properties, both in the as quenched, and quench and tempered conditions. This is an improvement over current CCT diagrams for SA508 Gr.3 Cl.1, and is more useful to manufacturers of large forgings for nuclear applications.

The HTS is an advancement on current dilatometry technology that is necessary for characterising both microstructure, and critically, mechanical properties, at standardised scales. The work presented has proven this functionality, a functionality unique to the HTS. Scope exists for further improvements to the technology and for further research; however, the results have shown the HTS to be a novel, unique instrument that has advanced the field of dilatometry, facilitating enhanced material characterisations. The studies reported in this thesis have verified and validated the HTS and its function, and its use will aid in the development of new materials and new heat treatment processes for large forgings, subsequently contributing to the growth of civil nuclear energy.

8   FURTHER RESEARCH

The design of the HTS facilitates studies of heat treatments on large forgings with greater functionality than current scientific methods, and the scope for further research using the HTS is great. Some of the possibilities for further research were identified in this thesis. These are detailed below:

Chapter 4 discussed that the HTS dilatation data did not represent the magnitude of transformation events. This is because the recorded dilatation related to the bulk, while microstructure and mechanical testing related only to the representative volume. This meant that some analysis of the data such as by Fishers formulation (equation 15) was not possible. During this study, effort was made to develop a mathematical model that related the representative volume to measured dilatation; however, this was not completed due to time constraints. An area of further research would be to develop and validate this model. This would further validate the HTS and add to its functionality.

Chapter 5 trialled a new method of evaluating heat treatments using the HTS by simulating a historical thermal profile. The results were compared with small-scale dilatometry for validation; however, the study focussed on the functionality of the HTS rather than the forging.

In industry, the microstructure and properties of the forging are of primary importance, and so an area of further research would be to validate the HTS by a physical comparison to the microstructure and properties of real forgings.

Chapter 6 developed a CCT diagram that contained microstructure and mechanical properties for SA508 Gr.3 Cl.1, both in the AQ and QT state; however, the QT state was un-validated. An area of further research would be systematic and validated study of the effect of tempering parameters on the mechanical properties of SA508 Gr.3 Cl.1.

REFERENCES

[1] A. Einstein, "Does the inertia of a body depend upon its energy-content?," *Ann. Phys.*, pp. 1–3, 1905.

[2] R. Leachman, "Nuclear fission," *Sci. Am.*, pp. 49–59, 1965.

[3] D. Bodansky, *Nuclear energy: principles, practices, and prospects.* Springer-Verlag, 2005.

[4] H. P. Romero, "Quantitative basis for the structure and properties of a critically-important pressure vessel steel," PhD. dissertation, Cambrige, 2014.

[5] A. Stoneham, "Nuclear fission: the interplay of science and technology.," *Philos. Trans. R. Soc.*, vol. 368, pp. 3295–313, 2010.

[6] K. Grandin, P. Jagers, and S. Kullander, "Nuclear Energy," *Ambio.*, vol. 39, pp. 26–30, 2010.

[7] K. Ehrlich, J. Konys, and L. Heikinheimo, "Materials for high performance light water reactors," *J. Nucl. Mater.*, vol. 327, pp. 140–147, 2004.

[8] T. Schulenberg, "Material requirements of the high performance light water reactor," *J. Supercrit. Fluids.*, vol. 77, pp. 127–133, 2013.

[9] R. W. Grimes, R. J. M. Konings, and L. Edwards, "Greater tolerance for nuclear materials.," *Nat. Mater.*, vol. 7, pp. 683–685, 2008.

[10] R. Schenkel, T. Schulenberg, C. Renault, and D. Haas, "Overview of Generation IV Liquid Metal-Cooled Fast Reactors: Advanced Supercritical Water and Molten Salt Reactors," in *Proc. GIF Symposium*, 2009, pp. 35-45.

[11] S. J. Zinkle and G. S. Was, "Materials challenges in nuclear energy," *Acta Mater.*, vol. 61, pp. 735–758, 2013.

[12] T. Abram and S. Ion, "Generation-IV nuclear power: A review of the state of the science," *Energy Policy*, vol. 36, pp. 4323–4330, 2008.

[13] Generation IV International Forum (GIF), "GIF R&D Outlook for Generation IV Nuclear Energy Systems." pp. 1–32, 2009.

[14] K. L. Murty and I. Charit, "Structural materials for Gen-IV nuclear reactors : Challenges and opportunities," *J. Nucl. Mater.*, vol. 383, pp. 189–195, 2008.

[15] S. J. Zinkle and J. T. Busby, "Structural materials for fission & fusion energy," *Mater. Today.*, vol. 12, pp. 12–19, 2009.

[16] International Atomic Energy Authority, "Nuclear Power Reactors in the World," Vienna, 2017.

[17] L. M. Davies, "A Comparison of Western and Eastern Nuclear Reactor Pressure Vessel Steels," *Int. J. Press. Vessel. Pip.*, vol. 76, pp. 163–208, 1999.

[18] International Atomic Energy Authority, "Nuclear Power Reactors in the World," Vienna, 2016.

[19] Y. Tanaka and I. Sato, "Development of high purity large forgings for nuclear power plants," *J. Nucl. Mater.*, vol. 417, pp. 854–859, 2011.

[20] J. Ling, "The Evolution of the ASME Boiler," *J. Press. Vessel Technol.*, vol. 122, pp. 242–246, 2000.

[21] J. W. Stokes, L. Holly, and K. H. Mayer, "The ASME Boiler and Pressure Vessel Code," *Non-Destructive Test.*, vol. 7, no. 3, pp. 145–151, 1974.

[22] J. Spence and A. Tooth, *Pressure Vessel Design: Concepts and Principles.* E & FN Spon, 1994.

[23] Y. Bangash, "PWR Steel Pressure Vessel Design and Practice," *Prog. Nucl. Energy.*, vol. 16, no. 1, pp. 1–40, 1985.

[24] J. Talamantes-silva, P. Bates, S. Al-Bermani, P. Davies, A. Hambleton, and D. Bunney, "New challenges for the production of ultra large forgings for the manufacturing of pressure vessels," in *Proc. of the ASME 2013 Pressure Vessels and Piping Conference*, 2013, pp. 1–9.

[25] American Society of Testing and Materials, "A508/508M: standard specification for quenched and tempered carbon and alloy steel forgings." pp. 1–9, 2004.

[26] American Society of Testing and Materials, "ASTM A788/788M: Standard Specification for Steel Forgings, General Requirements." 2015.

[27] F. Hochstein, W. Austel, and C. Maidhorn, "Application of a New Processing Procedure for the Further Improvement of Nuclear Grade Structural VCD Steels," *Nucl. Eng. Des.*, vol. 81, pp. 185–192, 1984.

[28] J. Kim, "Improvement of impact toughness of the SA 508 class 3 steel for nuclear pressure vessel through steel-making and heat-treatment practices," *Nucl. Eng. Des.*, vol. 174, no. 1, pp. 51–58, 1997.

[29] K. J-t, K. H-k, K. K-c, and K. J-m, "Improved Mechanical Properties of the A 508 Class 3 Steel for Nuclear Pressure Vessel Through Steelmaking," *Steel Forgings*, vol. 2, pp. 18–32, 1997.

[30] H. Pous-Romero, I. Lonardelli, D. Cogswell, and H. K. D. H. Bhadeshia, "Austenite grain growth in a nuclear pressure vessel steel," *Mater. Sci. Eng. A.*, vol. 567, pp. 72–79, 2013.

[31] E. J. Pickering and H. K. D. H. Bhadeshia, "The consequences of macroscopic segregation on the transformation behavior of a pressure-vessel steel," *J. Press. Vessel Technol.*, vol. 136, no. 3, pp. 1-7, 2014.

[32] K. Suzuki and K. Taniguchi, "The Mechanism of Reducing 'A' Segregates in Steel Ingots," *Trans. Iron Steel Inst. Japan*, vol. 21, no. 4, pp. 235–242, 1981.

[33] C. Maidorn and D. Blind, "Solidification and segregation in heavy forging ingots," *Nucl. Eng. Des.*, vol. 84, no. 2, pp. 285–296, 1985.

[34] G. Ostberg, "A review of present knowledge concerning the influence of segregates on the integrity of nuclear pressure vessels," *Int. J. Press. Vessel. Pip*, vol. 74, pp. 153–158, 1998.

[35] E. J. Pickering, "Macrosegregation in Steel Ingots," PhD. dissertation, The University of Cambridge, 2014.

[36] E. J. Pickering and H. K. D. H. Bhadeshia, "Macrosegregation and microstructural evolution in a pressure-vessel steel," *Metall. Mater. Trans. A.*, vol. 45, no. 7, pp. 2983–2997, 2014.

[37] Y.-S. Ahn, H.-D. Kim, T.-S. Byun, Y.-J. Oh, G.-M. Kim, and J.-H. Hong, "Application of intercritical heat treatment to improve toughness of SA508 Cl.3 reactor pressure vessel steel," *Nucl. Eng. Des.*, vol. 194, pp. 161–177, 1999.

[38] G. P. Gibson, M. Capel, and S. G. Druce, "Effect of heat treatment on the fracture toughness transition properties of an A508 class 3 steel," in *Defect Assessment in Components-Fundamentals and Applications*, J. G. Blauel and K. H. Schwalbe, Eds. Mechanical Engineering Publications, London, 1991, pp. 587–611.

[39] X. Y. Cheng, H. X. Zhang, H. Li, and H. P. Shen, "Effect of Tempering Temperature on the Microstructure and Mechanical Properties of a Reactor Pressure Vessel Steel," *Mater. Sci. Eng. A.*, vol. 636, pp. 164–171, 2015.

[40] M. Lin, S. S. Hansen, T. D. Nelson, and R. B. Focht, "Effects of Composition and Heat Treatment on the Toughness of ASTM A508 Grade 3 Class 1 Material for Pressure Vessels," in *Steel Forgings*, G. Nisbett and A. S. Melilli, Eds. American Society for Testing and Materials, 1997, pp. 33–55.

[41] C. Li, L. Han, G. Yan, Q. Liu, X. Luo, and J. Gu, "Time-dependent temper embrittlement of reactor pressure vessel steel: Correlation between microstructural evolution and mechanical properties during tempering at 650°C," *J. Nucl. Mater.*, vol. 480, pp. 344–354, 2016.

[42] American Society of Mechanical Engineers, "Specification for Quenched and Tempered Vacuum-Treated Carbon and Alloy Steel Forgings for Pressure Vessels," in *ASME Boiler and Pressure Vessel Code, Section II, Part A*, vol. 6, 2013, pp. 915–925.

[43] T. S. Byun, J. H. Hong, F. M. Haggag, K. Farrell, and E. H. Lee, "Measurement of Through-the-Thickness Variations of Mechanical Properties in SA508 Gr.3 Pressure Vessel Steels Using Ball Indentation Test Technique," *Int. J. Press. Vessel. Pip.*, vol. 74, no. 3, pp. 231–238, 1997.

[44] K. D. Haverkamp, K. Forch, K.-H. Piehl, and W. Witte, "Effect of heat treatment and precipitation state on toughness of heavy section Mn-Mo-Ni-steel for nuclear power plants components," *Nucl. Eng. Des.*, vol. 81, no. 2, pp. 207–217, 1984.

[45] K. Suzuki, I. Kurihara, T. Sasaki, Y. Koyoma, and Y. Tanaka, "Application of high strength MnMoNi steel to pressure vessels for nuclear power plant," *Nucl. Eng. Des.*, vol. 206, pp. 261–278, 2001.

[46] J. A. Francis, H. K. D. H. Bhadeshia, and P. J. Withers, "Welding residual stresses in ferritic power plant steels," *Mater. Sci. Technol.*, vol. 23, no. 9, pp. 1009–1020, 2007.

[47] H. Pous-Romero and H. K. D. H. Bhadeshia, "Continuous cooling transformations in nuclear pressure vessel steels," *Metall. Mater. Trans. A.*, vol. 45, no. 11, pp. 4897–4906, 2014.

[48] J. Kim, S. Lee, and T. Jin, "Fatigue evaluation of dissimilar welds on nuclear components," in *The International Conference on Structural Mechanics in Reactor Technology*, 2003, pp. 2–9.

[49] M. V. Li, D. V Niebuhr, L. L. Meekisho, and D. G. Atteridge, "A computational model for the prediction of steel hardenability," *Metall. Mater. Trans. B.*, vol. 29, no. 3, pp. 661–672, 1998.

[50] J. S. Kirkaldy and D. Venugopalan, "Prediction of microstrucure and hardenability in low alloy steels," in *Phase Transformations in Ferrous Alloys*, no. 1, A. Marder and J. Goldstein, Eds. New York: AIME, 1984, pp. 125–148.

[51] L. A. Dobrzański and J. Trzaska, "Application of neural networks to forecasting the CCT diagrams," *J. Mater. Process. Technol.*, vol. 157–158, pp. 107–113, 2004.

[52] J. Trzaska and L. a. Dobrzański, "Modelling of CCT diagrams for engineering and constructional steels," *J. Mater. Process. Technol.*, vol. 192–193, pp. 504–510, 2007.

[53] J. Trzaska, a. Jagiełło, and L. a. Dobrzañski, "The calculation of CCT diagrams for engineering steels," *Arch. Mater. Sci. Eng.*, vol. 39, no. 1, pp. 13–20, 2009.

[54] N. Saunders, U. K. Z. Guo, X. Li, a. P. Miodownik, and J.-P. Schillé, "Using JMatPro to model materials properties and behavior," *J. Mater.*, vol. 55, pp. 60–65, 2003.

[55] N. Saunders, Z. Guo, a P. Miodownik, and J.-P. Schillé, "The Calculation of TTT and CCT diagrams for General Steels," Sente Software Ltd., 2004.

[56] Z. Guo, N. Saunders, P. Miodownik, and J. P. Schille, "Modelling phase transformations and material properties critical to the prediction of distortion during the heat treatment of steels," *Int. J. Microstruct. Mater. Prop.*, vol. 4, no. 2, pp. 187-191, 2009.

[57] S. Kanagaraj and S. Pattanayak, "Measurement of the thermal expansion of metal and FRPs," *Cryogenics.*, vol. 43, no. 7, pp. 399–424, 2003.

[58] J. D. James, J. A. Spittle, S. G. R. Brown, and R. Evans, "A review of measurement techniques for the thermal expansion coefficient of metals and alloys at elevated temperatures," *Meas. Sci. Technol.*, vol. 1, pp. 1–15, 2001.

[59] Y. C. Liu, F. Sommer, and E. J. Mittemeijer, "The austenite-ferrite transformation of ultralow-carbon Fe-C alloy; transition from diffusion- to interface-controlled growth," *Acta Mater.*, vol. 54, no. 12, pp. 3383–3393, 2006.

[60] Y. C. Liu, F. Sommer, and E. J. Mittemeijer, "Calibration of the differential dilatometric measurement signal upon heating and cooling; Thermal expansion of pure iron," *Thermochim. Acta.*, vol. 413, pp. 215–225, 2004.

[61] G. Mohapatra, F. Sommer, and E. J. Mittemeijer, "Calibration of a quenching and deformation differential dilatometer upon heating and cooling: Thermal expansion of Fe and Fe-Ni alloys," *Thermochim. Acta.*, vol. 453, no. 1, pp. 31–41, 2007.

[62] G. Mohapatra, F. Sommer, and E. J. Mittemeijer, "A temperature correction procedure for temperature inhomogeneity in dilatometer specimens," *Thermochim. Acta.*, vol. 453, pp. 57-66, 2007.

[63] M. E. Brown, *Introduction to Thermal Analysis*. Kluwer Academic Publishers, 2001.

[64] American Society of Testing and Materials, "E289-04: Standard Test Method for Linear Thermal Expansion of Rigid Solids with Interferometry." pp. 82–90, 2004.

[65] American Society of Testing and Materials, "E228-95: Standard Test Method for Linear Thermal Expansion of Solid Materials with a Vitreous Silica Dilatometer." pp. 74–81, 1995.

[66] J. E. Daw, J. L. Rempe, D. L. Knudson, and J. C. Crepeau, "Thermal eexpansion coefficient of steels used in LWR vessels," *J. Nucl. Mater.*, vol. 376, no. 2, pp. 211–215, 2008.

[67] J. Cordero, T. Heinrich, T. Schuldt, M. Gohlke, S. Lucarelli, D. Weise, U. Johann, and C. Braxmaier, "Interferometry Based High-precision Dilatometry for Dimensional Characterization of Highly Stable Materials," *Meas. Sci. Technol.*, vol. 20, pp.1-10, 2009.

[68] H. K. D. H. Bhadeshia, "Some Phase Transformations in Steels," *Mater. Sci. Technol.*, vol. 15, no. 1, pp. 22–29, 1999.

[69] H. K. D. H. Bhadeshia, "Diffusional Formation of Ferrite in Iron and its Alloys," *Prog. Mater. Sci.*, vol. 29, pp. 321–386, 1985.

[70] H. K. D. H. Bhadeshia, "Very Short and Very Long Heat Treatments in the Processing of Steel," *Mater. Manuf. Process.*, vol. 25, no. 1–3, pp. 1–6, 2010.

[71] H. K. D. H. Bhadeshia and D. V. Edmonds, "Mechanism of Bainite Formation in Steels," *Acta Metall.*, vol. 28, pp. 1265–1273, 1980.

[72] P. Cizek, B. P. Wynne, C. H. J. Davies, B. C. Muddle, and P. D. Hodgson, "Effect of Composition and Austenite Deformation on the Transformation Characteristics of Low-carbon and Ultralow-carbon Microalloyed Steels," *Metall. Mater. Trans. A.*, vol. 33, no. 5, pp. 1331–1349, 2002.

[73] Y. S. Touloukian, R. K. Kirby, R. E. Taylor, and P. D. Densai, *Thermophysical Properties of Matter: Volume 12.* 1975.

[74] J. R. Davis, *ASM Speciality Handbook: Stainless Steels.* ASM International, 1994.

[75] M. Gomez, L. Rancel, E. Escudero, and S. F. Medina, "Phase Transformation under Continuous Cooling Conditions in Medium Carbon Microalloyed Steels," *J. Mater. Sci. Technol.*, vol. 30, no. 5, pp. 511–516, 2014.

[76] C. Garcia De Andres, C. Capdevila, F. G. Caballero, and D. San Martín, "Effect of molybdenum on continuous cooling transformations in two medium carbon forging steels," *J. Mater. Sci.*, vol. 36, no. 3, pp. 565–571, 2001.

[77] V. Colla, M. Desanctis, A. Dimatteo, G. Lovicu, and R. Valentini, "Prediction of Continuous Cooling Transformation Diagrams for Dual-Phase Steels from the Intercritical Region," *Metall. Mater. Trans. A.*, vol. 42, pp. 2781–2793, 2011.

[78] M. Atkins, *Atlas of Continuous Cooling Diagrams for Engineering Steels.* American Society for Metals, 1980.

[79] ASM International, *Atlas of Time-Temerature Diagrams for Iron and Steels.* ASM International, 1991.

[80] J. Davies and P. Simpson, *Induction Heating Handbook.* McGraw-Hill, 1979.

[81] W. F. Peschel, "Induction Heating of Microalloyed Forging Steels," *Mater. Sci. Forum,* vol. 284–286, pp. 451–460, 1998.

[82] American Society of Mechanical Engineers, "Standard Specification for Centrifugally Cast Austenitic Steel Pipe for High-Temerature Service," in *ASME Boiler and Pressure Vessel Code, Section II, Part D*, 2013, p. 756.

[83] J. P. Holman, *Heat Transfer*, 10th ed. McGraw-Hill, 2010.

[84] Joint Committee for Guides in Metrology, "Evaluation of measurement data — Guide to the expression of uncertainty in measurement," *International Organization for Standardization Geneva*, pp. 1-134, 2008.

[85] J. Feldstein and F. Lake, "A new constitution diagram for predicting ferrite content of stainless steel weld metals," *Mater. Des.*, vol. 14, no. 6, pp. 345–348, 1993.

[86] ASM International, *Austenitic Stainless Steels*, 1st ed. ASM International, 2008.

[87] S. S. Al-Bermani, P. S. Davies, C. Chesman, B. P. Wynne, and J. Talamantes-Silva, "Use of controlled heat treatment to predict mechanical properties in steel components," *Ironmak. Steelmak.*, pp. 1-7, 2015.

[88] H. K. D. H. Bhadeshia, *Physical Metallurgy of Steels*, 5th ed., University of Cambridge, 2014.

[89] C. García De Andrés, F. G. Caballero, C. Capdevila, and L. F. Álvarez, "Application of dilatometric analysis to the study of solid-solid phase transformations in steels," *Mater. Charact.*, vol. 48, pp. 101–111, 2002.

[90] D. San Martín, P. E. J. Rivera-Díaz-del-Castillo, and C. García-de-Andrés, "In situ study of austenite formation by dilatometry in a low carbon microalloyed steel," *Scr. Mater.*, vol. 58, no. 10, pp. 926–929, 2008.

[91] H.-S. Yang and H. K. D. H. Bhadeshia, "Uncertainties in dilatometric determination of martensite start temperature," *Mater. Sci. Technol.*, vol. 23, no. 5, pp. 556–560, 2007.

[92] B. (Pawłowski, "Determination of Critical Points of Hypoeutectoid Steels," *Arch. Civ. Mech. Eng.*, vol. 57, no. 4, pp. 10–15, 2012.

[93] G. L. Fisher and R. H. Geils, "A method for obtaining quantitative dilatometric data from alloys undergoing a phase transformation," *Metallography*, vol. 3, pp. 229–233, 1970.

[94] K. Suzuki, "Reactor Pressure Vessel Materials." International Atomic Energy Authority, pp. 70–164, 1998.

[95] T. Yokota, C. García Mateo, and H. K. D. H. Bhadeshia, "Formation of Nanostructured Steels by Phase Transformation," *Scr. Mater.*, vol. 51, no. 8, pp. 767–770, 2004.

[96] American Society of Testing and Materials, "E384-99: Standard Test Method for Microindentation Hardness of Materials." pp. 438–461, 2002.

[97] American Society of Testing and Materials, "E8/E8M-16a: Standard Test Methods for Tension Testing of Metallic Materials," pp. 1–27, 2009.

[98] American Society of Testing and Materials, "E23-16b: Standard Test Methods for Notched Bar Impact Testing of Metallic Materials." pp. 1–25, 2013.

[99] T. M. Tritt, *Thermal conductivity: Theory, properties and applications*. Kluwer Academic Publishers, 2004.

[100] M. Takahashi and H. K. D. H. Bhadeshia, "The interpretation of dilatometric data for transformations in steels," *J. Mater. Sci.*, vol. 8, pp. 477–478, 1989.

[101] M. Howson, B. Wynne, P. Davies, and J. Talamantes-silva, "Modelling the Effect of Phase Transformations on Cooling Rate During Quenching in Nuclear Forgings Using Effective Heat Capacity," in *Proc. International Forgemasters Meeting*, 2014.

[102] K. Suzuki, "Current steel forgings and their properties for steam generator of nuclear power plant," *Nucl. Eng. Des.*, vol. 198, pp. 15–23, 2000.

[103] H. C. Furtado, L. H. De Almeida, J. Dille, and I. Le May, "Correlation between hardness measurements and remaining life prediction for 2.25Cr-1Mo steel used in power plants," in *Journal of Materials Engineering and Performance*, 2010, vol. 19, no. 4, pp. 558–561.

[104] G. Krauss, *Principles of heat treatment of steels*. ASM International, 1980.

[105] L. E. Samuels, *Light Microscopy of Carbon Steels*, 1st ed. ASM International, 1999.